# SPIN OPTOMECHANICS OF LEVITATED NANOPARTICLES

A Dissertation

Submitted to the Faculty

of

Purdue University

by

Jonghoon Ahn

In Partial Fulfillment of the

Requirements for the Degree

of

Doctor of Philosophy

August 2020

Purdue University

West Lafayette, Indiana

# THE PURDUE UNIVERSITY GRADUATE SCHOOL
# STATEMENT OF DISSERTATION APPROVAL

Dr. Tongcang Li, Chair

      Department of Physics and Astronomy

      School of Electrical and Computer Engineering

Dr. Francis Robicheaux

      Department of Physics and Astronomy

Dr. Mahdi Hosseini

      School of Electrical and Computer Engineering

Dr. Minghao Qi

      School of Electrical and Computer Engineering

**Approved by:**

      Dr. Dimitri Peroulis

            Head of the School Graduate Program

To my family.

TABLE OF CONTENTS

LIST OF FIGURES

# ABBREVIATIONS

| | |
|---|---|
| BS | Beam Splitter |
| COM | Center of Mass |
| DAQ | Data Acquisition |
| DOF | Degree of Freedom |
| DSMC | Direct Simulation Monte Carlo |
| EMCCD | Electron Multiplying Charged Coupled Device |
| ESR | Electron Spin Resonance |
| NV | Nitrogen Vacancy |
| NA | Numerical Aperture |
| ODMR | Optically Detected Magnetic Resonance |
| PBS | Polarizing Beam Splitter |
| PSD | Power Spectral Density |
| RF | Radio Frequency |
| ROT | Rotational motion |
| r.p.m. | Rounds per minute |
| SEM | Scanning Electron Microscope |
| TEOS | Tetraethyl Ortosillicate |
| TOR | Torsional vibration |
| UTS | Ultimate Tensile Strength |
| VCO | Voltage Controlled Oscillator |
| ZPL | Zero Phonon Line |

# ABSTRACT

Ahn, Jonghoon Ph.D., Purdue University, August 2020. Spin Optomechanics of Levitated Nanoparticles. Major Professor: Tongcang Li.

With the unique advantage of great isolation from the thermal environment, levitated optomechanics has emerged as a powerful platform for various fields of physics including microscopic thermodynamics, precision measurements, and quantum mechanics. Experiments with optically levitated micro- and nanoparticles have already obtained remarkable feats of zeptonewton force sensing and ground-state cooling. The novel system has also been proposed to assess various theories including the objective collapse models and macroscopic quantum mechanics.

This thesis reports experimental results on a levitated Cavendish torsion balance, a GHz nanomechanical rotor, and a torque sensor with unprecedented sensitivity realized with optically levitated nanoparticles in a vacuum environment. The system at room temperature achieves a sensitivity of $(4.2 \pm 1.2) \times 10^{-27} \mathrm{Nm}/\sqrt{\mathrm{Hz}}$ surpassing the sensitivity of most advanced nanofabricated torque sensors at cryogenic environments. Calculations suggest potential detection of Casimir torque and vacuum friction under realistic conditions. Moreover, the nanoparticles are driven into ultrafast rotations exceeding 5 GHz, which achieves the fastest humanmade nanomechanical rotor. Such fast rotations allow studies on the ultimate tensile strength of the nanoparticles as well.

Subsequently, the electron spin control of nitrogen vacancies (NV) in optically trapped diamond naoparticles is demonstrated in low vacuum. The configuration is analogous to trapped atoms and ions which serve as a quantum system with internal states. The effect of the air pressure, surrounding gas, and laser power on the electron spin resonance (ESR) are studied, and the temperature of the diamond is

also measured with the ESR. The levitated nanodiamonds will provide the means to implement a hybrid spin-optomechanical system.

# 1. INTRODUCTION

## 1.1 Radiation Pressure and Angular Momentum of Light

Light and electromagnetic waves are capable of exerting a force, or radiation pressure, on a matter via momentum exchange. In 1862, the momentum from electromagnetic radiation was theoretically predicted by James C. Maxwell. According to his predictions, if the Poynting vector ($\mathbf{S} = \mathbf{E} \times \mathbf{H}$) is divided by speed of light, it would correspond to the momentum per unit area of the electromagnetic field [1]. Therefore, a fully absorptive surface would experience a radiation pressure exerted from a perpendicular beam of light of $F = P/c$ which shows that the force equals to the power of light divided by speed of light. For a source of light with a power of 1 W, the radiation pressure would be approximately 3.3 nN. Furthermore, if the surface is a totally reflecting mirror, the force would be doubled due to the reflection, and the force from a 1 W light source on a perfect mirror would be about 6.7 nN.

Later, in the years of 1900 and 1901, the existence of radiation pressure was experimentally verified independently by Pytor Lebedev [2], and by Nichols and Hull [3]. In the experiment by Nicholas and Hull, a torsion balance with two mirrors attached were used. Light from a thermal light source was focused onto one of the mirrors and the balance moving from its equilibrium position was observed. Although the minute force from light had been measured, it was viewed to be too small to be utilized for any practical purpose. In 1905, during his speech to the British Physical Society, J. H. Poynting quoted, "A very short experience in attempting to measure these forces is sufficient to make one realize their extreme minuteness, beyond consideration in terrestrial affairs" [4]. After several decades after this comment, the laser was invented and the force from light has gained a plethora of applications in various fields of science [5, 6].

Besides the force generated from the linear momentum of light, another important aspect would originate from the angular momentum of light that can exert an optical torque on matter. In 1936, Richard A. Beth conducted the first experiment to confirm an optical angular momentum transfer to an object resulting in a torque [7]. A doubly refracting plate was suspended from a quartz fiber in a vacuum environment and a circularly polarized light was directed through the plate. The exerted torque from the change in light polarization could be detected with the torsional pendulum and the results could show the optical torque delivered to the plate is $\tau = 2P/\omega$, where $P$ is power and $\omega$ is the angular frequency of light. As the circularly polarized light passes through the half waveplate, the handedness of the polarization is reversed which is responsible for the factor of two in the amount of torque exerted onto the plate. The study could also verify the angular momentum of $2\hbar$ has transferred to the plate per photon.

## 1.2   Optical Manipulation of Microscopic Particles

Beginning from the early 1970s, with the invention of the laser, Arthur Ashkin and his colleagues started to carry out experiments using the laser-induced optical forces on microscopic particles [8–12]. In particular, in 1986, Ashkin was able to report on the first invention of the optical tweezer which is formed with a single laser that is tightly focused and uses the gradient force to stably grab microscopic particles in all three dimensions [13]. In 2018, Arthur Ashkin was presented Nobel Prize in Physics for his work on optical tweezers and its role in biological studies. A more detailed introduction to the development of the optical tweezer will be presented in the following chapter of the thesis.

In addition to the optical forces that can be used for manipulation of microscopic particles in the translational directions, efforts have appeared to harness optical torque to control the angular orientation of the laser trapped particles. An optically induced torque were generated either by the absorption of a Laguerre-Gaussian laser beam

[14, 15] or by modifying the angular momentum of the trapping beam with the shape [16] or birefringence [17] of the trapped object. The torque from light exerted on the various particles were also experimentally analyzed through observations on the changes in polarization of the scattered light [18, 19]. The added rotational control of optically trapped microparticles enabled various applications for microrheology, optical micromachines, and biotechnology [20, 21].

## 1.3 Levitated Optomechanics

Dielectric particles have been optically levitated in air and vacuum and have been reported since the early work of Ashkin and Dziedzic that used the counterbalance between a gravitational force on the particles and the scattering forces from an upward laser beam [9–12]. Afterwards, a single beam optical trap that uses the gradient force was implemented in air [22], followed with optical levitation with counter-propagating lasers [23, 24], and later with a single beam [25] in vacuum. Concurrently, there have been approaches to levitate particles in vacuum with Paul traps [26–30] or magneto-gravitational traps [31, 32].

Levitated optomechanics has received significant attention for its unique properties differentiating the platform from conventional mechanical oscillators. Most importantly, levitated particles are absent of a mechanical clamp which typically serves as the main source of decoherence in common mechanical resonators. Therefore, the primary source of dissipation for the levitated optomechanical platform arises from the surrounding gas, and can be further decoupled from the thermal bath once the system reaches a vacuum environment. Furthermore, the mechanical properties including the oscillation frequency and damping can be easily tuned, and rare dynamics like free rotation can be observed with the levitated objects.

With its great isolation from the thermal environment and tunable system parameters, levitated optomechanics has become an important platform for diverse experimental research including microscopic thermodynamics and precision measure-

ments [33,34]. The ability to operate in vacuum where the levitated object is under-damped allowed the first observations of ballistic Brownian motion [23] and Kramers turnover [35], and tests of fluctuation theorems [36,37]. Moreover, the large quality factor arising from the great thermal isolation allowed the use of levitated particles as sensors for force [38,39], acceleration [40], and torque sensing [41].

In parallel with the experimental progress, numerous theoretical proposals have appeared to utilize levitated optomechanics for studies of fundamental physics. The early work identified the opportunity to couple the levitated particles to optical cavities [42, 43] which called large attention to the field. Subsequently, the levitated particles exploited as ultrasensitive sensors were proposed to enable search for the exotic forces and interactions associated with dark energy [44], non-Newtonian gravity [45,46], and gravitational waves [47]. Furthermore, once the motion of the trapped particles in vacuum are cooled, quantum behavior have been proposed to be observed from macroscopic objects even in room temperature conditions. The quantum mechanical states of the large objects anticipate for experiments on macroscopic quantum superposition [48–50], objective collapse models [51,52], and matter-wave interferometry [53–55].

In order to realize the aforementioned ambitious proposals, many experiments have pushed towards cooling down the motion of the levitated particle into the quantum regime. The ability to confine particles in a harmonic potential and also to monitor their motion from the scattered light opened up the opportunity for feedback cooling on the center of mass (COM) motion of levitated particles. Using active force feedback [24,31,56–58], parametric feedback cooling [25,59–61], and cavity cooling [27,62–65], various groups were able to cool the translational motions in the range of millikelvins and below. Most recently, the first demonstrations of quantum mechanical motions [61] and quantum ground state cooling has been reported [65].

### 1.3.1 Torsional and Rotational Degree of Freedom

Added to the COM motion, the angular degree of freedom (DOF) of a levitated object has also become a matter of interest for the levitated optomechanics community. Early theoretical work have proposed the use of Laguerre Gaussian modes and orbital angular momentum of light to cool the rotational motion of dielectric rods and to generate optomechanical interactions with dielectric microwindmills [42, 66]. Furthermore, the spin angular momentum could also be used to apply torque and exhibit rotational motions on levitated birefringent particles [67–70] and nonspherical particles [71, 72] that were optically levitated in air and vacuum. Similar experiments have been demonstrated with graphene particles in Paul traps [26, 73] and an electrically driven rotation has been reported with microspheres in an optical trap [74]. The reduction in rotational damping in vacuum has previously enabled rotations as fast as 10 MHz [68].

In addition to rotational motions, experimental control on torsional vibration [41, 75] and precession [76] of levitated nanoparticles has also been demonstrated. It has been shown that the torsional motion has a higher frequency compared to that of translational motions, which is advantageous for ground state cooling [41]. Additionally, theoretical calculations have suggested future studies with the angular DOF of levitated particles to detect Casimir torque [76–78] and generate macroscopic angular superpositions [55, 79].

In this thesis, as shown in Fig.1.1, nanodumbells are used which are nonspherical nanoparticles with a well defined geometry. In linearly polarized optical tweezers, the levitated nanodumbell shows a torsional vibration and can be considered as a very sensitive torsion balance. With the optically levitated torsion balance, unprecedented torque sensitivities is expected to be achieved that may also be capable of measuring anisotropic surface interactions [77]. With a circular polarization, the dumbbell-shaped nanoparticles are driven into a rotation exceeding 1 GHz [75, 80]. With such high rotations, material properties in extreme conditions can be measured [73, 81, 82].
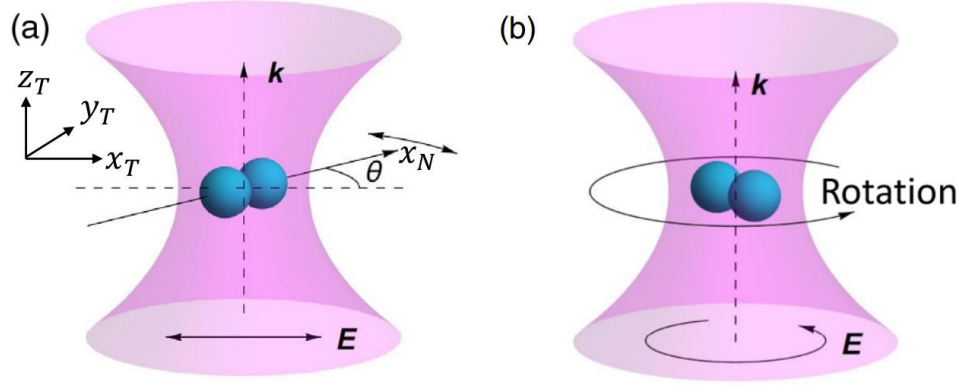
Fig. 1.1. (a) A dumbbell-shaped nanoparticle levitated in a laser with linear polarization. (b) A dumbbell-shaped nanoparticle levitated in a laser with circular polarization.

Furthermore, the optical torque delivered to optically levitated nanorotors is utilized to demonstrate experiments of ultrasensitive torque detection [83]. The unprecedented levels of torque sensitivity of the system is envisioned to provide the means for investigation on unexplored regimes of science such as the probing of vacuum friction [84–86].

## 1.4   Nitrogen Vacancies and Levitated Nanodiamonds

The second part of this dissertation contains experimental work based on the proposals to implement a hybrid quantum device with levitated particles. Previous experiments have demonstrated coupling between the motions of mechanical resonators and a single electron spin with the desire to attain a strong coupling and to actualize the proposed uses in quantum information science and quantum metrology [87,88]. With an even higher quality factor, the levitated particles with an internal degree of freedom would realize a hybrid spin-optomechanical system that provides the remarkable opportunity to investigate the unexplored regimes of fundamental physics [50,51,53].

The diamond nitrogen vacancy (NV) centers are most often referred as the suitable system for such applications.

Atomic impurities or color centers in diamond have drawn great attention for its future applications in nanoscale sensing [89–92], quantum information [93, 94], and quantum computing [95, 96]. Among the various color centers, the diamond NV center is considered to be the leading candidate for the various applications. An NV is composed with a nitrogen atom and a neighboring vacancy site that takes place of the carbon atoms, as illustrated in Fig. 1.2(a). The characteristics of the NV centers that make it favorable include the stable single photon emission at room temperature [97, 98], the long spin coherence times at room temperature [99, 100], and the optically detected magnetic resonance (ODMR) [101–104]. In particular, the ODMR, or the optical addressed electron spins, provides the means for readout and manipulation of the quantum states with high fidelity, laying the foundations for the diverse quantum technologies.

A nitrogen vacancy center that is negatively charged, NV$^-$, has six electrons and forms a spin-1 system. As mentioned in the above, an interesting characteristic of a NV$^-$ is that the spin state of the defect can be addressed and read out optically. The energy levels that a NV$^-$ have are depicted in Fig. 1.2. With zero external magnetic field, the spin-1 ground state is split into a $m_s = 0$ state and a nearly degenerate $m_s = \pm 1$ state by cause of local magnetic interactions. The $m_s = 0$ state is positioned approximately 2.87 GHz below the $m_s = \pm 1$ state and a resonant microwave can be used to alter the population between the two states. With a green laser, the NV$^-$ in the ground state is excited to the excited state. The NV$^-$ in the excited state relaxes through a radiative transition with a fluorescence in the 600 to 800 nm range. In both the excitation and the relaxation through radiative transition, the spin state is conserved, allowing the use of the optical emission to read out the spin states. Another competing relaxation transition exists through a non-radiative transition that does not conserve the spin state and adopts a long-lived singlet state. After the non-radiative transition and an illumination with the 532 nm green laser,
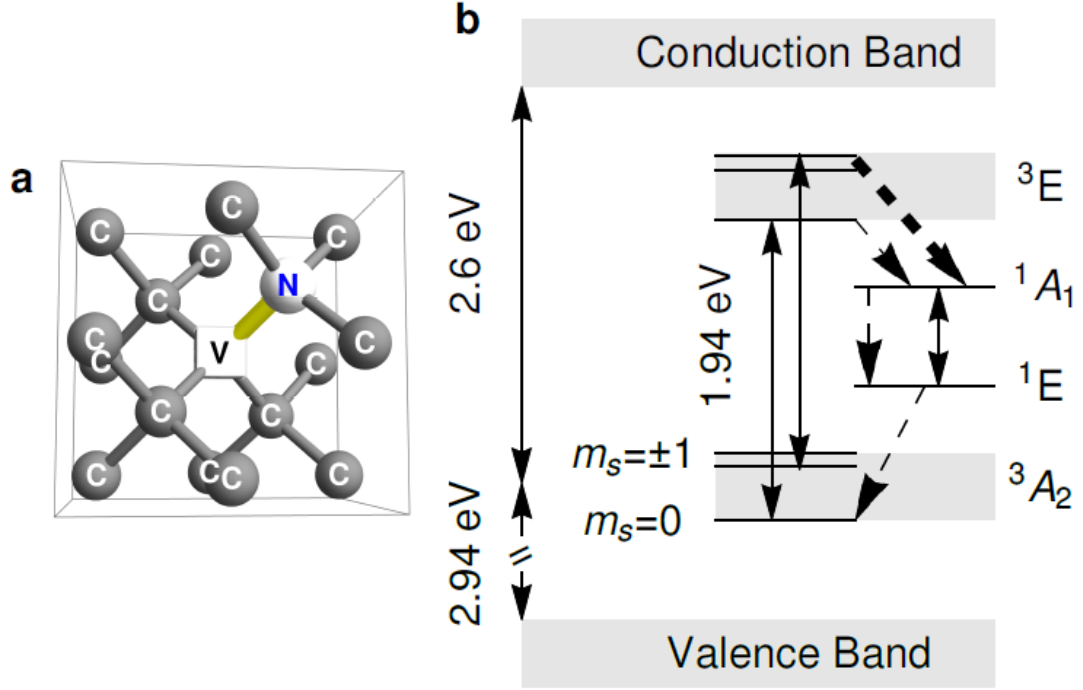
Fig. 1.2. (a) NV center in diamond crystal. In NV centers, a substituting nitrogen atom and a lattice vacancy are at neighboring positions. (b) NV$^-$ center energy level.

the NV$^-$ tends to be in the $m_s = 0$ state while the $m_s = \pm 1$ state in the excited state has a higher chance to access the singlet state compared to the $m_s = 0$ state [105]. This causes the $m_s = \pm 1$ state to stay longer in the long-lived singlet state, which leads to a reduction in fluorescence compared to that of $m_s = 0$ state [106]. After several cycles, the system is eventually brought to the $m_s = 0$ state [107, 108]. In short, the spin states can be assorted with a resonant microwave, and a green laser excitation and a red fluorescence can be used for read out and initialization of the spin states. In this thesis, the control of electron spin from levitated NV nanodiamonds is demonstrated with this optical interface.

Electron spin control has been previously achieved from optically trapped nanodiamonds in liquid and air [109–112]. The natural following step to produce a hybrid spin-optomechanical system would be the demonstration of the electron spin control

from a levitated diamond nanoparticle in vacuum. Once the diamond sample with embodied NV centers is trapped in high vacuum and the electron spin can be well controlled, an extrinsic magnetic field gradient would be able to exert a spin dependent force on the levitated diamonds. The NV electron spin will be able to sense and manipulate the motion of the levitated nanodiamonds in vacuum as it has been for clamped beams [87, 88]. Furthermore, a levitated nanoparticle in vacuum would have a much smaller mass and higher quality factor with the exclusion of mechanical contact to the environment and this would lead to a strong coupling between the motion of the trapped diamond and the NV spin, an important prerequisite to realize the aforementioned proposals. Moreover, once the nanodiamond is levitated in high vacuum, the nanodiamond will be able to be driven into a fast rotation [113, 114]. A fast mechanical rotation of the trapped diamond with electron spin will accumulate a quantum geometric phase [115] and potentially have applications in rotation sensing or as a quantum nanogyroscope [116].

In this thesis, a nanodiamond is levitated optically in low vacuum and the electron spin control of its embedded NV centers is demonstrated [117]. For a comprehensive understanding on the system, the effects from the air pressure, trap power, and different gas types are investigated. Also, the internal temperature of the trapped nanodiamonds are directly measured using the ESR.

## 1.5   Outline

This thesis includes the experimental research on the demonstration of an dumbbell-shaped nanoparticle torsion balance, a GHz nanomechanical rotor, and an ultrasensitive torque detector with optically levitated dielectric particles that have a nonspherical geometry. It also includes experimental work demonstrating the electron spin control from diamond nanoparticles optically trapped in low vacuum.

The reaminder of the dissertation is structured as the following. Chapter 2 describes a concise history of optical tweezers and the basic principles of optical trapping.

Next, chapter 3 discusses the experiments with optically levitated dumbbell-shaped silica nanoparticles in vacuum that builds a Cavendish torsion balance and a nanomechanical rotor [75]. Chapter 4 focuses on the experiment where the rotation rate of the levitated nanorotor is advanced further to above 5 GHz and an ultrasensitive torque sensor is acquired with the optically levitated nanorotors [83]. Chapter 5 introduces the work demonstrating the first control of electron spin from levitated diamond nanoparticles in a vacuum environment [117]. Finally, the thesis concludes with chapter 6 that contains concluding remarks and an outlook for relevant research.

# 2. PRINCIPLES OF OPTICAL TRAPPING

## 2.1 Introduction

In 1970, Arthur Ashkin demonstrated the first acceleration and trapping on dielectric microparticles in a fluid environment with the radiation pressure from a laser beam [8]. Succeeding the initial work, experiments led by Ashkin and Dziedzic used the optical forces of an upwards laser beam to counterbalance the gravity on microparticles and trap the particles in air and vacuum [9, 10]. The upward scattering force together with the confinement in the transverse directions from the gradient forces enabled levitation at pressures of about $10^{-6}$ torr [11] and the trapped particle was stabilized with feedback control [12]. Afterwards, in 1986, Ashkin was able to manifest the optical trapping of microparticles in liquid using a tightly focused beam where the gradient force overcomes the light's radiation pressure [13]. This optical dipole trap, or the optical tweezer, has played an imperative role in the advancements of fields of biophysics [118–121] and atomic, molecular and optical physics [122–124]. With his contributions to the realization of the optical tweezer, Arthur Ashkin was awarded the 2018 Nobel Prize in Physics.

While optical tweezers are typically used to trap and manipulate particles in a liquid environment, recent studies have begun using the optical tweezer in air and vacuum. Following the first demonstration optical levitation in high vacuum in 1976 [11], the field of levitated optomechanics has drawn broad interests for its great thermal seclusion from the surrounding environment. The optical levitation setups remove the mechanical contact to the surrounding thermal bath and the main source of decoherence for typical mechanical resonators is eliminated for the trapped dielectric particles. With the distinctive properties of the optical levitation experiments, many proposals and experiments have appeared for applications including precision

measurements [38,56,125], nonequilibrium thermodynamics [33,36,37], and quantum ground state cooling [65].

Before discussing the experimental details on the experiment, I will provide a brief introduction to the principles of optical trapping. The following will first discuss optical trapping with Ray optics where the object is significantly larger than the laser wavelength. Subsequently, optical forces will be explained for Rayleigh optics in which the object is significantly smaller than the laser wavelength. The gradient forces, scattering forces, and the optical potentials are discussed for spherical particles in a Gaussian laser. Finally, I will examine the optical trapping of nonspherical particles. The dynamics in the angular directions are compared with translational motions and the torque delivered to the particles in both linearly and circularly polarized laser beams are reviewed.

## 2.2 Ray Optics Approximation

The approximation of Ray optics holds when the radius of the spherical micropar-ticle to be trapped is considerably larger than the trapping laser wavelength. For example, Ray optics approximation is typically used when $R > 10\lambda_0$ where R is the radius of the microsphere and $\lambda_0$ is the laser wavelength in vacuum. The optical trap-ping in the Ray optics regime is explained with the momentum exchange between the laser and the trapped particle [13,126].

An illustration for the qualitative explanation for trapping with Ray optics ap-proximation is depicted in Fig. 2.1. Assuming there is no reflection from the surface of the micropshere, the microsphere would be trapped at the focus of the trapping laser. Once the sphere travels away from the focus the momentum exchange between the beam and the microsphere brings the object back to its original position. For instance, if the sphere moves to the right of the focus, the path of the photons pass-ing through the particle would deflect to the right because of the refraction of the laser beam. Therefore, a net force pushing the microsphere to the left would occur
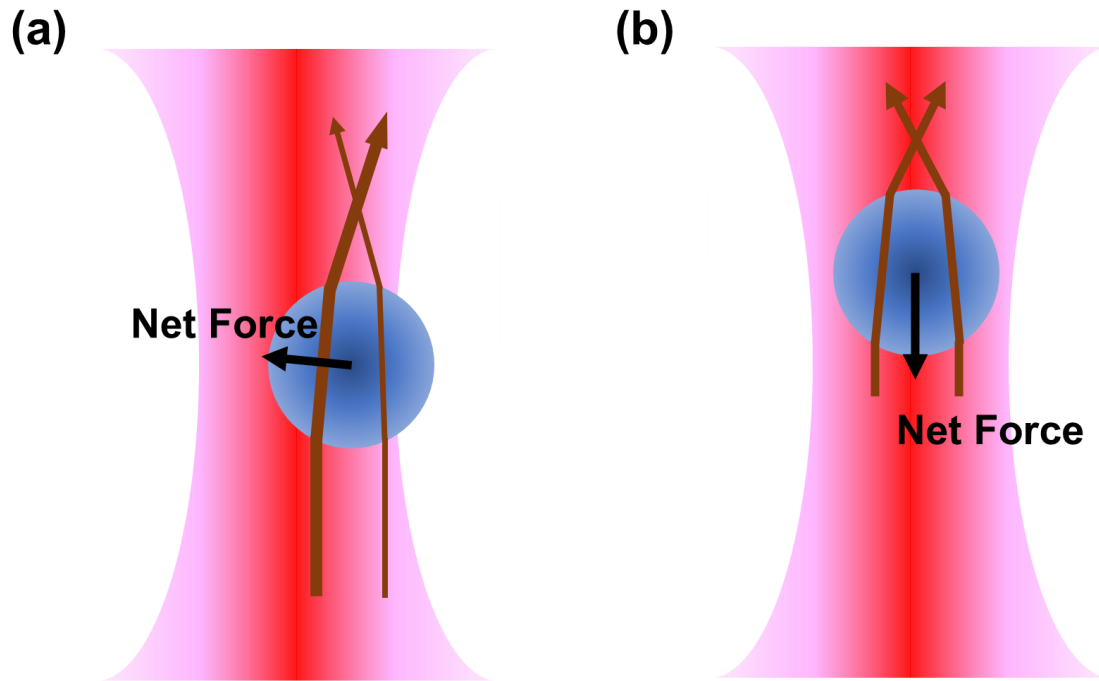
Fig. 2.1. Optical trapping with ray optics approximation. (a) When the microsphere moves to the right from the focus, the beam is refracted to the right and therefore the a resulting force pulls the microsphere back to the focus. The thicker line closer to the beam axis corresponds to stronger field. (b) When the microsphere moves forward into the laser beam propagation direction, the beam is focused stronger and the refraction generates optical force to pull back the particle to the laser focus. [127, 128]

moving the sphere backwards towards the focus of the trapping laser. On the other hand, if the sphere moves from the focus towards the laser propagation direction, the microsphere would cause the laser beam to be focused stronger and strengthen the forward momentum of the photons. Therefore, a counter force would push the microsphere back towards the opposite direction and closer to the beam focus. Since the sphere experiences a restoring force in all translation directions, the laser beam can stably trap the particle.

In real experiments, a reflection from the surface of the microsphere would affect the optical trapping. As a result of the surface reflection, the microsphere would be pushed into the laser propagation direction. If the reflection is small, it would result in the trapping of the microsphere at a position shifted towards to propagation direction from the focal point of the trapping laser. However, if the force from the reflection is stronger than the restoring force, the microsphere is cannot be stably trapped and is pushed away. For stable optical trapping, the reflection can be reduced by selecting a material that has a small refractive index compared to the medium or the restoring force can be increased by using a strongly focused laser with high numerical aperture (NA) lenses.

## 2.3    Rayleigh Approximation

The Rayleigh optics approximation is applied when the nanosphere radius is considerably smaller than the trap laser wavelength. Our experiments use silica or diamond particles with average size of about 100 nm or 150 nm in diameter and therefore can be approximated with the Rayleigh optics approximation. Typically, the Rayleigh optics approximation is used when $10R < \lambda_0$ and the particle is considered as an electric dipole. Therefore, the intensity gradient of the laser beam causes a force on the particle that leads to a force pulling the particle to the area where the light intensity is the highest, or in other words the focus of the beam. The second part of the forces is the scattering force which is results from the light scattering. When gradient force is dominant over the scattering force, the net force on the particle can become a three dimensional trap keeping the particle in a stable position.

Here, the optical forces on the spherical nanoparticle are analytically calculated with the theory of Rayleigh scattering [129]. Assuming the particle has a geometry of a sphere with a radius of $R$ and the dielectric constant $\varepsilon$ in a medium with refractive index of $n_m$, the induced dipole moment of the particle would be as follows [129]:

$$\mathbf{p} = 4\pi\varepsilon_m R^3 \left( \frac{\varepsilon_p - \varepsilon_m}{\varepsilon_p + 2\varepsilon_m} \right) \mathbf{E} = 4\pi n_m^2 \varepsilon_0 R^3 \left( \frac{n_r^2 - 1}{n_r^2 + 2} \right) \mathbf{E} \qquad (2.1)$$

Here, $\varepsilon_m$ is the dielectric constant of the medium, $\varepsilon_p$ is the dielectric constant of the particle, $\varepsilon_0$ is the dielectric constant in vacuum, $n_p$ is the refractive index of the trapped particle, $n_r = n_p/n_m$ is the relative refractive index of the particle, and the polarizability of the dielectric sphere is $\alpha = 4\pi n_m^2 \varepsilon_0 R^3 \left(\frac{n_r^2-1}{n_r^2+2}\right)$. From the definition of the dipole moment, the gradient force is $\mathbf{F} = (\mathbf{p} \cdot \nabla)\mathbf{E}$ [130, 131], and therefore the gradient force on the nanosphere is as follows:

$$\mathbf{F}_{grad} = \frac{\alpha}{2}\nabla\langle\mathbf{E^2}\rangle = 2\pi n_m^2 \varepsilon_0 R^3 \left(\frac{n_r^2-1}{n_r^2+2}\right)\nabla\langle\mathbf{E^2}\rangle = \frac{2\pi n_m R^3}{c}\left(\frac{n_r^2-1}{n_r^2+2}\right)\nabla I_L \quad (2.2)$$

since $\langle\mathbf{E^2}\rangle = \frac{I_L}{n_m \varepsilon_0 c}$, where $c$ is the speed of light and $I_L$ is the laser intensity. As a result, the potential can be expressed as below:

$$U = -\frac{2\pi n_m R^3}{c}\left(\frac{n_r^2-1}{n_r^2+2}\right)I_L \quad (2.3)$$

The scattering force from the beam on the spherical nanoparticle is [129]:

$$\mathbf{F}_{scatt} = \mathbf{z}\frac{n_m}{c}C_{scatt}I_L = \mathbf{z}\frac{128\pi^5 R^6}{3c\lambda_0^4}\left(\frac{n_r^2-1}{n_r^2+2}\right)^2 n_m^5 I_L \quad (2.4)$$

where $C_{scatt}$ is the scattering cross section and the laser propagation direction is in the $\mathbf{z}$ direction.

The total force on the nanosphere from the laser can be expressed as $\mathbf{F} = \mathbf{F}_{grad} + \mathbf{F}_{scatt}$ and therefore the minimum force along the $\mathbf{z}$ direction should be smaller than zero to establish a stable optical trap. As the gradient force scales with $R^3$ while the scattering force scales with $R^6$, the scattering is weakened more rapidly than the gradient force as the radius of the particle is reduced. Therefore, smaller nanospheres are easier to trap stably with an optical trap.

On the contrary, another prerequisite for stable trapping is to obtain a potential depth that is at minimum ten times greater than the average kinetic energy of the trapped sphere [13]. From the equipartition theorem, the average kinetic energy in each direction is $k_B T/2$ and $k_B$ is the Boltzmann constant and $T$ is the temperature of the surrounding medium. Therefore, in room temperature the potential depth should be larger than $1500\text{K} \cdot k_B$ to make a stable trap. Since the average kinetic energy

of the trapped sphere is independent to the particle size but the potential depth of the optical trap reduces with the particle size, particles that are too small become difficult to trap.

In experiments, the dielectric particles are trapped in air or vacuum with a 1550 nm laser focused with a high NA lens. The electric field of the Gaussian beam is defined with the paraxial approximation assuming the directions of $x$ and $y$ are perpendicular to the beam propagation and $z$ is in the beam propagation direction [132]:

$$\mathbf{E}(x, y, z) = E_0 \frac{\omega_0}{\omega(z)} e^{\frac{-(x^2+y^2)}{\omega^2(z)}} e^{i[kz-\eta(z)+k\frac{(x^2+y^2)}{2R(z)}]} \tag{2.5}$$

where abbreviations for beam radius ($\omega(z)$), wavefront radius ($R(z)$), and phase correction ($\eta(z)$) are as follows:

$$\omega(z) = \omega_0 (1 + z^2/z_0^2)^{1/2} \tag{2.6}$$

$$R(z) = z(1 + z_0^2/z^2) \tag{2.7}$$

$$\eta(z) = \arctan(z/z_0) \tag{2.8}$$

Since the NA of a Gaussian beam is NA $= \lambda_0/(\pi\omega_0)$, the waist can be expressed as $\omega_0 = \lambda_0/(\pi\text{NA})$ and the Rayleigh length can be approximated as $z_0 = \pi\omega_0^2/\lambda_0 = \lambda_0/(\pi\text{NA}^2)$.

Assuming that a spherical particle is positioned at the lowest part of the harmonic trap and the particle displacement is smaller than the Rayleigh length and beam waist, the gradient restoring force on the trapped object can be approximated to a linear form $F_{grad_j} = -k_j j$ where $j$ is the three translational directions. Using the laser intensity that can be described with the electric field amplitude and the laser power $I_L = n_m \varepsilon_0 c E_0^2/2 = 2P/(\pi\omega_0^2)$, the spring constant can be found for the Gaussian beam along the different axes:

$$k_{x,y} = \frac{\alpha E_0^2}{\omega_0^2} = \frac{4\alpha P}{\pi n_m \varepsilon_0 c \omega_0^4} = \frac{4\alpha}{\pi n_m \varepsilon_0 c} \left(\frac{\pi\text{NA}}{\lambda_0}\right)^4 P \tag{2.9}$$

$$k_z = \frac{\alpha E_0^2}{2z_0^2} = \frac{2\alpha P}{\pi n_m \varepsilon_0 c \omega_0^2 z_0^2} = \frac{2\alpha}{\pi n_m \varepsilon_0 c} \left(\frac{\pi\text{NA}}{\lambda_0}\right)^4 \text{NA}^2 P \tag{2.10}$$

From the spring constant above and the harmonic oscillator approximation, the potential for each direction can be found as $U_j = \frac{1}{2}k_j j^2$. Therefore, the oscillation frequency can be also found with $\omega_j^2 = k_j/m$ and $\alpha/m = \frac{3\varepsilon_0}{\rho} \frac{n_r^2-1}{n_r^2+2}$. The resulting oscillation frequencies along each axis for a spherical particle substantially smaller than the laser wavelength are as follows:

$$\omega_{x,y}^2 = \frac{4\alpha P}{\pi n_m \varepsilon_0 c \omega_0^4 m} = \frac{12}{\pi n_m c \rho} \left(\frac{n_r^2-1}{n_r^2+2}\right)\left(\frac{\pi \text{NA}}{\lambda_0}\right)^4 P \tag{2.11}$$

$$\omega_z^2 = \frac{2\alpha P}{\pi n_m \varepsilon_0 c \omega_0^2 z_0^2 m} = \frac{6}{\pi n_m c \rho} \left(\frac{n_r^2-1}{n_r^2+2}\right)\left(\frac{\pi \text{NA}}{\lambda_0}\right)^4 \text{NA}^2 P \tag{2.12}$$

In Fig. 2.2, the calculated gradient force and potentials of a silica spherical nanoparticle trapped in vacuum with a focused Gaussian beam is shown. The wavelength and power of the laser is 1550 nm and 500 mW, and the beam waist is selected to be 1.1 $\mu$m. The corresponding NA of this case is 0.45 and the Rayleigh length is 2.45 $\mu$m. The diameter of the trapped silica nanoparticle is 150 nm and the calculated potential is 46110 K which is enough to securely trap the particle in vacuum. For the trapped particle near the lowest position of the harmonic potential, the calculated oscillation frequency is approximately 123 kHz and 39 kHz in the radial and axial directions. The gradient force are smaller than zero for positive coordinates and larger than zero for negative coordinates in both radial and axial directions which push back the particle near to the focus of the laser beam. Finally, the scattering is smaller compared to the gradient force in axial directions, allowing the stable trapping of the silica nanosphere at room temperature.

## 2.4 Optical Trapping of Nonspherical Objects

This thesis focuses on the optical levitation of nonspherical particles with which torsional or rotational motions of the trapped particles are observed. An ellipsoidal particle can be considered as a simple model in this regard. The biggest difference from the case of a nanosphere and a nanoellipsoid is that in the latter case the polarizability is a tensor due to the different lengths of each axis, unlike the sphere
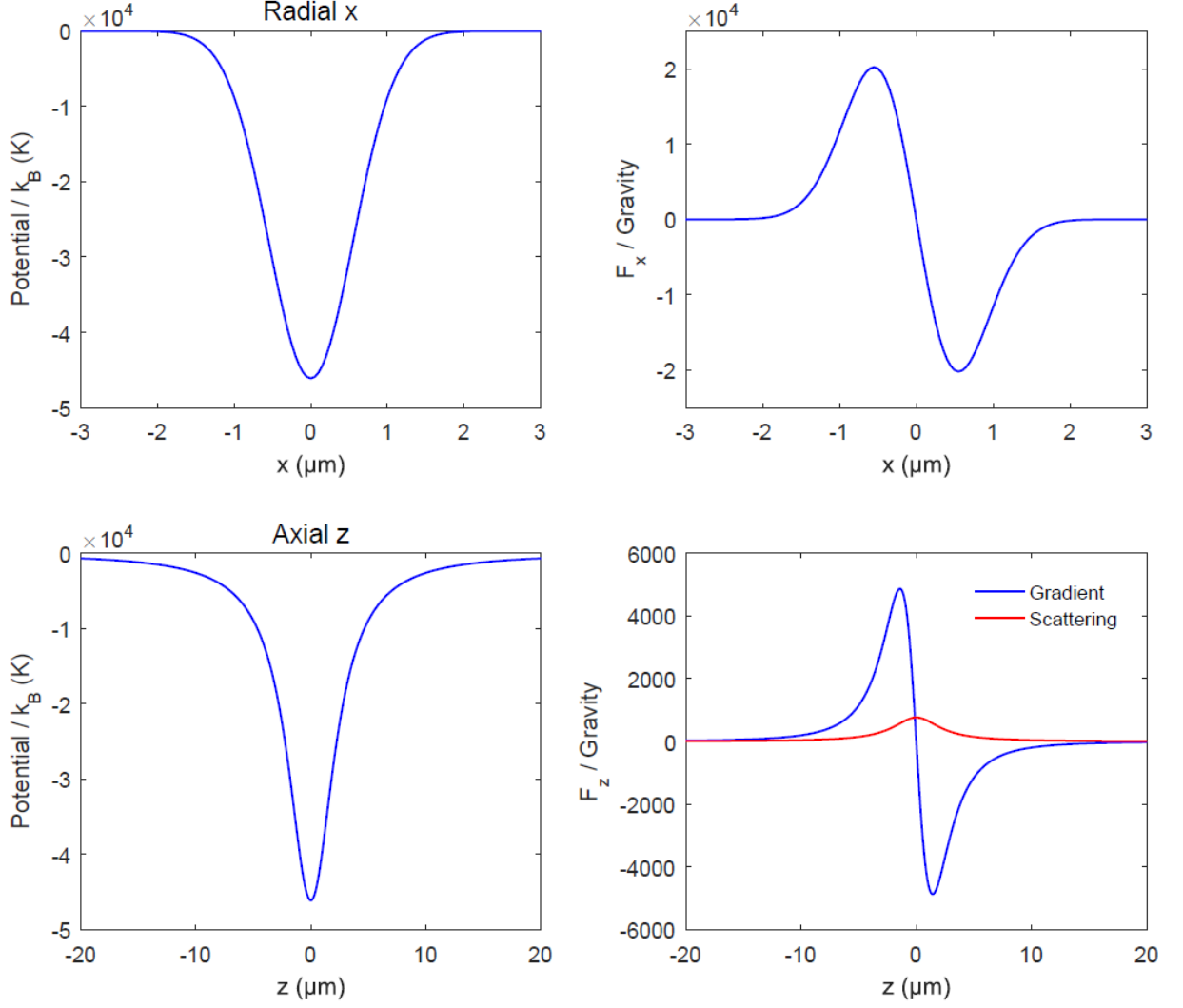
Fig. 2.2. Rayleigh optics. Optical potentials and forces of a 150 nm diameter spherical silica nanoparticle in vacuum. The wavelength and power of the trap laser is 500 mW and 1550 nm, and has a waist of 1.1 $\mu$m.

where the polarizability is simply a scalar value. The three half-axes of the ellipsoid have lengths of $a$, $b$, and $c$. The volume of the particle is $V = 4\pi abc/3$ and the polarizability along the $j$ axis is as follows in vacuum [130]:

$$\alpha_j = \frac{\varepsilon_0 V}{L_j + \frac{1}{n^2-1}} \tag{2.13}$$

and

$$L_1 = \int_0^\infty \frac{abc\,ds}{2(s+a^2)^{3/2}(s+b^2)^{1/2}(s+c^2)^{1/2}} \tag{2.14}$$

The equation for the geometrical factor $L$ can be applied for $L_2$ and $L_3$ by changing the values for the appropriate axes.

To examine the effect of the geometrical factor of the ellipsoid on the polarizability, the electric susceptibility is used to exclude the factor of volume:

$$\chi_j = \frac{\alpha_j}{\varepsilon_0 V} \tag{2.15}$$

The results in Fig. 2.3 are calculated assuming that the particle is a silica particle with two axes of $b$ and $c$ in relationship of $c = b$ or $c = b/2$. Results show the change of susceptibility as the length $b$ changes. The black curve is the electric susceptibility along the direction of $a$, the red along the $b$, and the blue along the $c$ of the ellipsoid. In the case where $b = c$, the susceptibility in directions of $b$ and $c$ are identical.
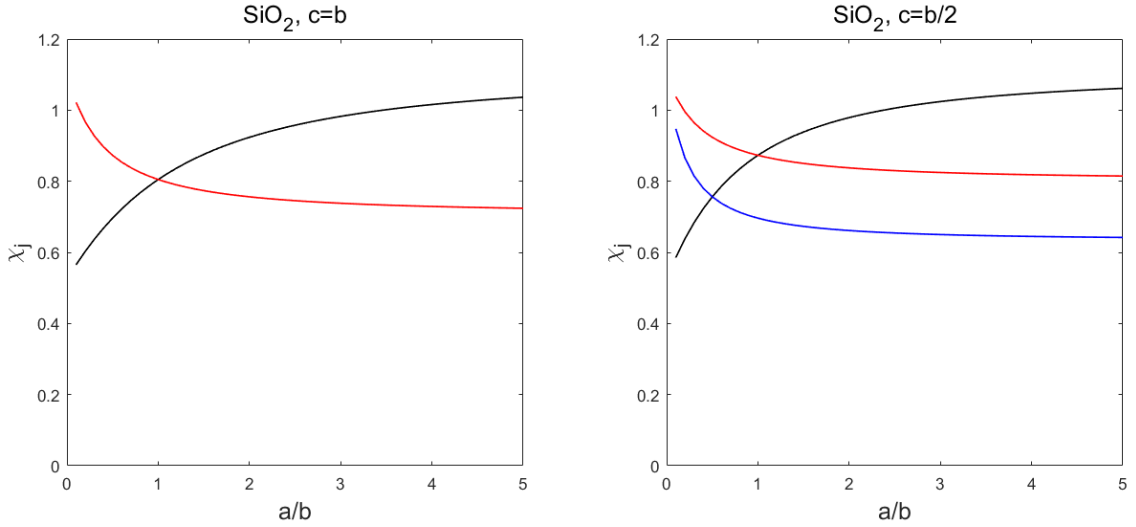


Fig. 2.3. Electric susceptibility versus geometry of ellipsoid. The black, red, and blue curves correspond to the directions of $a$, $b$, $c$, respectively.

For the calculations of optical gradient forces and potentials on an ellipsoidal silica nanoparticle, a prolate ellipsoid is used that has lengths of $a > b = c$, and assume the direction of the longer axis is the $x$ direction and one of the other axes to be the $y$ direction. The electric field is applied with the angle $\theta$ from the $x$ axis. Letting the particle to sit in the $x-y$ plane, the $E$ field will be expressed as $\mathbf{E} = E_0(\cos\theta\mathbf{x}+\sin\theta\mathbf{y})$ and the dipole moment $\mathbf{p} = E_0(\cos\theta\alpha_1\mathbf{x} + \sin\theta\alpha_2\mathbf{y})$. Therefore, the gradient force and the potential for an ellipsoid can be found as the following:

$$\mathbf{F}_{grad} = \frac{1}{2}(\alpha_1\cos^2\theta + \alpha_2\sin^2\theta)\nabla\langle\mathbf{E^2}\rangle = \frac{1}{2c\varepsilon_0}[\alpha_1 - (\alpha_1 - \alpha_2)\sin^2\theta]\nabla I_L \qquad (2.16)$$

$$U = -\frac{1}{2c\varepsilon_0}[\alpha_1 - (\alpha_1 - \alpha_2)\sin^2\theta]I_L \qquad (2.17)$$

Similar to the above, the gradient force and potentials can be calculated for the case of a silica ellipsoid in a focused Gaussian laser in vacuum. The calculations in Fig. 2.4 are done with a trapping laser with a wavelength and power of 1550 nm and 500 mW focused to a waist radius of 1.1 $\mu m$ at the focus. The length of the half axes of the silica ellipsoidal particle are 100 nm, 75 nm, and 75 nm. Results show sufficient values for a stable trap for silica nanoparticles with an ellipsoid geometry in a vacuum environment at room temperature.

Since the ellipsoidal particle have a polarizability in tensor form instead of a scalar value as in spherical particles, the torque exerted on the particle can be determined. The optical torque can be found from $\mathbf{M}_{opt} = \mathbf{p} \times \mathbf{E}$ [130, 131]. As in the above, $\mathbf{E} = E_0(\cos\theta\mathbf{x} + \sin\theta\mathbf{y})$ and the dipole moment is $\mathbf{p} = E_0(\cos\theta\alpha_1\mathbf{x} + \sin\theta\alpha_2\mathbf{y})$:

$$\mathbf{M}_{opt} = \mathbf{p} \times \mathbf{E} = \frac{1}{2}E_0^2(\alpha_1 - \alpha_2)\cos\theta\sin\theta = \frac{1}{4}E_0^2(\alpha_1 - \alpha_2)\sin2\theta \qquad (2.18)$$

The same results on the optical torque on the ellipsoid can be found from $M_{opt} = -\frac{dU}{d\theta}$:

$$\begin{aligned} M_{opt} &= -\frac{dU}{d\theta} = -\frac{1}{4}E_0^2(-2\alpha_1\cos\theta\sin\theta + 2\alpha_2\cos\theta\sin\theta) \\ &= \frac{1}{2}E_0^2(\alpha_1 - \alpha_2)\cos\theta\sin\theta = \frac{1}{4}E_0^2(\alpha_1 - \alpha_2)\sin2\theta \end{aligned} \qquad (2.19)$$

The optical torque can be calculated as shown in Fig. 2.5 according to the angle between the electric field from the laser beam and the longer axis of the ellipsoid. The
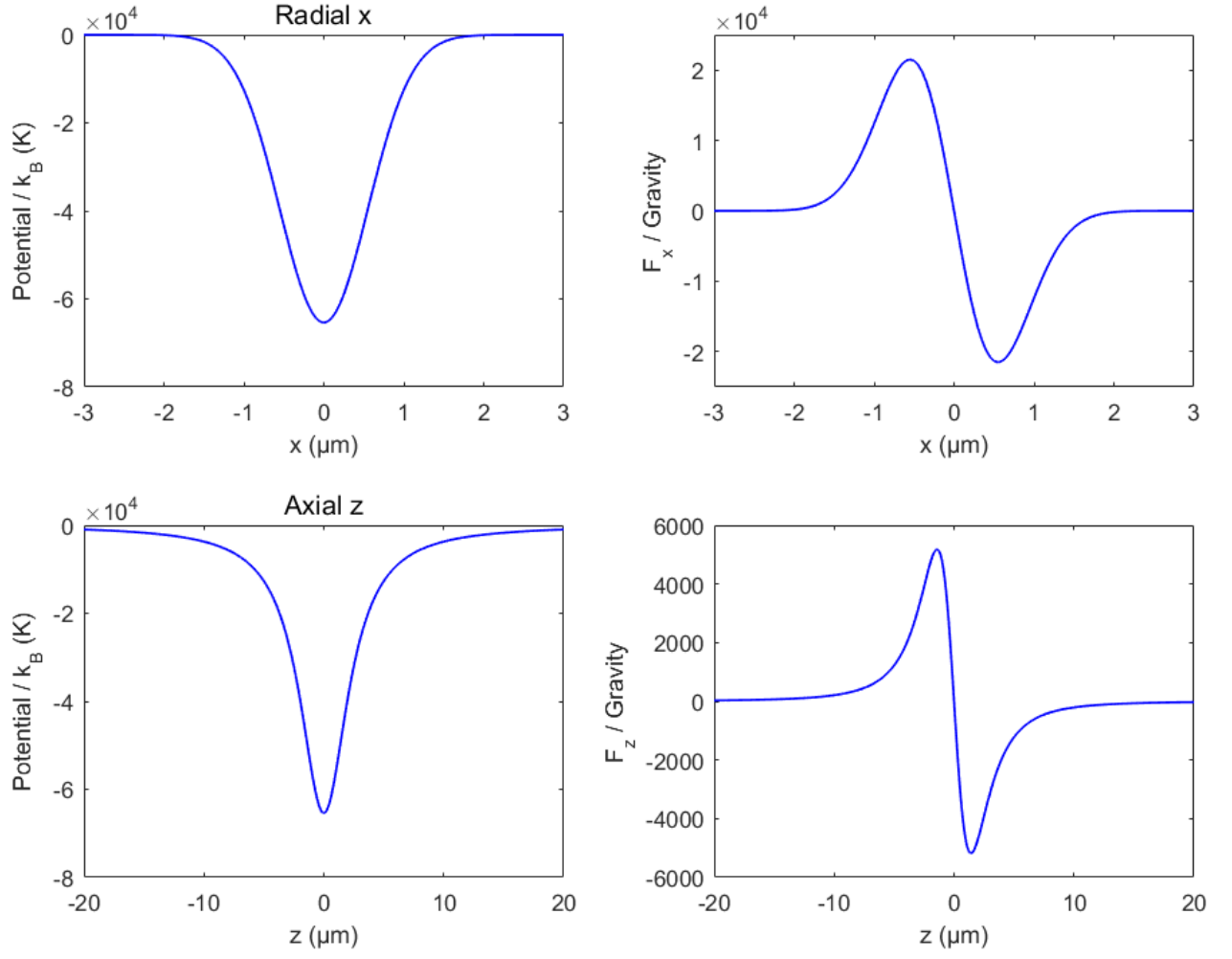
Fig. 2.4. Optical potentials and forces of an ellipsoidal nanoparticle in vacuum. The wavelength and power of the trap laser is 500 mW and 1550 nm, and has a waist of 1.1 $\mu$m. The half axes of the ellipsoid are 100 nm, 75 nm, and 75 nm.

torque has a period of $\pi$ since the torque is proportional to $\cos\theta\sin\theta$ and is expected due to the geometrical symmetry of the ellipsoid used for the calculations.
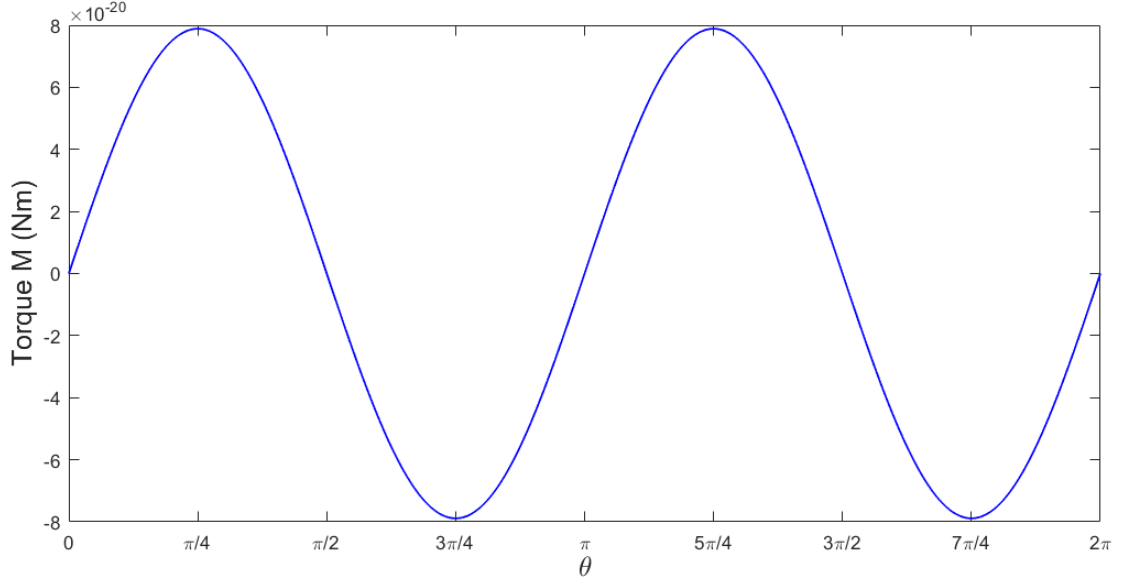
Fig. 2.5. Optical torque on an ellipsoidal nanoparticle in vacuum. The wavelength and power of the trap laser is 500 mW and 1550 nm, and has a waist of 1.1 $\mu$m. The half axes of the ellipsoid are 100 nm, 75 nm, and 75 nm.

If the ellipsoid is trapped in a Gaussian beam that is linearly polarized where the change in angular orientation of the ellipsoid is small, the torsional vibration frequency can be found. From Eq. 2.18 and Eq. 2.19, the optical torque is as follows:

$$M_{opt} = \frac{I_L}{2n_m\varepsilon_0 c}(\alpha_1 - \alpha_2)\sin 2\theta \tag{2.20}$$

Under the approximate for small angle $\sin 2\theta = 2\theta$ and therefore:

$$M_{opt} = \frac{I_L}{n_m\varepsilon_0 c}(\alpha_1 - \alpha_2)\theta \tag{2.21}$$

From Eq. 2.21, the spring constant and oscillation frequency for the torsional vibration can be found as:

$$k_\theta = \frac{I_L}{n_m\varepsilon_0 c}(\alpha_1 - \alpha_2) = \frac{2P}{\pi n_m\varepsilon_0 c\omega_0^2}(\alpha_1 - \alpha_2) = \frac{2(\alpha_1 - \alpha_2)}{\pi n_m\varepsilon_0 c}\left(\frac{\pi\text{NA}}{\lambda_0}\right)^2 P \tag{2.22}$$

$$\omega_\theta^2 = k_\theta/I_m = \frac{10P(\alpha_1 - \alpha_2)}{\pi n_m \varepsilon_0 c \omega_0^2 \rho V(a^2 + b^2)} = \frac{10P(\chi_1 - \chi_2)}{\pi n_m c \omega_0^2 \rho(a^2 + b^2)}$$
$$= \frac{10(\chi_1 - \chi_2)}{\pi n_m c \rho(a^2 + b^2)} \left(\frac{\pi \mathrm{NA}}{\lambda_0}\right)^2 P \tag{2.23}$$

where $I_m = \frac{1}{5}m(a^2 + b^2)$ is the moment of inertia of the ellipsoid.

For comparison between the torsional vibration and the translational motion of an optically trapped ellipsoid, the motion along the y direction and the vibration around the z axis can be compared. In Fig. 2.6, the trapping potential is compared between a function of the position in the y when the ellipsoid has an orientation of $\theta = 0$ and a function of $a\theta$ when the ellipsoid is at position $y = 0$. In order to plot the two potentials together, $U_\theta$ is plotted as a function of $a \cdot \theta$ which describes the distance the apex travels. The potential in the transverse direction has a Gaussian form because of the spatial profile of the Gaussian beam while the potential in the angular direction is sinusoidal as can be expected from Eq. 2.17. Here, the $U_\theta$ has several periods within the waist of the trapping laser and therefore the torsional vibration with higher frequency compared to the translational motion can be expected.

The oscillation frequency in the translation directions for an ellipsoid can be found similarly to the method used to calculate it for the spheres, and the oscillation frequencies for the ellipsoid are as follows:

$$\omega_{x,y}^2 = \frac{4\alpha_1 P}{\pi n_m \varepsilon_0 c \omega_0^4 m} = \frac{4\chi_1 P}{\pi n_m c \rho \omega_0^4} \tag{2.24}$$

$$\omega_z^2 = \frac{2\alpha_1 P}{\pi n_m \varepsilon_0 c \omega_0^2 z_R^2 m} = \frac{2\chi_1 P}{\pi n_m c \rho \omega_0^2 z_R^2} \tag{2.25}$$

When the oscillation frequency in the $y$ is compared to torsional vibration in $\theta$, the ratio of $\omega_\theta/\omega_y$ scales with $\omega_0/a$ and since $a$ is typically smaller than $\omega_0$, the torsional vibration has a higher frequency compared to the translational motions. Furthermore, while the COM does not depend on the ellipsoid size, the torsional vibration frequency increases as the ellipsoid becomes smaller. Also, as the ratio of $b/a$ becomes smaller, the ratio of $\omega_\theta/\omega_y$ can be increased leading to potential advantages for torsional ground state cooling [41].
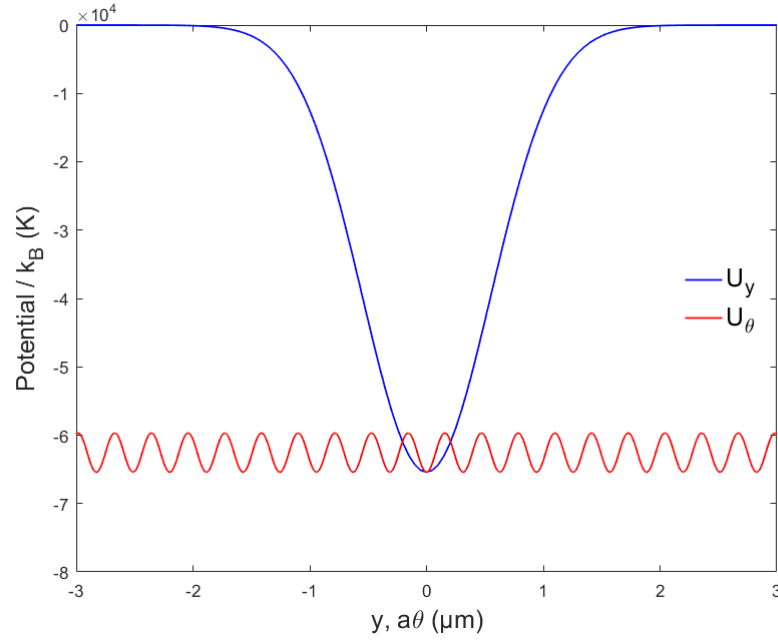
Fig. 2.6. The transverse ($U_y$) and angular ($U_\theta$) direction trapping potentials. The wavelength and power of the trap laser is 500 mW and 1550 nm, and has a waist of 1.1 $\mu$m. The half axes of the ellipsoid are 100 nm, 75 nm, and 75 nm.

While the calculations from this section inform us on the characteristics of the optically trapped particles including the optical potential, gradient forces, spring constants and oscillation frequencies, the observed values in the real experiments may differ from our calculations. For example, the oscillation frequencies along the $x$ and $y$ are calculated to be the same in the above, but a tightly focused laser beams with linear polarization have an elongated field distribution along the polarization direction and therefore the trapping frequency is slightly smaller along the polarization than along the other transverse direction. Also, if the optically trapped particles undergo a large oscillation, the motion can become anharmonic and the nonlinearities would need to be considered with the higher derivatives of the potential [33, 133, 134].

## 2.5 Rotation of Nonspherical Particles in Circularly Polarized Laser

As found from the previous section, nonspherical particles in a linearly polarized laser tries to align its longer axis to the polarization axis of the beam in order to reach a minimum potential energy. As the long axis strays from its equilibrium position, due to Brownian motion, the particle experiences a torque to push back the axis towards its equilibrium position. Therefore, the nonspherical particle in a linearly polarized laser exhibits a torsional vibration [41, 71, 135].

On the contrary, in a circularly polarized laser the nonspherical particle is driven into a free mechanical rotation. The circularly polarized light delivers a torque via spin angular momentum transfer from the light scattering [26, 70, 71, 73, 80, 136]. With the polarization anisotropy due to the geometry of the particle, the nonspherical particles experiences a torque similar to that of which a birefringent particle would encounter [16, 67, 68]. The rotation can be controlled by either the laser intensity, ellipticity of laser polarization, or with the particle geometry, and this adds the ability to control the angular DOF to the field of levitated optomechanics which has been previously focused mainly on the COM DOF.

As the particle is trapped in air and vacuum, the air drag torque decreases with the lower pressure. Once the optical torque exceeds the drag, the particle can start a free mechanical rotation and the rotation speed of the rotating particle is decided with the balance between the optical and drag torque acting on the trapped particle. Therefore,

$$\omega_{rot} = M_{opt}/(I_m \gamma) \tag{2.26}$$

where $\omega_{rot}$ is the rotation speed and $\gamma$ corresponds to the rotational damping rate. The rotational damping rate is proportional to pressure. Consequently, the rotation rate is inversely proportional to pressure, $\omega_{rot} \propto 1/p$. As the pressure is lowered, rotations exceeding 1 GHz have been observed [75, 80, 83] and such rapid rotations has the potential to investigate material properties or measure vacuum friction.

# 3. TORSION BALANCE AND GHZ NANOMECHANICAL ROTOR WITH OPTICALLY LEVITATED DUMBBELL-SHAPED NANOPARTICLES

## 3.1  Introduction

With its excellent isolation from the surrounding environment, systems of levitated optomechanics have drawn large interest for its potential in precision measurements. Previous experiments have exploited levitated particles to demonstrate remarkable force sensitivity [38, 56], acceleration sensitivity [70], and search for millicharged particles [125]. Also, there have been numerous proposals to use levitated particles to study interactions related to dark energy [44], non-Newtonian gravity [45], and test objective collapse models [48, 51].

While the COM motion of levitated particles have been studied extensively, the experimental studies on torsional vibrations of the particles has recently begun. In a previous study from our group, we have experimentally observed the torsional vibration of levitated nonspherical nanodiamonds in low vacuum for the first time [41]. Since the nanoparticles that were trapped in the system had an irregular geometry and were significantly smaller than the trap laser wavelength, a model of a nano-ellipsoid with a polarizability of a tensor form could be used to explain the detected torsional motion. Within a linearly polarized trapping laser such a particle would align its longer axis to the direction of polarization in order to minimize its potential energy. Once the particle strays from the angle of equilibrium position, it would experience a torque pushing the particle back to its original orientation, and therefore, exhibit a torsional vibration.

With the irregularly-shaped nanodiamonds trapped in low vacuum, we were able to observe torsional vibrations at frequencies of approximately one order higher than

that of COM motions. The higher frequencies are potentially beneficial in regards of the achievement of ground state cooling of the angular DOF. However, to bring the torsional motion to its ground state, the particle needed to be trapped in higher vacuum which is a factor limiting our previous experiments. The nanodiamonds were lost at a pressure of a few torr due to the increase in temperature of the trapped nanodiamond particle with less air molecules in the surrounding environment [112, 137].

Moreover, the nonspherical particle optically levitated in vacuum can have an analogy to a torsion balance similar to the system Cavendish used to demonstrate the first experiments on gravitational forces in the laboratory [138]. The nanoscale system with a levitated nanoparticle is anticipated to reach torque sensitivities several orders higher than the state-of-the-art sensors [139, 140] once it reaches ultrahigh vacuum. The optically levitated torsion balance would enable the rare opportunities for the detection of Casimir torque [77, 141, 142], and tests on quantum gravity [79, 143, 144]. However, in our previous study, the trapped diamonds had a geometry differing on each trapped particle. In order to utilize the trapped particle as a torsion balance, the geometry of the particle needs to be understood to calibrate the torque measurements.

Therefore, in this work, an essential part is to trap the nonspherical particles with a well-defined geometry and at lower pressures. While there have been previous work using particles with a nanorod geometry, particles have been generally lost before reaching pressures below 1 torr [71, 72]. In order to manage higher vacuum, I replace the material of the optically trapped particle to silica that is already well known to survive lower pressures for its low absorption at wavelengths of the trapping laser [11, 60, 145]. Based on the proposal to use the nonspherical particle as an ultrasensitive torsion balance, a silica nanoparticle with a dumbbell geometry is used throughout the experiment. The well-defined nonspherical geometry of the trapped dumbbell-shaped nanoparticles allows the calculations on the minimum torque sensitivity the levitated torsion balance would be able to reach. The silica dumbbell-shaped nanoparticles are synthesized using two separate methods [146].

The replacement of the material allowed the nonspherical nanoparticles to be trapped in high vacuum without loss caused by heating. While former work have demonstrated rotations of about 10 MHz [68, 70, 72], the ability to trap dumbbell-shaped nanoparticles in high vacuum opened up the opportunity to rotate the nanoparticles at higher speed with lower drag torque at lower pressures. Using a circular polarization for the trapping beam, the dumbbell-shaped nanoparticles could be rotated at rates higher than 1 GHz, achieving the fastest manmade rotor [80]. With such fast rotations, the material properties of nanoparticles in extreme conditions could also be examined [73, 82].

## 3.2   Experimental Apparatus

To study levitated optomechanics with nanoparticles in air and vacuum, our group has designed an optical tweezer within a vacuum chamber as shown in Fig. 3.1. The simplified schematic of the trapping and the detection of the particle motion is provided in Fig. 3.2. In the following, the experimental setup of the optical levitation system, two methods for the silica dumbbell-shaped nanoparticle sample synthesis, and the loading of the samples to the optical trap are described.

### 3.2.1   Optical Levitation System

For the isolation from unwanted mechanical vibrations, the overall optical setup is designed on an optical table (Newport RS2000). The optical table is supported with pneumatic vibration isolators (Newport S-2000A) which provides further isolation from the environmental vibrations. With the optical table that is air floated, the vibration amplitude can be decreased by approximately three orders of magnitude. Therefore, the use of optical tables with pneumatic vibration isolators is imperative to avoid performance degradation and unwanted drifts in the beam path.

A 1550 nm ultralow noise laser (NKT Photonics, Koheras Adjustik C15) and a power amplifier (NKT Photonics, Koheras Boostik HPA) is used as the trapping light
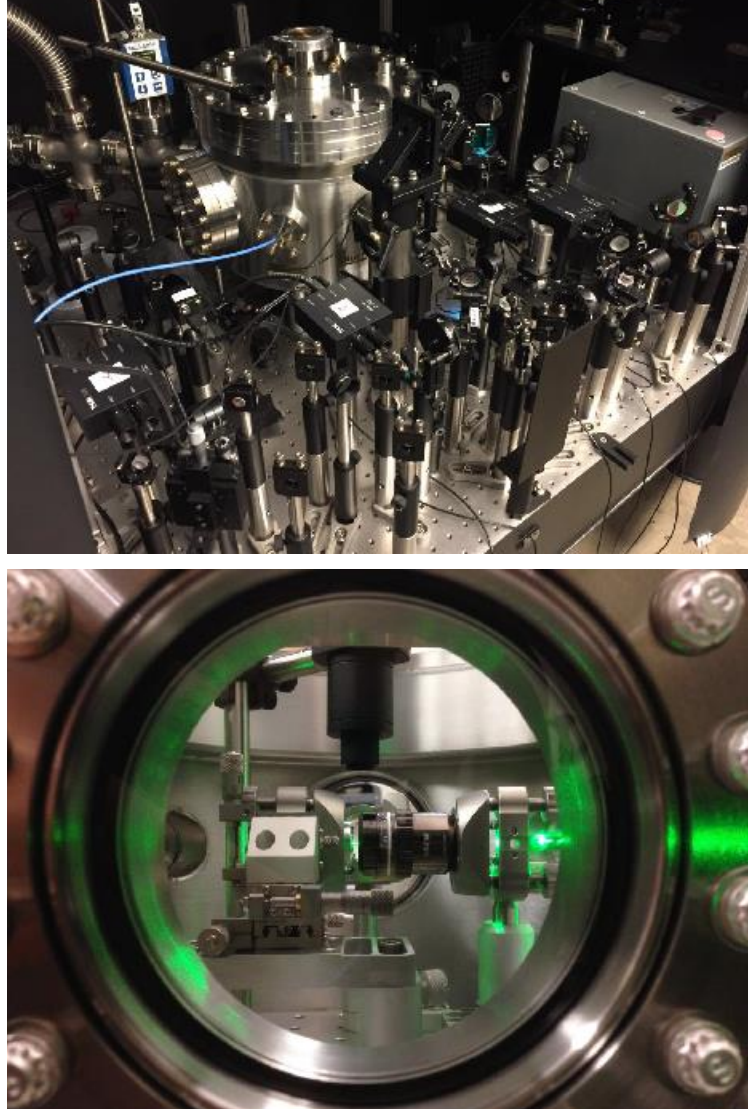
Fig. 3.1. Experimental apparatus. Top figure shows picture of the overall system. Lower figure shows picture of the objective lens and collimating lens inside the vacuum chamber. Tube on top guides the nebulized nanoparticles to the trap site.

source. After the air-spaced doublet collimator (Thorlabs F810APC-1550), a quarter waveplate controls the polarization of the trap laser which is initially linearly polarized. The beam is focused with an air objective lens (Olympus LCPLanN 100x, NA 0.85) located inside a custom designed vacuum chamber. To form a single beam optical tweezer, it is important that the trapping laser completely fills the rear aperture
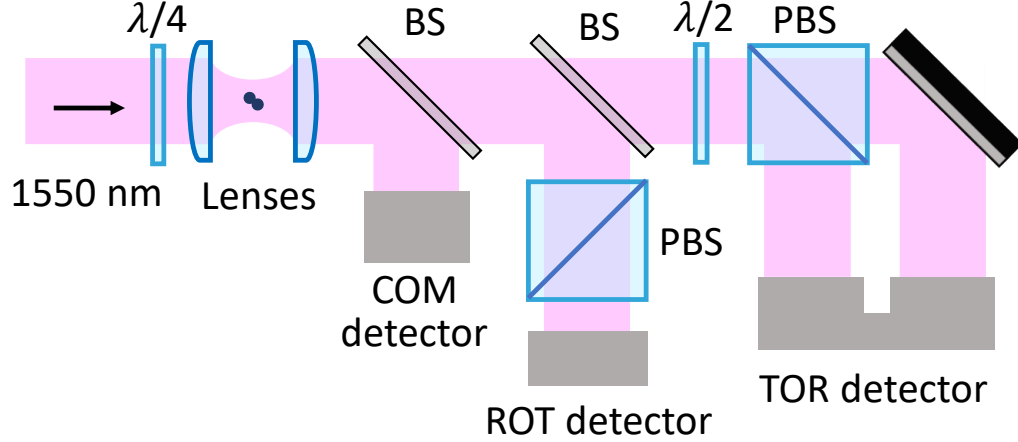
Fig. 3.2. Simplified schematic of trapping and detection system. $\lambda/4$ - quarter waveplate, BS - beam splitter, $\lambda/2$ - half waveplate, PBS - Polarizing beam splitter, COM - Center of Mass motion, ROT - Rotational motion, TOR - Torsional motion.

of the objective lens. With the optical trap inside a vacuum chamber, the levitation experiments can be held both in air and vacuum. Following the objective lens and the trapping site of the optical trap, also inside the vacuum chamber, an additional aspheric lens (Thorlabs C660TME-C, NA 0.6) is used to collimate the focused laser beam. Finally, after the vacuum chamber, the trapping laser is collected with fast balanced photodetectors (Thorlabs PDB 410C, PDB 420C, PDB480C-AC) to record the motion of the optically trapped particle. An additional 532 nm laser (Laserglow LLS-0532) is overlapped with the 1550 nm laser, and the scattering from the particle in the optical trap is observed with a camera (Pointgrey BFLY-U3-032M-CS) on the side. The trapping process can be observed with the scattering light and the camera.

### 3.2.2 Vacuum System

A custom designed vacuum chamber is connected to a turbo-molecular vacuum pump (Pfieffer Hicube 80) with a valve in between shown in Fig. 3.3. The rate at which the pressure is lowered can be controlled with this valve. To avoid mechanical
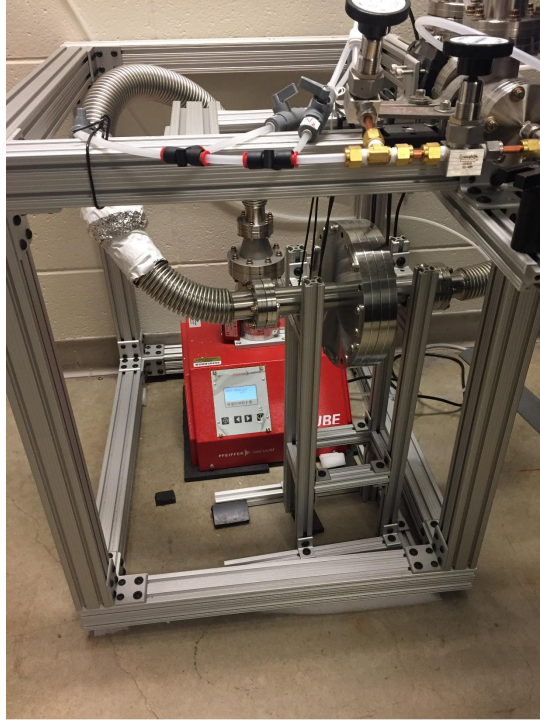
Fig. 3.3. Vacuum System. Turbo-molecular pump and structure to reduce vibration. Valves are used for control of pressure inside vacuum chamber.

vibration affecting the optical experiments in the vacuum chamber, stainless steel bellows are used to connect between the pump and the experimental chamber. Additionally, a metal structure is made to clamp the valve and bellows onto the structure. With the turbo-molecular pump alone, the lowest pressure achieved in the system is about $2 \times 10^{-5}$ torr without bakeout. The system is later modified to achieve higher vacuum.

For the reading of the pressure inside the vacuum chamber two pressure gauges are used. At relatively high pressures, a vacuum transducer (MKS 910 DualTrans) with a power supply and display (MKS PDR900) is used. This transducer uses a Piezo and a Pirani sensor to allow pressure measurements for a wide range. The Piezo acts as an absolute pressure sensor that measures from 1 to 1500 torr regardless of gas type. The Pirani gauge allows pressure measurements at as low as $10^{-5}$ torr. In our

system, for pressures below 50 mTorr, an ion gauge (Kurt J. Lesker KJLC354) is used. The pressure of the vacuum is measured with a hot cathode ionization gauge by measuring the quantity of ions produced while the gas atoms and molecules in are ionized. The ion gauge has two options for emission current, 4 mA or 100 $\mu$A. From $5 \times 10^{-6}$ to $5 \times 10^{-2}$ torr, the 100 $\mu$A is preferred, while at lower pressures of $10^{-9}$ to $5 \times 10^{-4}$ torr, the use of 4 mA is recommended. The ability to lower and read out the pressure while the nanoparticles are trapped throughout the experiment allow the observations and accurate measurements of the torsional and rotational motions in the vacuum environment.

### 3.2.3   Detection System
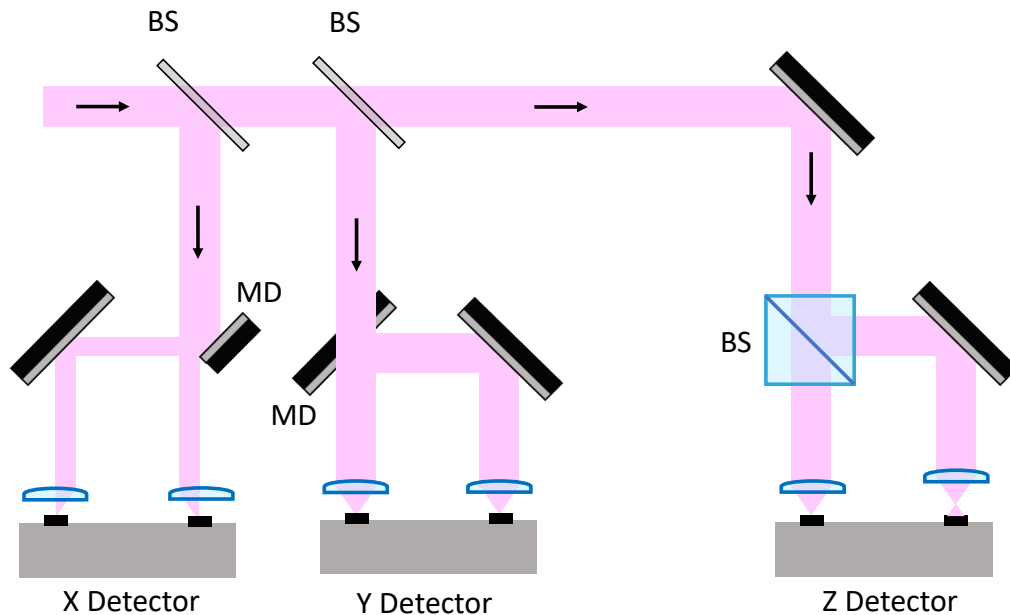


Fig. 3.4. COM detection system. Simplified schematic of the detection scheme of COM detectors. The detection in the X and Y are allowed with a D shaped mirror (MD) that allows detection of the two halves of the beam and measure the difference between the two. The Z detection is measured with the variation of the beam waist.

The particle's COM motion is observed by detecting the intensity modulation of the interference between the scattering and the trapping beam. As in the above, the trap laser is collimated after the trapping site with an aspheric lens and is aligned to fast balanced photodetectors. For the COM detectors, we use photodetectors of a bandwidth of 75 MHz (Thorlabs PDB 410C for Z) and 100 MHz (Thorlabs PDB 420C for X and Y) and the active detector diameter of the detectors are 0.3 mm. Since the trapping laser is used for the detection of motion of the particles, an InGaAs/PIN detector that has wavelength range of 800 to 1700 nm is chosen. As shown in Fig. 3.4, the particle displacement in the X and Y directions are measured with D shaped mirrors that are located in front of the balanced detectors to divide the beam in horizontal and vertical directions, respectively. Due to the difference in travel lengths, the two beams resulting from the reflection and transmission past the D shaped mirrors have different phase at the two photodetectors of each balanced detector. This phase difference is converted to an intensity change through the interference with the unscattered part of the trapping beam. Since the phase is proportional to the particle's lateral position, the output signal of the X and Y detectors are also proportional to the particle's position in X and Y. The Z motion is detected by the variation in the focus of the scattered light as the longitudinal position of the trapped object changes. While one of the detectors collects the total beam power for a reference, the lens position in front of the other detector is altered so that it measures the total intensity change from the interference of the transmitted light and the scattering. As the particle moves in the Z, the scattered light focuses and defocuses minutely. This change in focus of the scattered light, again, is converted to an intensity difference with the interference to the unscattered laser. For all three COM detection schemes, the two optical inputs of the balanced detector are subtracted from each other in order to rule out the common mode noise. Also, for small displacements, the difference in the two inputs of the beam is proportional to the particle position, and provides a detection scheme with exceptional spatial and temporal resolution [147, 148].

The torsional vibration and the rotation is also measured with a similar scheme. In this experiment, the torsional vibration of the trapped nanoparticle is observed when the trapping laser is set to a linear polarization. During a torsional motion, the orientation of the trapped particle changes and alters the polarization of the laser. This change in polarization is exploited to monitor the torsional vibration of the optically trapped particle [18, 19, 68].

A polarizing beam splitter (PBS) and a half waveplate is positioned in front of the balanced detector as shown in Fig. 3.2. As the particle changes the polarization of the transmitted laser, the power reaching the two photodetectors varies and can be monitored with the photodetector. The rotation of the particle is observed with similar physics, but the input beam is changed to circular polarization. Additionally, a photodetector with a higher bandwidth of 30 kHz to 1.6 GHz is used (Thorlabs PDB480C-AC) and the output signal is connected to an amplifier (Minicircuit ZKL-2+) and a spectrum analyzer (Tektronix RSA306) to observe the rotations up to 1 GHz in the dumbbell-shaped nanoparticles. A sample of the measurements is shown in Fig. 3.5. The peak shown in this figure corresponds to twice the mechanical rotation rates due to the symmetrical geometry of the dumbbell-shaped nanoparticles used in the experiments. In the experiments, the rotation signal were observed at up to about 1.1 GHz, and this frequency was only restricted by the bandwidth of the balanced detectors.

The collected signal from all the photodetectors other than the rotation detector is directed to a data acquisition (DAQ) card (Gage Octupus Compuscope 8384) that has a sampling rate of up to 50 MS/s and 14 bit vertical resolution. With the DAQ card, the data is digitized and stored on a computer. The output of the rotation photodetector is connected to the spectrum analyzer which saves the data onto the computer.
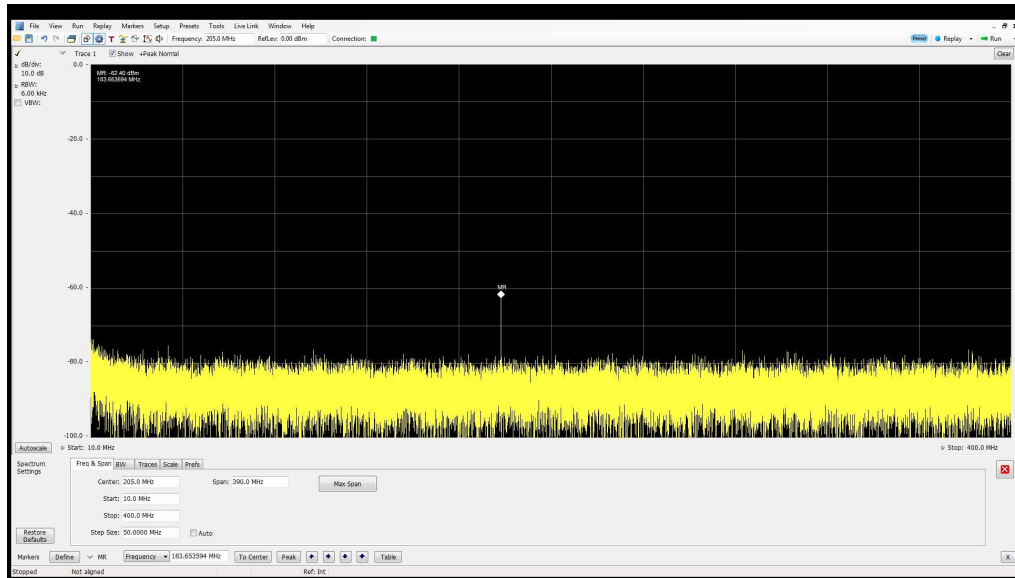
Fig. 3.5. Sample of rotational data measurement with a Tektronix RSA306 spectrum analyzer. The signal observed at approximately 184 MHz corresponds to a rotation frequency of about 92 MHz.

### 3.2.4 Sample Synthesis and Loading

As mentioned in the above, in order to make an analogy to a torsion balance a nonspherical particle with a well-defined geometry has to be trapped. The geometry of the particle needs to be understood for the calculation of the minimum torque sensitivity of the optically levitated torsion balance. To satisfy the conditions of having a nonspherical particle and a particle with a known geometry, a dumbbell-shaped nanoparticle geometry is selected as depicted in Fig. 3.6 (b). Moreover, to achieve optical trapping in lower pressures, the material is chosen to be silica. The silica dumbbell-shaped nanoparticles used in the experiments are synthesized with two separate methods.

The first method is to use a chemical synthesis of silica dumbbell-shaped nanoparticles [146]. Our colleagues have used this chemical process to mass produce the silica dumbbell-shaped nanoparticles and with a tunable aspect ratio. By controlling the interpenetration of the two spheres the aspect ratio is tuned. In Fig. 3.6(a), the
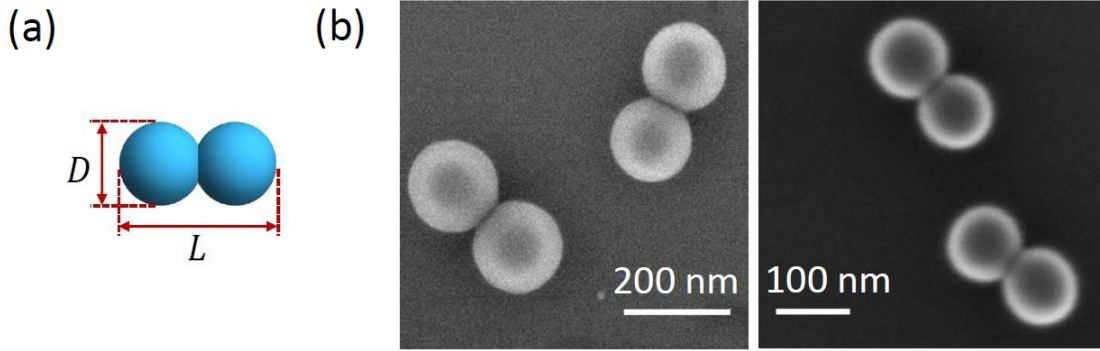
Fig. 3.6. (a) Dumbbell geometry of the silica nanoparticles. D - Diameter of one sphere of dumbbell-shaped nanoparticle, L - Length of dumbbell-shaped nanoparticle. (b) SEM images of dumbbell-shaped silica nanoparticles with varied sizes.

length of the dumbbell-shaped nanoparticle is defined as L and D as the diameter of one sphere of the dumbbell-shaped nanoparticle to define the aspect ratio as (L/D). The typical process for chemical synthesis is shown in Fig. 3.7. First, cores of the silica particle with a diameter of $(L - D)$, 80 nm in this case, are synthesized with 1 mL of tetraethyl orthosilicate (TEOS) in a solution of 4.86 mL of ammonia, 2.98 mL of ultra-pure water and 100 mL ethanol while stirring the solution. After 48 hours of stirring, a solution with silica nanospheres of a diameter of approximately 80 nm are made. Here, an additional 10 mL of acetone is added and the solution is stirred for another 24 hours for aggregation and 20 $\mu$L of TEOS is added while the solution is stirred for another 24 hours in order to grow the silica shells. To obtain the precipitates of the silica dumbbell-shaped nanoparticles the solution was washed with ethanol and centrifuges at 9000 r.p.m. for 10 minutes. In order to purify the sample, the dumbbell-shaped nanoparticles were cleaned with seven cycles of washing processes and was dispersed to 40 mL of anhydrous ethanol. The solution was heated at 90 °C for 12 hours in a Teflon-lined stainless steel autoclave. The supernatant is collected after 10 minutes of centrifugation at 1000 r.p.m. and centrifuged at 9000 r.p.m. for another 10 minutes so that the impurities could be removed. Finally, the sample is dried under room temperature in vacuum overnight and the final sample

is obtained. This chemical process can produce a large amount of dumbbell-shaped nanoparticles and can tune the aspect ratio by changing the distance penetrated between the two spheres. However, the process is demanding and time consuming. SEM images of two different sized dumbbell-shaped nanoparticles are shown in Fig. 3.6(b).
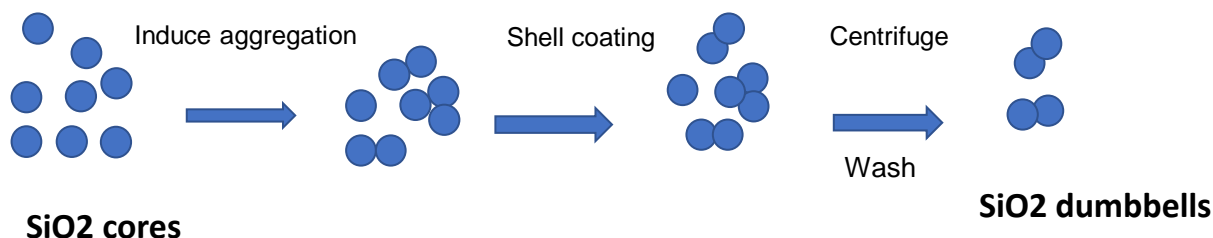


Fig. 3.7. Chemical synthesis of silica dumbbell-shaped nanoparticles.

A simpler procedure to synthesize dumbbell-shaped nanoparticles that was used throughout the experiment was to use a physical method to assemble the silica dumbbell-shaped nanoparticles. The typical process is as follows. A solution of silica nanospheres with a 170 nm diameter (Bangs Laboratories SS02000) are diluted in water. The concentration is controlled so that approximately two nanospheres are contained per water droplet produced by a nebulizer that is used for the delivery of the nanoparticles to the trapping position. According to the specifications of the nebulizer (Mabis Minibreeze Ultrasonic Nebulizer) that is used, the water microdroplets formed by the nebulizer have approximately 5 $\mu$m diameter in size. If the water droplet introduced to the trapping site contains two nanospheres, a dumbbell-shaped nanoparticle is mechanically formed and is optically trapped as the water droplet evaporates. This method is simpler and less time consuming than the chemical synthesis, but has the drawbacks of trapping not dumbbells but singlets, triplets, or even larger particles. Therefore, the particles that are trapped need to be examined whether it is a dumbbell-shaped nanoparticle geometry but not a different shape.

As aforementioned, the dumbbell-shaped nanoparticles that were synthesized in either way is diluted in a solution form, and is delivered to the trapping site with a nebulizer at atmospheric pressures [25,41]. In previous studies, there has been various ways to deliver micro- or nanoparticles to the trapping site including using piezos or pulsed lasers to release the particles that are initially attached onto a substrate [24,71]. However, these methods have a low probability in being transported to the trapping site, and for nanoparticles the attractive van der Waals force from the surface have become too large to overcome. Instead of methods that need to release particles from a surface, our experiments use a nebulizer to launch the particles directly in forms of a solution. Before being nebulized, the dumbbell-shaped nanoparticles are sonicated for 10 minutes so that the particle aggregations are broken and evenly dispersed. Then the solution is loaded to a nebulizer with a tube to guide the nanoparticles to the trapping site. Once the particle falls down due to gravity and is trapped at the trapping position, the tube is removed and the vacuum chamber is sealed. The trapping process is observed with the 532 nm laser that is directed to the trapped nanoparticle and the scattering off the trapped particle is monitored with the camera outside the vacuum chamber as shown in Fig. 3.8. After the nanoparticle is trapped, the air pressure in the vacuum chamber is lowered to 0.01 torr before measurements to remove any excess nanoparticles in the chamber that may fall into the optical trap.

## 3.3 Dumbbell-shaped Nanoparticle Verification

Using either synthesis method from the above, the particle that is loaded to the optical trap may be a geometry that is not a dumbbell but a single sphere or a cluster of multiple particles. However, for our system to have an analogy to a torsion balance, it is important to confirm that the trapped particle is a dumbbell-shaped nanoparticle but not a different geometry. In order to verify the geometry of the nanoparticle, the ratio between the damping coefficients for translation motions in the three orthogonal axes is measured while the particle is trapped in the trapping
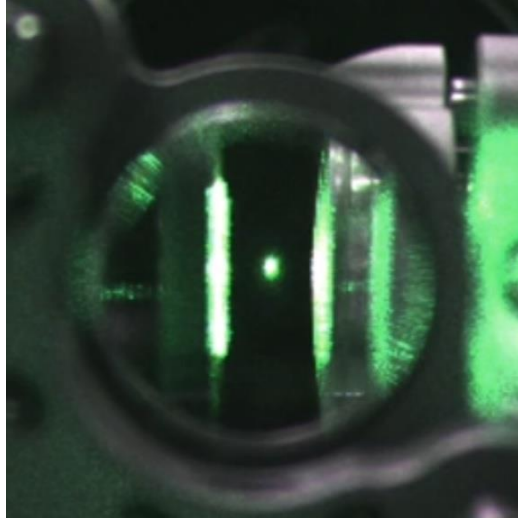
Fig. 3.8. Photograph of trapped nanoparticle. Scattering of 532 nm laser from particle is collected with a camera outside the vacuum chamber.

laser that is linearly polarized. If the trapped particle were to be a dumbbell-shaped nanoparticle, the particle's longer axis would align to the direction of laser polarization since the polarizability along the particle's longer axis is greater than that in the direction perpendicular to the longer axis. Since the dumbbell-shaped nanoparticle aligns in respect to the laser polarization, the damping rates along the different axes would have anisotropic values.

### 3.3.1 Direct Simulation Monte Carlo

A particle that is in the optical trap will experience a damping force due to the surrounding air molecules from the environment. Considering the different geometry the silica nanospheres that are trapped can form, the damping ratios are calculated using the Direct Simulation Monte Carlo (DSMC). In the calculations, the particle is assumed to be in the free molecular flow regime [149–151].

To begin with, gas molecules are launched from an imaginary sphere that is surrounding the particle of interest. The trajectory of the gas molecule is simulated

until the molecule escapes the launching sphere and the momentum transfer along the trajectory is used to determine the damping force the trapped particle experiences. For accurate simulations, the following is considered: the trajectory of the gas molecules with stochastic directions and speeds, collision and re-emitted molecule's velocity, and the estimation of damping force.

The damping force can be calculated with the net momentum transmitted from the gas molecules to the trapped nanoparticle. The following equation is for damping force when the particle is moving along the x:

$$F_D^x = \begin{bmatrix} F_{Dx}^x \\ F_{Dy}^x \\ F_{Dz}^x \end{bmatrix} = \frac{\mu a^2}{\lambda} \frac{\sqrt{\pi} A_e^*}{N_m} \sum_{i=1}^{N_c} \sigma_{inc,i}(c_{inc,i}^* - c_{ref,i}^*) \tag{3.1}$$

Here, $\mu$ corresponds to the gas viscosity coefficient, a is the radius of one nanosphere, $\lambda$ is the mean free path of the gas molecules, $A_e^*$ is the surface area of the launching sphere, $N_m$ is the total number of the launched gas molecules, $N_c$ is the number of gas molecules that have collision with the trapped particle, $\sigma_{inc,i}$ is the flux of the gas molecules, $c_{inc,i}^*$ is the momentum of the launched gas molecule, and $c_{ref,i}^*$ represents the momentum of the re-emitted gas molecule as it reaches back to the launching sphere. Similarly, the values for $F_D^y$ and $F_D^z$ can also be calculated, and with the damping force tensor, the damping force coefficients along the three axes can be derived.

The results for a dumbbell-shaped nanoparticle is calculated for two cases: when two spheres are touching leading to an aspect ratio (L/D) of 2 and when two spheres have an interpenetration allowing the aspect ratio (L/D) to be 1.9. For the former case, the ratio of the damping coefficient along the short axes to the long axis becomes 1.258. For the latter case, the ratio is 1.276. Since a dumbbell would have two short axes with same damping, the damping rate ratio along the short axis to the long axis are the same for the two different directions. As depicted in Fig. 3.9, the damping rate ratio values for different various geometries are 1.378 for chain trimers, 1.133-1.136 for triangle trimers, and 1.448 for chain tetramers. These values are distinct from the
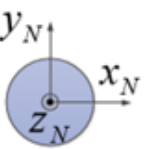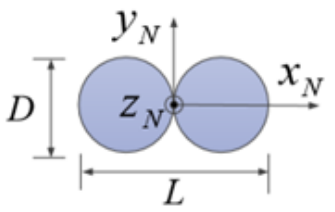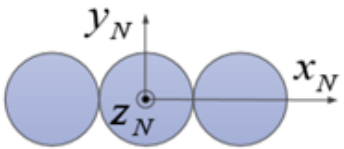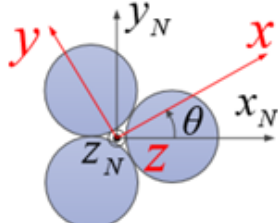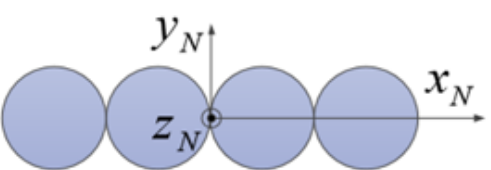
| Particle type | | | $\Gamma_y/\Gamma_x$ | $\Gamma_z/\Gamma_x$ |
|---|---|---|---|---|
| Sphere |  | | 1 | 1 |
| Dumbbell |  | $L/D = 1.9$ | 1.276 | 1.276 |
| | | $L/D = 2.0$ | 1.258 | 1.258 |
| Chain trimer |  | | 1.378 | 1.378 |
| Triangle trimer |  | | 0.997-1.004 | 1.133-1.136 |
| Chain tetramer |  | | 1.448 | 1.448 |

Fig. 3.9. Calculated damping rate ratios for nanoparticles with various geometries.

value for a dumbbell-shaped nanoparticle, and therefore the damping rate ratio can be used to confirm the trapped particle is a dumbbell-shaped nanoparticle.

The damping rate ratio for dumbbells with different aspect ratio can be calculated with DSMC. In Fig. 3.10, the ratio of the damping coefficients in the $y_N$ direction ($\Gamma_y$)
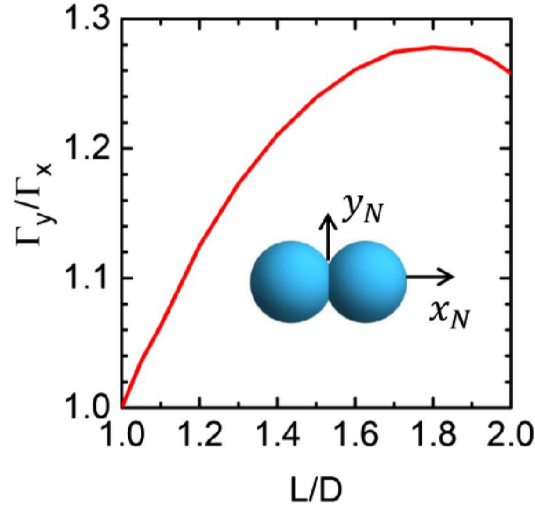
Fig. 3.10. Damping ratio for the translational directions in respect to the dumbbell-shaped nanoparticle versus the aspect ratio. The two translational directions are shown in the inset figure.

and along the $z_N$ direction ($\Gamma_x$) is plotted in regard to the aspect ratio (L/D). The inset shows each direction in respect to the dumbbell-shaped nanoparticle orientation. It can be verified for a dumbbell with a aspect ratio of 1, which is a sphere, the damping ratio is 1.

### 3.3.2   Power Spectral Density

To experimentally measure the damping coefficients, the power spectral density (PSD) of the translational motions along the three orthogonal axes are measured. Since the trapping laser is linearly polarized and the polarization is along the X, the trapped object tries to align its longer axis so that it is parallel with the X axis. As discussed earlier, the orientation of the trapped dumbbell-shaped nanoparticle is fixed in the linearly polarized trapping laser and the damping ratio is measured with the PSD.

Optically trapped nanoparticles are considered as particles in a harmonic potential assuming the particle undergoes small displacements. In this circumstance, the one dimensional equation of motion in $j = x, y, z$, can be expressed as follows.

$$\frac{d^2 j(t)}{dt^2} + \Gamma_0 \frac{dj(t)}{dt} + \Omega^2 j(t) = F_{th}(t)/M \tag{3.2}$$

Here $\Gamma_0$ stands for the damping coefficient, $\Omega$ is the trapping frequency, $F_{th}(t)$ is a random Langevin force, and $M$ corresponds to the mass of the trapped object. Based on the fluctuation-dissipation theorem, $< F_{th}(t)F_{th}(t - t') > = 2M\Gamma_0 k_B T\delta(t')$ when $k_B$ is the Boltzmann constant and $T$ is the temperature. From here, the PSD can be found which is the squared modulus of the Fourier transform of a variable [152, 153].

The Fourier transform of Eq. 3.2 results in:

$$(-\omega^2 + i\omega\Gamma_0 + \Omega^2)j(\omega) = F_{th}(\omega)/M \tag{3.3}$$

The $j(\omega)$ and $F_{th}(\omega)$ are the Fourier transform of $j(t)$ and $F_{th}(t)$ defined as:

$$j(\omega) = \int_{-\infty}^{\infty} e^{i\omega t} j(t)dt \tag{3.4}$$

$$F_{th}(\omega) = \int_{-\infty}^{\infty} e^{i\omega t} F_{th}(t)dt \tag{3.5}$$

From Eq. 3.3, $j(\omega)$ is found.

$$j(\omega) = \frac{F_{th}(\omega)}{M(\Omega^2 - \omega^2 + i\omega\Gamma_0)} \tag{3.6}$$

By the Wiener-Khinchin theorem, the PSD for $j$ can be found as

$$S_j(\omega) = \int_{-\infty}^{\infty} < j(t)j(t - t') > e^{-i\omega t'}dt' = \frac{2M\Gamma_0 k_B T}{M^2[(\Omega^2 - \omega^2)^2 + \omega^2\Gamma_0^2]} \tag{3.7}$$

Therefore the expected value of PSD for the COM motion along the three axes can be given as the following [152]:

$$S_j(\omega) = \frac{2k_B T}{M} \frac{\Gamma_0}{(\Omega_j^2 - \omega^2)^2 + \omega^2\Gamma_0^2} \tag{3.8}$$

The measured PSD for the three translational motions are depicted in Fig. 3.11 (b) and the black curve is the Lorentz fit. The linewidth $\Gamma_0$ is found from the fitting

along the three axes. From the fitting with the measured PSD for a silica dumbbell-shaped nanoparticle of 170 nm diameter, the measured damping ratio were $\Gamma_y/\Gamma_x = 1.25 \pm 0.01$ and $\Gamma_z/\Gamma_x = 1.27 \pm 0.02$. The values agree well with the simulation results in the previous section confirming that the trapped particle is a dumbbell-shaped nanoparticle.

Fig 3.11(a) shows the PSD for both the translational motion and torsional motion of the levitated dumbbell-shaped nanoparticle at $5 \times 10^{-4}$ torr. As the torsional motion frequency is higher compared to the translational motion, the ground state cooling of the torsional vibration can be considered promising.

## 3.4 Torque Sensitivity

With DSMC simulations, the drag torque acting on the dumbbell-shaped nanoparticle could also be calculated and plotted in regard to the aspect ratio (L/D) in respect
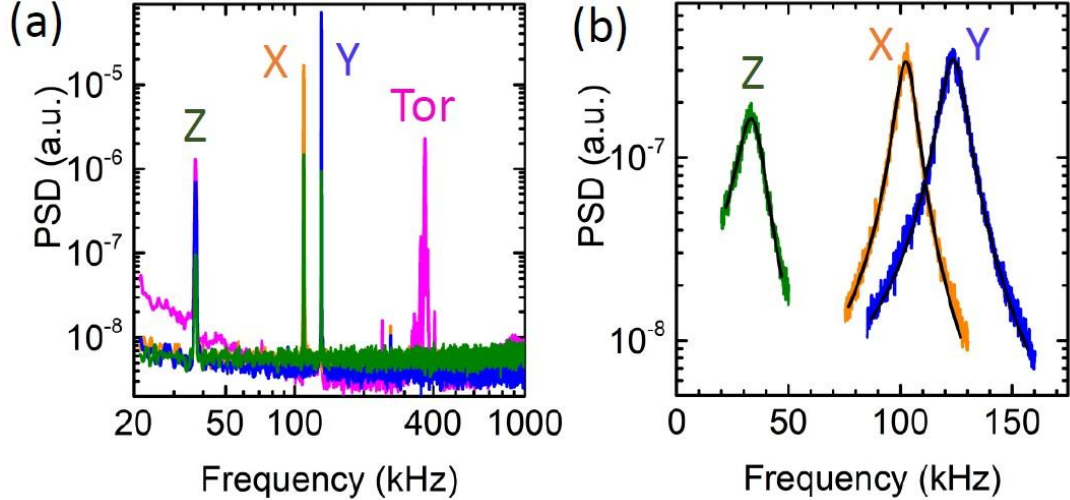


Fig. 3.11. (a) Measured PSD from torsional vibration and translation motion of a 170 nm, dumbbell-shaped nanoparticle trapped at $5 \times 10^{-4}$ torr. (b) Measured PSD from translational motions of a dumbbell-shaped nanoparticle at 10 torr.

to the damping torque a sphere would experience. The drag torque a sphere would experience is

$$T_{sphere} = \frac{\pi \mu D^4 \Omega}{(11.976 \lambda_M)} \tag{3.9}$$

where D is the sphere diameter, $\Omega$ is the rotation frequency, and $\lambda_M$ is the mean free path of the air molecules [151]. The drag torque for a dumbbell-shaped nanoparticle rotating around the Z axis, $T_z$, can be found:

$$T_D^z = \begin{bmatrix} T_{Dx}^z \\ T_{Dy}^z \\ T_{Dz}^z \end{bmatrix} = \frac{\mu a^4}{\lambda} \frac{A_e^*}{N_m} \sum_{i=1}^{N_c} \sigma_{inc,i}((r_{inc,i}^* \times c_{inc,i}^*) - (r_{ref,i}^* \times c_{ref,i}^*)) \tag{3.10}$$

Here, $r_{inc,i}^*$ and $r_{ref,i}^*$ corresponds to the position of where the gas molecules collide with the target particle. The $T_z = T_{Dz}^z$ is the drag torque of interest. The calculated drag torque acting on a dumbbell compared to that on a sphere is shown in Fig. 3.12(a) showing that the drag torque on a dumbbell is larger for larger aspect ratio and matches the value for a sphere when the aspect ratio is 1. The inset shows the axis the dumbbell-shaped nanoparticle is rotating around. Furthermore, the rotational damping rate about the Z axis is $\Gamma_\theta = T_z/(I_z\Omega)$ and $I_z$ is the moment of inertia.

Fig. 3.12(b) shows the different effective susceptibility along the $x_N$ and $y_N$ direction. Since the trapped particles are substantially smaller than the trapping laser wavelength, the dipole approximation is used. Accordingly, the induced dipole on the trapped dumbbell-shaped nanoparticle is expressed as the following:

$$\mathbf{p} = \alpha_x E_x \mathbf{x_N} + \alpha_y E_y \mathbf{y_N} + \alpha_z E_z \mathbf{z_N} \tag{3.11}$$

Here $\mathbf{x_N}$ is the direction of the longer axis of the dumbbell while $\mathbf{y_N}$ and $\mathbf{z_N}$ are the directions perpendicular to the longer axis of the dumbbell. With the complex amplitude of the induced dipole, the force and the torque acting on the object can be described as $F_j = \frac{1}{2}Re\{\mathbf{p}^* \cdot \sigma_j \mathbf{E}\}$ and $M_j = \frac{1}{2}Re\{\mathbf{p}^* \times \mathbf{E}\}$ [131]. The quasistatic polarizability $\alpha_j^0$ is related to the effective susceptibility as $\chi_x = \alpha_x^0/(\epsilon_0 V)$ and $\chi_y = \alpha_y^0/(\epsilon_0 V)$ [154] where $\epsilon_0$ is the vacuum permittivity and V is the volume of the dumbbell-shaped nanoparticle. When L/D = 1.9, $(\chi_x - \chi_y)/\chi_y = 0.14$. The
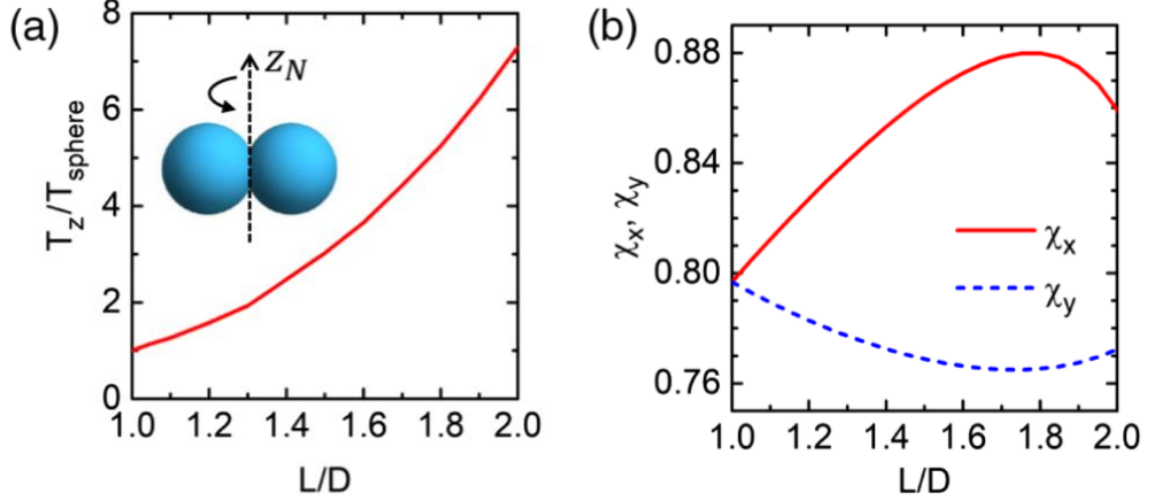
Fig. 3.12. (a) Calculated drag torque of a levitated dumbbell-shaped nanoparticle in respect to drag torque of sphere versus aspect ratio. (b) Calculated effective susceptibilities of dumbbell-shaped silica nanoparticles in $x_N$ and $y_N$ directions.

effects from the oscillation of the laser electric field can be included and then the polarizability becomes [155, 156]:

$$\alpha_j = \frac{\alpha_j^0}{1 - [ik_0^3 \alpha_j^0/(6\pi\epsilon_0)]} \tag{3.12}$$

Here $k_0$ is the wavenumber. The real part of the polarizability can explain the confinement of the orientation of the dumbbell-shaped nanoparticle while the imaginary part would be relevant to the rotation of the nanoparticle.

Calculations on the drag torque acting on a rotating dumbbell-shaped nanoparticle and the effective susceptibility along the different axes of the dumbbell-shaped nanoparticle are important to derive the torque sensitivity the dumbbell-shaped nanoparticle would have as a levitated Cavendish torsion balance. The torque sensitivity for the system is shown in respect to the air pressure in Fig. 3.13. The smallest torque that can be detected restricted by the thermal noise is [157]:

$$M_{th} = \sqrt{\frac{4k_B T_{env} I_z \Gamma_\theta}{\Delta t}} \tag{3.13}$$
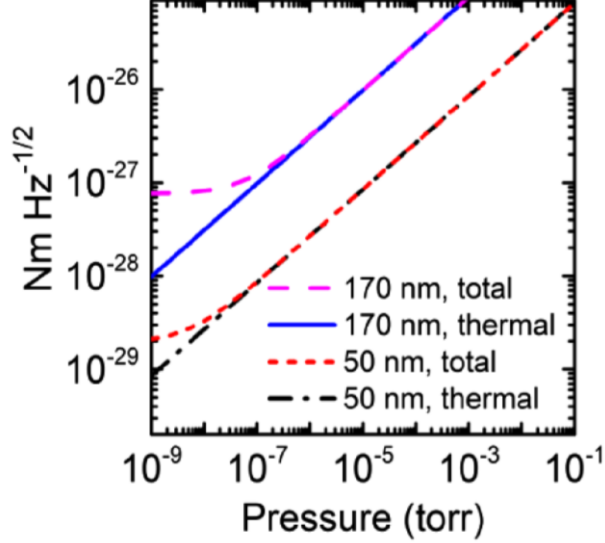
Fig. 3.13. Torque sensitivity calculated for optically levitated dumbbell-shaped silica nanoparticles with 170 nm and 50 nm diameter.

where $T_{env}$ is the environment temperature, $\Gamma_\theta$ is the rotational damping rate of the dumbbell-shaped nanoparticle, and $\Delta t$ is the time duration of measurement. The drag torque $T_z$ is pressure dependent and therefore the minimum torque the dumbbell will be able to sense is limited by the thermal noise until it reaches an ultrahigh vacuum where it is bounded by the laser shot noise. In this regime, the minimum measurable torque that is shot noise limited is [77]

$$M_{rad} = (\chi_x - \chi_y)k_0^2 V \hbar \sqrt{\frac{J_p}{(3\pi\Delta t)}} \qquad (3.14)$$

where $J_p = I_L/(\hbar\omega_L)$ corresponds to the photon flux, $I_L$ is the intensity and $\omega_L$ stands for the angular frequency of the laser. According to the calculations, with a 500 mW laser and at pressures below $10^{-8}$ torr, an optically trapped 170 nm diameter dumbbell-shaped nanoparticle would reach a torque detection sensitivity of $10^{-27} \mathrm{Nm}/\sqrt{\mathrm{Hz}}$ while a dumbbell-shaped nanoparticle with 50 nm diameter at the same conditions would reach $10^{-29} \mathrm{Nm}/\sqrt{\mathrm{Hz}}$. This torque sensor would be more sensitive by several orders compared to most advanced devices which have achieved

$10^{-22}$Nm/$\sqrt{\text{Hz}}$ at room temperature and $10^{-24}$Nm/$\sqrt{\text{Hz}}$ at temperatures of 25 mK [140].

## 3.5   GHz Rotation of dumbbell-shaped nanoparticles

Once the trapping laser polarization is adjusted from linear to circularly polarized light, the dumbbell-shaped nanoparticle could be driven into a mechanical rotation. Since the dumbbell-shaped nanoparticles have a non-spherical geometry, its susceptibility is anisotropic. The spin angular momentum of the circularly polarized beam is transmitted to the trapped dumbbell-shaped nanoparticles driving the particle into rotation, and the maximum rotation rate is reached once the optical and the drag torque on the rotating particle is equal. Since the drag depends on the air pressure, the drag torque acting on the dumbbell-shaped nanoparticle is small at vacuum, and the particles could be driven to rotation rates exceeding 1 GHz. Fig. 3.14(a) shows the PSD of the rotational motion of a 170 nm diameter dumbbell-shaped nanoparticle at $7.9 \times 10^{-5}$ torr. A peak is observed at about 2.2 GHz and this would correspond to a rotation of approximately 1.1 GHz since the dumbbell-shaped nanoparticle has a symmetric geometry and a signal would be detected twice for each revolution. This rotation of 1.1 GHz is two orders faster compared to the fastest of the rotations detected in previous studies [68, 70, 72] and our particle showed a high stability at this rotation rate.

The rotation is plotted versus the air pressure in Fig. 3.14(b). Since the rotation rate is decided by the optical torque $M_z$ and drag $T_z$ acting on the dumbbell-shaped nanoparticle and since the drag is proportional to air pressure, the rotation speed at steady state would be inversely proportional to pressure $p_{air}$ which could be observed in the results. The black line in Fig. 3.14(b) shows that the experimental measurements follows $A/p_{air}$ where $A$ is the fitting parameter. Higher rotation could have been observed at lower pressures. However, the detected rotation rate is constrained by the bandwidth of the photodetector used in experiment. The signal above 1.1 GHz

could not be detected due to the larger noise level compared to that of the signal from the rotating dumbbell-shaped nanoparticle.
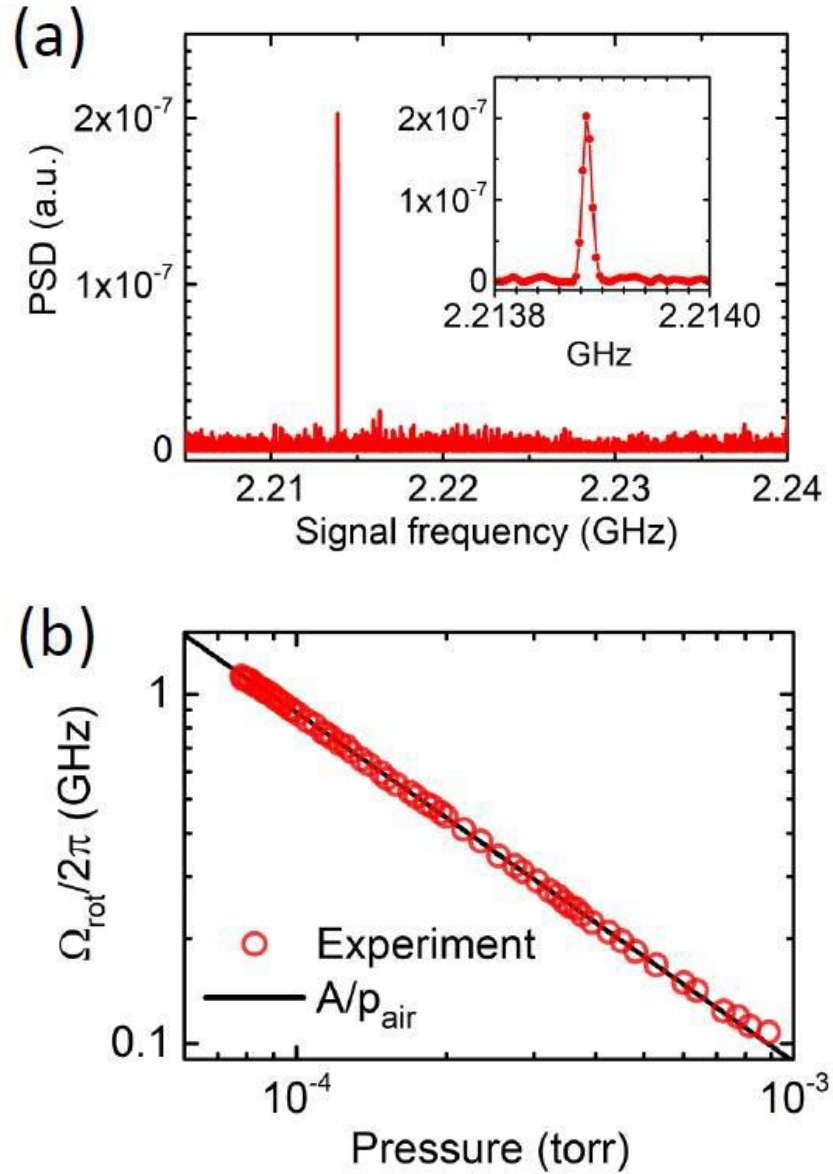


Fig. 3.14. (a) An example of a PSD experimentally measured from the rotational motion of a dumbbell-shaped nanoparticle showing signal at about 2.2 GHz. (b) Rotation frequency of a dumbbell-shaped silica nanoparticle versus pressure.

### 3.5.1 Terminal Rotation Frequency

The dumbbell-shaped nanoparticle rotating at such a fast rotation speed would also experience a large centrifugal force. Once the centrifugal force reaches the ultimate tensile strength (UTS), the particle would break and the particle would no longer be able to reach higher rotation speeds. This would determine the terminal rotation frequency a silica dumbbell-shaped nanoparticle will be able to reach. Therefore, with the terminal rotation frequency, the UTS of nanoparticles can be studied.
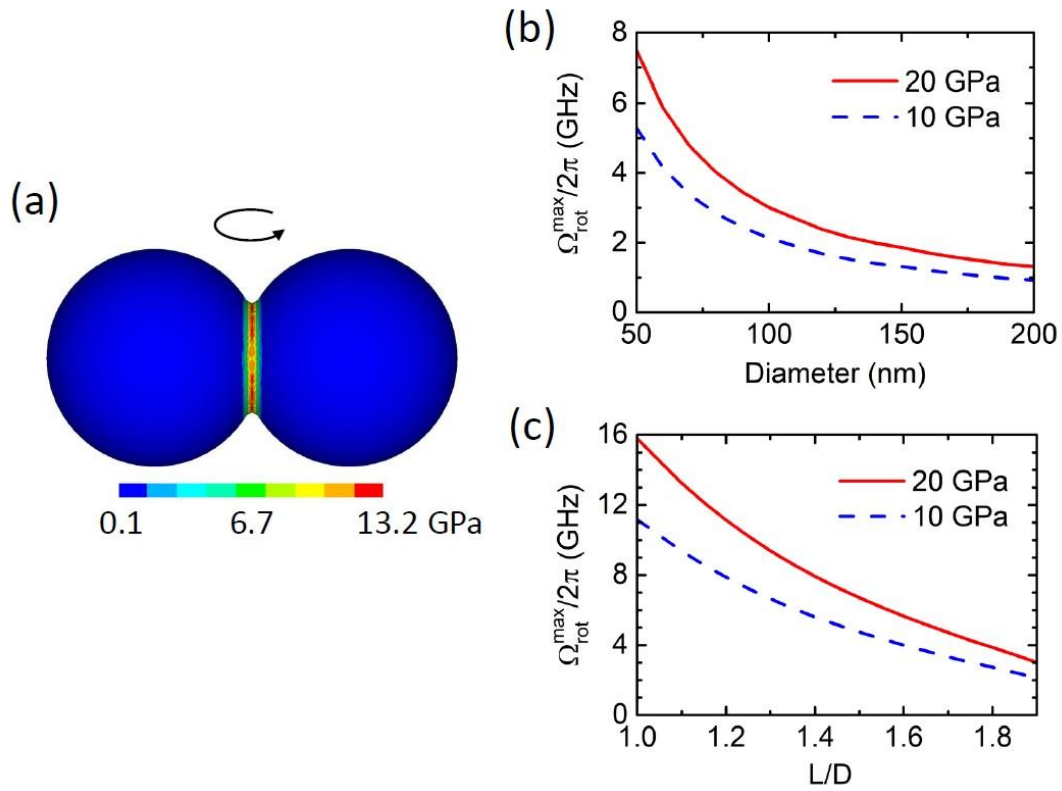


Fig. 3.15. (a) Calculated stress distribution of a dumbbell-shaped nanoparticle with 170 nm diameter and aspect ratio of 1.9 rotating at 1.2 GHz (b) Terminal rotation frequency versus size of dumbbell-shaped nanoparticle. The aspect ratio is fixed at 1.9. (c) Terminal rotation frequency versus aspect ratio. The diameter of the dumbbell-shaped nanoparticle is fixed at 100 nm.

First, the stress distribution on a 170 nm diameter silica dumbbell-shaped nanoparticle with an aspect ratio of 1.9 rotating at a rate of 1.2 GHz is calculated with the finite element method and is shown in Fig. 3.15(a). Assuming the curvature radius at the point where two spheres are in contact is 5 nm, the utmost stress the dumbbell-shaped nanoparticle would experience is approximately 13 GPa. This is two orders higher compared to UTS of a bulk glass and proves that the dumbbell-shaped silica nanoparticle is comparably strong to silica nanowires [158].

The terminal rotation frequency a dumbbell-shaped nanoparticle could attain is plotted as in regard to particle size and aspect ratio in Fig. 3.15(b) and Fig. 3.15(c), respectively. The UTS is set to be in the range of 10 to 20 GPa based on the calculations from the finite element method shown in the above. In Fig. 3.15(b), the aspect ratio is fixed at 1.9 and from the calculations, a dumbbell-shaped nanoparticle with a diameter of 170 nm would have an terminal rotation frequency of 1.1 to 1.6 GHz. The ultimate rotation speed becomes faster as the particle size decreases. In Fig. 3.15(c), the diameter of one sphere composing the dumbbell is fixed to 100 nm and the maximum rotation is shown as a function of aspect ratio. As the aspect ratio becomes smaller, the particle can withstand a larger rotation speed before it breaks due to the large centrifugal forces. Therefore, with smaller dumbbell-shaped nanoparticles that have smaller aspect ratios, and with more advanced instruments that have a higher bandwidth, the observation of a mechanical rotation exceeding 10 GHz can be anticipated in future studies.

# 4. ULTRASENSITIVE TORQUE DETECTION WITH OPTICALLY LEVITATED NANOPARTICLES

## 4.1 Introduction

Among the various mechanical instruments that have been used for the measurements on fundamental interactions, torque sensors have played a major role in many important discoveries in modern physics [7, 138, 159]. For example, the torsional balance was used by Henri Cavendish for the earliest determination on the gravitational constant and it was also used for the discovery of the Coulomb's law. More recently, with the technological advances such as nanofabrication, the torque sensors have drawn interest for its capability to study multiple ambitious subjects including small-scale magnetism and the Casimir effect [160–163]. Along the aforementioned research topics, there have been continuous efforts to develop a torque detecting system with improved sensitivities [140].

Levitated optomechanics possesses a strong advantage in precision measurements and sensing with its great isolation from the surrounding thermal bath [38, 44, 49]. Recently, the field has begun to investigate beyond the conventional COM degrees of freedom with spherical particles, and has observed the rotation [68, 70, 72, 74, 75, 80], torsional vibration [41, 75] and precession [76] of non-spherical nanoparticles levitated in vacuum. Spontaneously, theoretical work have proposed the use of nonspherical particles optically levitated in vacuum as a highly sensitive torsion balance [75] that would provide an apparatus to study anisotropic surface interactions [77]. However, due to experimental challenges, an optically levitated torque sensor with state-of-the-art sensitivities has not been implemented previous to the work introduced in this chapter.

Prior to this work, the most advanced torque sensor has obtained a sensitivity of $2.9 \times 10^{-24} \text{Nm}/\sqrt{\text{Hz}}$ with a nanofabricated cavity-optomechanical torque sensor at cryogenic temperatures of 25 mK [140]. Furthermore, in our previous work presented in the previous chapter, a mechanical rotation of above 1 GHz has been reached with silica dumbbell-shaped nanoparticles optically levitated in a circularly polarized laser [75, 80]. The maximum rotation frequency observed from the fastest human made nanomechanical rotor was only limited by the bandwidth of the photodetector used in the experiments. In this work, an optically levitated nanorotor is employed as a torque sensor at room temperature and acquires an unprecedented sensitivity of $(4.2 \pm 1.2) \times 10^{-27} \text{Nm}/\sqrt{\text{Hz}}$. This system has the advantages that it does not involve cryogenic cooling or sophisticated nanofabrication. Furthermore, with improved measurement devices, observations on a nanoparticle driven to a rotation with a record speed of above 5 GHz is presented. The optically levitated nanorotor is expected to experimentally detect the vacuum friction which has been proposed in many theoretical studies [84, 86, 164, 165] and be applicable to research on nanoscale magnetism [160, 162] and the quantum geometric phase [166].

## 4.2   Experimental Apparatus

The experimental apparatus for the present research is similar to that of the system used in the former chapter. It employs the same optical levitation system in the custom-built vacuum chamber and uses the silica sample with the same particle loading process using the nebulizer. However, in order to add an external torque to the optically trapped particles, an additional laser is added and time successive spectrum is measured with the spectrum analyzer in order to measure the torque. Finally, an additional photodetector and a spectrum analyzer with larger bandwidth are used for measurements on higher frequencies compared to the previous chapter.
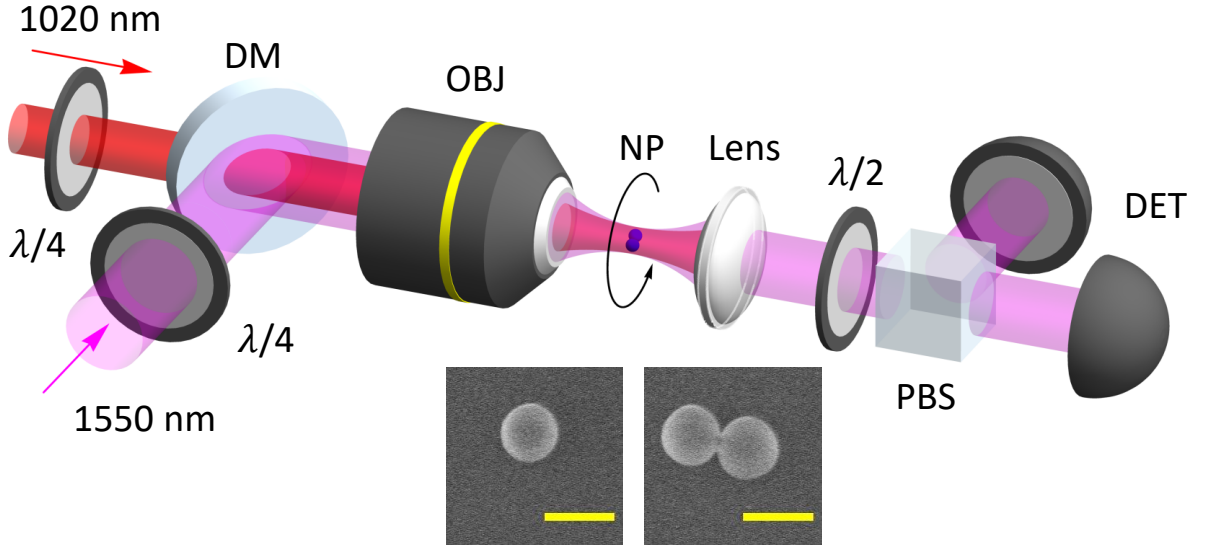
Fig. 4.1. Experimental schematic. A 1550 nm laser with a power of 500 mW is strongly focused using a (N.A. = 0.85) objective lens and is used to optically trap silica nanoparticles in air an vacuum. A 1020 nm laser is added to deliver the torque to be evaluated. The quarter waveplates are used to control the polarization of each laser. A collimation lens is placed after the focal position of the trap laser and the trap laser is employed to monitor the motions of the trapped nanoparticle. Only the detection scheme for torsional and rotational motion is shown for simplicity. A silica nanosphere sample and a dumbbell-shaped silica nanoparticle sample are shown in the SEM image below. The scale bar in both images are 200 nm.

## 4.2.1 External Torque Measurement

As in the previous chapter, a tightly focused 1550 nm laser in a vacuum chamber is used to optically trap silica nanoparticles (nanospheres or dumbbell-shaped nanoparticles) and its polarization is adjusted with a quarter waveplate prior to the objective lens. The detection on the particle is done with a similar setup of a collimation lens guiding the trapping beam to the balanced detectors which monitor the COM, rotational and torsional motions.
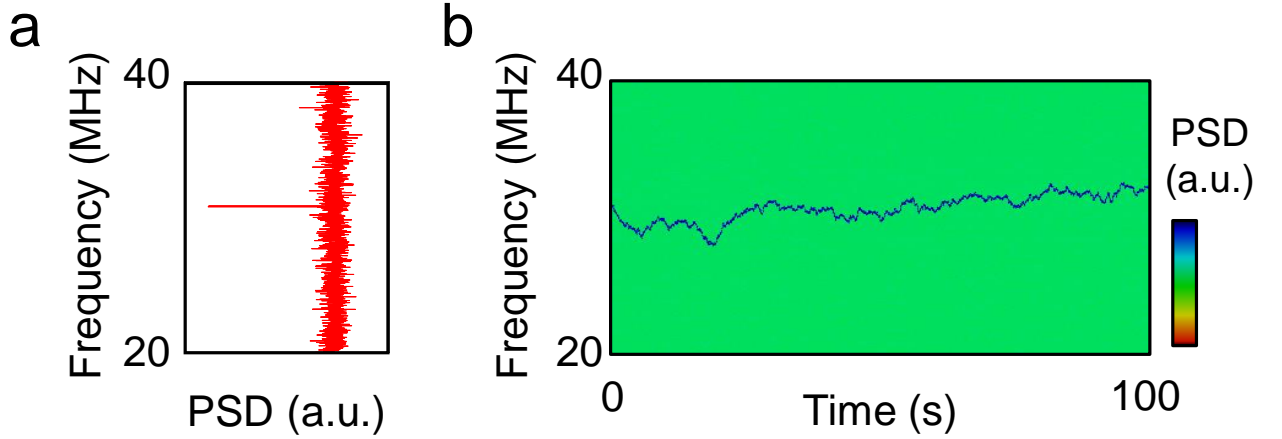
Fig. 4.2. (a) An example of a rotation PSD measured from a trapped nanoparticle at $10^{-4}$ torr. (b) An example of a spectrogram of the rotational motion taken for a measurement time of 100 seconds. The vertical line at the beginning of the spectrogram corresponds to the rotation PSD depicted in plot (a).

Before this study, when measuring the rotation frequency of the optically trapped nanoparticles, a simple spectrum was taken at a certain time and the rotation rates were determined from the spectrum as in Fig. 4.2 (a). In this study, for the measurements of small torque, the spectra are taken continuously for a certain amount of time duration and therefore the spectrogram function of the spectrum analyzer (Tektronix, RSA306) is used. The spectrogram displays a time trace of spectra by presenting the amplitude of each spectra with color. Each vertical line shown in Fig. 4.2 corresponds to a single spectrum and the frequency range can be shown in the y axis. In the x axis, the time is shown and the continuous vertical lines show the time trace of spectra taken for 100 seconds.

For the external torque, an additional 1020 nm laser (Q Photonics, L.L.C, QFBGLD-1030-400PM) is added. The circularly polarized 1020 nm laser applies an external

torque to the trapped nanoparticle and is modulated sinusoidally during the torque measurements. The sinusoidal signal is applied from a waveform generator (Agilent, 33500B) and this waveform generator is also used to send a reference signal to the voltage controlled oscillator (VCO).
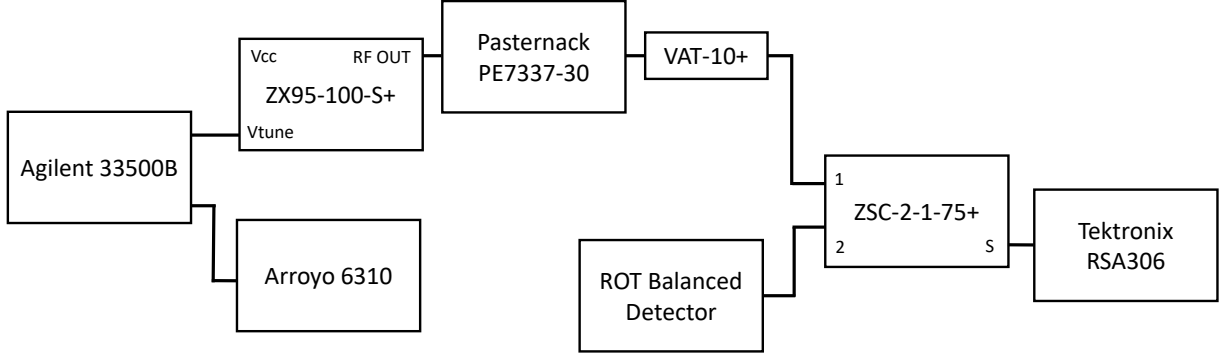


Fig. 4.3. Electronics for torque measurements. Signal from waveform generator is sent to VCO and laser diode controller. VCO generates a radio-frequency (RF) signal for a reference for measurements on torque. VCO signal is attenuated and added with rotation signal from the balanced photodetector and is observed with the spectrum analyzer.

Along with the additional laser for external torque, a VCO (Mini-Circuits, ZX95-100-S+) is added to generate a signal that serves as a reference during the torque measurements. A more elaborate description on the method used to measuring the torque will be provided in the following section, but for accurate measurements, it is important that the measurement times start at the same phase in respect to the sinusoidal signal generated by the signal generator. The VCO takes an input voltage and creates an oscillating output signal at a frequency depending on the input voltage. The voltage dependent frequency from the VCO allows the observation of the voltage sent to the 1020 nm laser controller using the spectrum analyzer. Therefore, the simultaneous observation of the 1020 nm laser power modulation and the change in

frequency of the rotational motion of the optically trapped nanoparticle is possible with our system.

The scheme in Fig. 4.3 is used for generation of the reference RF signal and not to exceed the maximum power that can be read with the spectrum analyzer. The waveform generator generates a signal that is connected to the laser diode controller (Arroyo Instruments, 6310) which controls the 1020 nm laser power. An additional signal with the same phase is generated and sent to the VCO where the voltage is converted to the frequency domain. Subsequently, the signal is attenuated and added with the signal from the rotation detector. Finally, the signal from the VCO and the rotation detector is read simultaneously from the spectrum analyzer. An example of the measurement screen is shown in Fig. 4.4.

### 4.2.2 Rotation Detection with Larger Bandwidth

The previous study measuring a maximum rotation of approximately 1.1 GHz was limited by the bandwidth of the photodetector that was used in the experiments. In this study, in order to overcome the shortcomings from the experimental apparatus, a balanced detector (Optilab, PR-40G-M) with a 32 GHz bandwidth and an additional spectrum analyzer (Agilent 9344C) with a 20 GHz frequency range is added to the system. The device allows the observations on improved rates of rotations in the experiments. The modified setup for rotation detection enables measurements of up to 10 GHz if the particles can withstand such a high rotation rate.

### 4.3 Torsional Vibration and Rotational Motion of Silica Nanoparticles

With the modified experimental system, the vibration and rotation of the optically trapped silica nanoparticles with different geometry are compared. Once a silica particle is confined in the linearly polarized optical trap, the pressure is lowered to 10 torr and the PSD of the motions of the particle is taken as shown in Fig. 4.5.
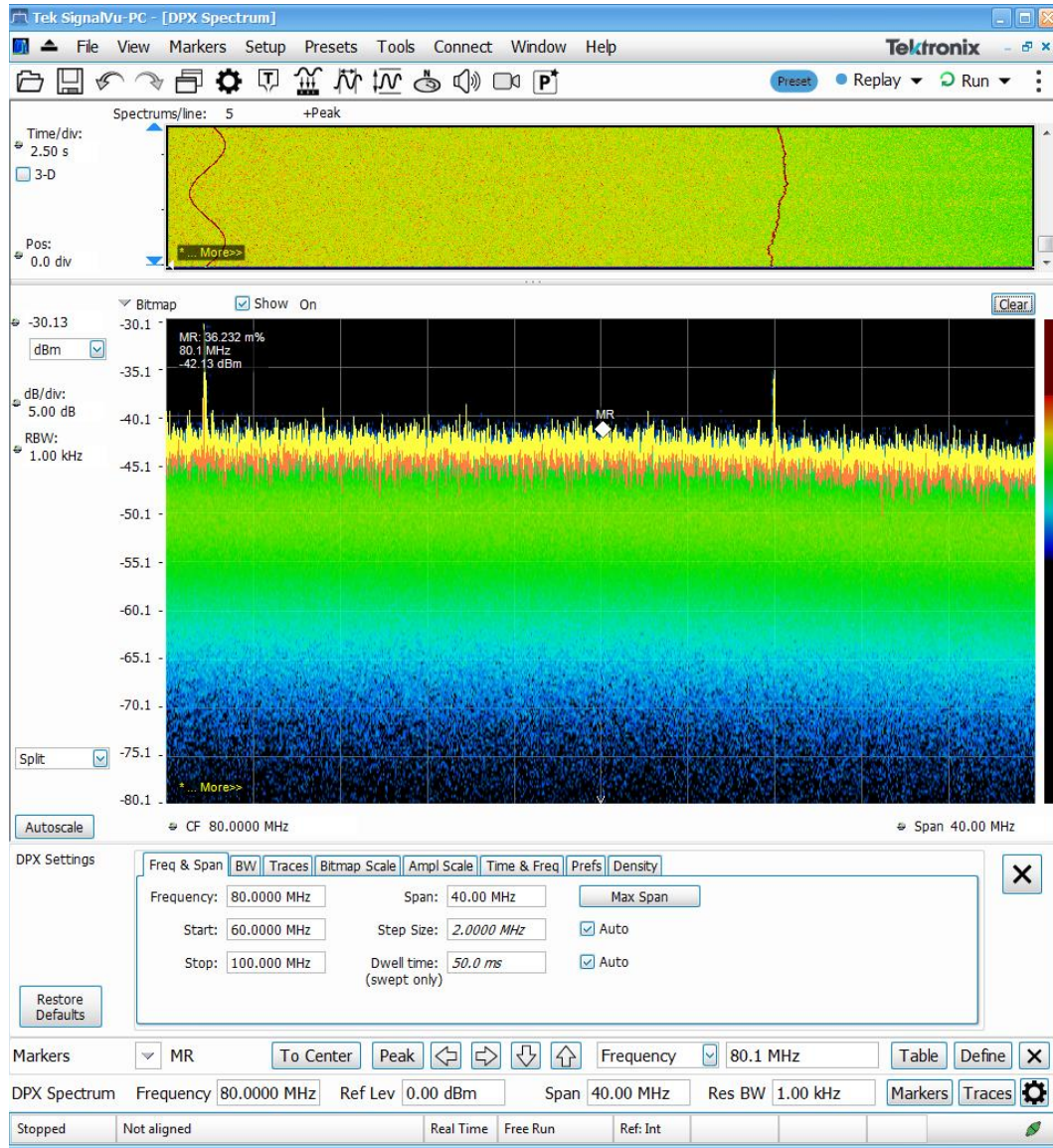
Fig. 4.4. Example of spectrogram measurement with VCO signal and the rotation detection signal. The signal on the left is from the VCO and the signal on the right is the detection signal from a rotating particle.

The PSD for a silica nanosphere and a silica dumbbell-shaped nanoparticle is compared in Fig. 4.5 (a) and (b). As in the earlier study, the polarization of the trap laser is parallel to the X axis, the propagation direction of the laser is along the Z axis and the damping in each translational direction is used to verify the shape
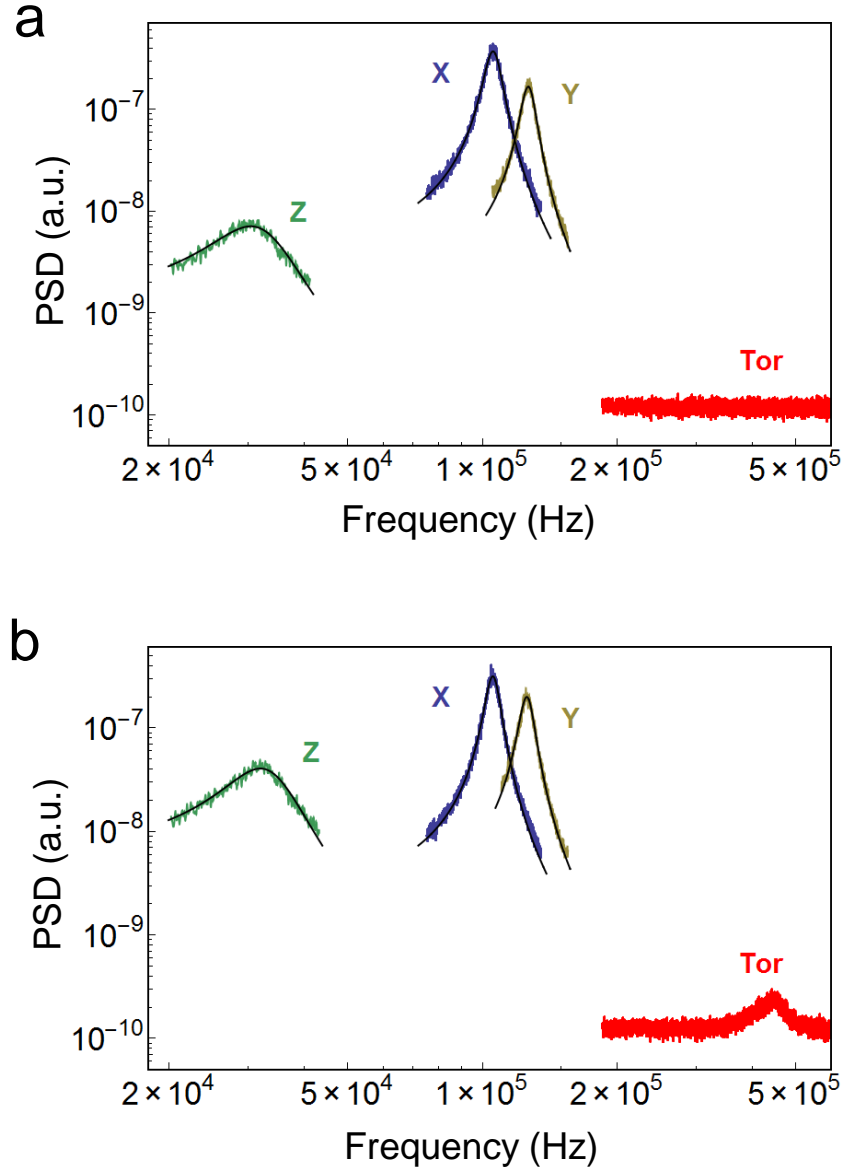
Fig. 4.5. PSD measurements on the translation and torsional motions of the optically trapped silica nanoparticles in a linearly polarized laser at pressure of 10 torr. (a) The measured PSD of a silica nanosphere. (b) The PSD measurement of a silica dumbbell-shaped nanoparticle. An additional peak that does not appear in the nanospheres appears in the torsional vibration for the case of the dumbbell-shaped nanoparticle. The black curves show the Lorentz fit for each translational direction.

of the particle that is trapped. For the nanosphere, the ratio of the damping along the Y to X directions is $1.02 \pm 0.01$ which is comparable to the anticipated value of 1. Also, a peak does not appear in the torsional vibration. In the contrary, for a dumbbell-shaped nanoparticle, the ratio of damping is $1.23 \pm 0.02$ and which is close to the anticipated value of 1.27 for a dumbbell geometry [75]. Additionally, a peak between 400 to 500 kHz can be observed in the PSD which corresponds to the torsional vibration motion. With the damping ratio perpendicular and parallel to the trap laser polarization and the appearance of the torsional peak, the geometry of the trapped silica particle could be determined between spheres and dumbbells.

Following the verification of the geometry of the silica particles, the trapping laser polarization is switched to a circular polarization and the trapped particle is driven into a rotation [75, 80]. As in the previous study, the angular momentum from the laser with circular polarization delivers an optical torque to the trapped nanoparticles, and the counterbalance between the drag from the surrounding gas and the optical torque determines the rotation speed of the trapped particles. Since the drag torque is linearly dependent on the air pressure, the rotation speed of the trapped particles is observed to be inversely proportional to pressure as shown in Fig. 4.6 and Fig. 4.7.

From Fig. 4.6, one can notice the rotation speed of a nanosphere substantially slower than that of a dumbbell-shaped nanoparticle while using an identical size, pressure, and the same optical trap. This is due to the smaller optical torque exerted on the nanosphere compared to that on a dumbbell-shaped nanoparticle caused by the differences in the geometry. The fastest rotation shown for the dumbbell-shaped nanoparticle in this plot already exceeds 3 GHz and this observation was possible by replacing the balanced detector and the spectrum analyzer with larger bandwidths.

Fig. 4.7 shows the results for the two fastest rotating nanoparticles observed throughout the experiments. The plot depicts the rotation frequency versus the pressure, and the data in red circles achieves measurement of rotation rates of approximately 5.2 GHz at $1.23 \times 10^{-5}$ torr while the particle shown in blue diamonds achieved rotation rates of about 5.0 GHz at $1.69 \times 10^{-5}$ torr. The inset also shown
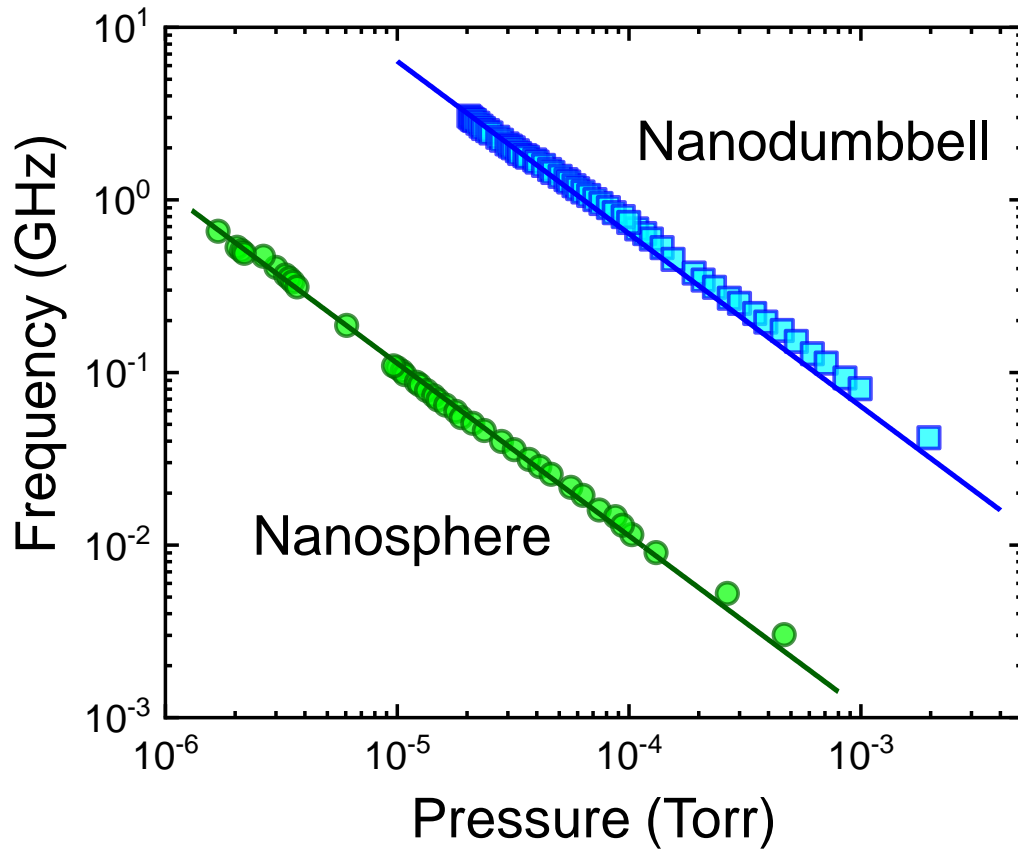
Fig. 4.6. The measured rotation frequency versus air pressure for nanospheres (green circles) and dumbbell-shaped nanoparticles (blue squares). The diameter for both particles is approximately 150 nm. The solid lines depict the rotation frequency inversely dependent to the air pressure.

in red and blue show the PSD of the rotational motions for the fastest rotation for each particle. From the geometrical symmetry, a peak appears at twice the rotational frequency, and therefore the peak in red is located at about 10.4 GHz while the peak in blue is at about 10.0 GHz. Shortly after reaching such rotational frequencies, the silica nanoparticles were lost from the optical trap showing that the maximum rotational frequency is now bounded by the particle loss instead of the bandwidth of the detectors. From the results, I was able to obtain mechanical rotation rates that
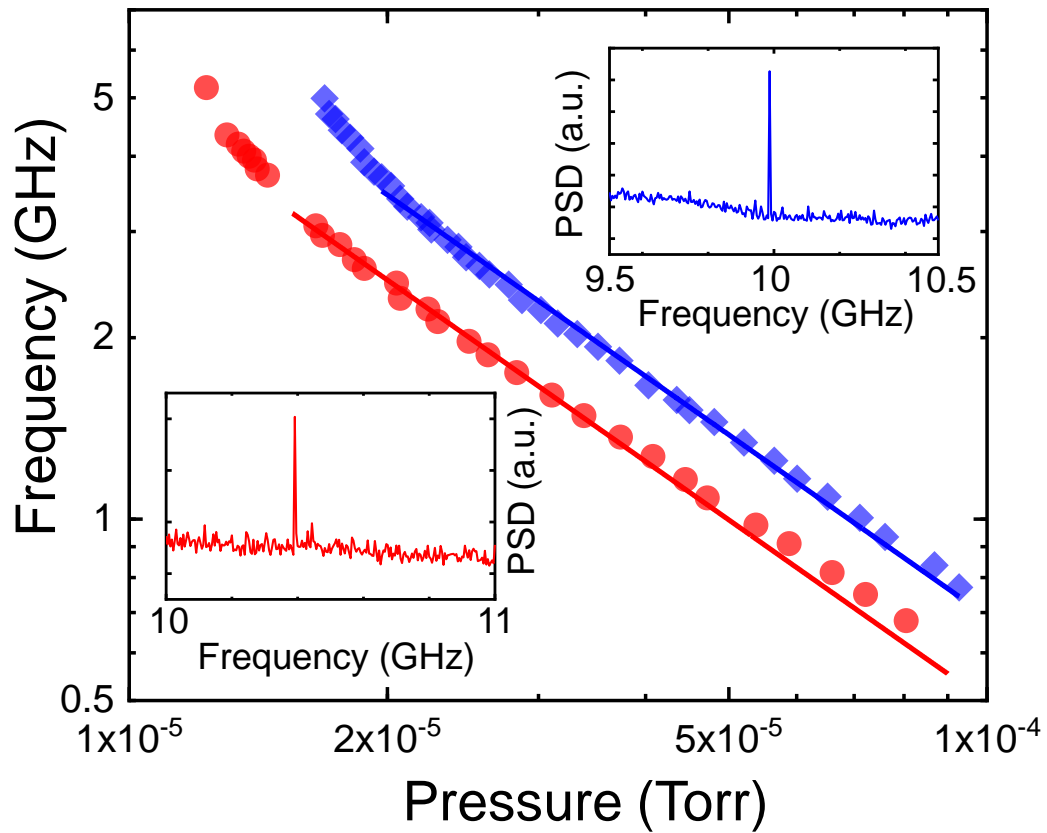
Fig. 4.7. The measured rotation frequency versus air pressure for the two fastest rotating silica particles. The insets show the measured PSD for the rotational motions of the two nanoparticles achieving 5.2 GHz and 5.0 GHz. The solid lines depict the rotation frequency inversely dependent to the air pressure.

surpass the previous fastest human-made nanomechanical rotor by approximately five times [75, 80].

## 4.4   Torque Measurement

In this study, the nanorotor is further exploited as an ultrasensitive torque sensor. For this purpose, as mentioned earlier, an additional circularly polarized 1020 nm laser

is added and is modulated sinusoidally in order to apply the external torque measured in the experiments. The corresponding equation of motion for the nanorotor can be shown as the following:

$$I_m \frac{d\omega_r(t)}{dt} + I_m \gamma \omega_r(t) = M_{th}(t) + M_{d.c.} + M_{a.c.} sin(\omega_{mod}t) \tag{4.1}$$

Here $I_m$ is the nanorotor's moment of inertia, $\omega_r$ is the nanoparticle's angular rotational velocity, $\gamma$ is the rotational damping rate that arises from the residual air molecules, $M_{th}$ is the thermal fluctuation torque, $M_{d.c.}$ is the constant part of the optical torque, $M_{a.c.}$ is an external torque from a sinusoidally modulated 1020 nm laser, and $\omega_{mod}$ represents the modulation frequency of the external torque. $M_{th}$ satisfies $< M_{th}(t)M_{th}(t - t') >= 2I_m \gamma k_B T \delta(t')$.

With the equation of motion, the PSD of the angular velocity that is time dependent can be calculated. The PSD is calculated with $(\omega_r - \omega_{d.c.})$ where $\omega_{d.c.} = M_{d.c.}/(I_m \gamma)$ is the average rotational frequency. First, exlcuding the effect from the alternating external torque, the Fourier transform of Eq. 4.1 results in:

$$(i\omega + \gamma)\omega_r(\omega) = M_{th}(\omega)/I_m \tag{4.2}$$

Again, the $\omega_r(\omega)$ and $M_{th}(\omega)$ are the Fourier transform of $\omega_r(t)$ and $M_{th}(t)$ defined as [152, 153]:

$$\omega_r(\omega) = \int_{-\infty}^{\infty} e^{i\omega t} \omega_r(t)dt \tag{4.3}$$

$$M_{th}(\omega) = \int_{-\infty}^{\infty} e^{i\omega t} M_{th}(t)dt \tag{4.4}$$

From Eq. 4.2, $\omega_r(\omega)$ can be arranged as the following:

$$\omega_r(\omega) = \frac{M_{th}(\omega)}{I_m(i\omega + \gamma)} \tag{4.5}$$

Here the angular frequency susceptibility $\chi(\omega)$ can be defined as $\omega_r(\omega) = \chi(\omega)M(\omega)$, and therefore [140]:

$$\chi(\omega) = \frac{1}{I_m(i\omega + \gamma)} \tag{4.6}$$

From the Wiener-Khinchin theorem, the PSD for $(\omega_r - \omega_{d.c.})$ can be found as:

$$S_r(\omega) = \int_{-\infty}^{\infty} <\omega_r(t)\omega_r(t-t')> e^{-i\omega t'}dt' = \frac{2\gamma k_B T}{I_m[\omega^2 + \gamma^2]} \tag{4.7}$$

To include the effect of the alternating torque in the PSD, the PSD of the sinusoidal external torque is calculated separately. Since in real experiments the measurements are carried out for a limited time, a truncated PSD is used and for a measurement time of $\Delta t$,

$$S_A(\omega) = \left| \frac{1}{\sqrt{\Delta t}} \int_{-\Delta t/2}^{\Delta t/2} A(t)e^{-i\omega t}dt \right|^2$$
$$= \frac{1}{\Delta t} \left| \frac{1}{2\pi} A(\omega) * \Delta t sinc(\frac{\Delta t\omega}{2}) \right|^2 \tag{4.8}$$

Inserting the sinusoidal torque in the position of $A(t)$ and $A(\omega)$, we find

$$S_A(\omega) = \frac{1}{\Delta t} \left| \frac{\Delta t}{2\pi} [\pi M_{a.c.}(\delta(\omega - \omega_{mod}) + \delta(\omega + \omega_{mod}))] * sinc(\frac{\Delta t\omega}{2}) \right|^2$$
$$= M_{a.c.}^2 \frac{\Delta t}{4} |sinc[\omega - \omega_{mod})\Delta t/2] + sinc[\omega + \omega_{mod})\Delta t/2]|^2 \tag{4.9}$$
$$\cong M_{a.c.}^2 \frac{\Delta t}{4} sinc^2[\omega - \omega_{mod})\Delta t/2]$$

Applying the angular displacement susceptibility $\chi(\omega)$ and using a single sided PSD, the PSD for $(\omega_r - \omega_{d.c.})$ including the driven external torque is finally found as

$$S_r(\omega) = \frac{4\gamma k_B T}{I_m[\omega^2 + \gamma^2]} + \frac{M_{a.c.}^2 \Delta t sinc^2[\omega - \omega_{mod})\Delta t/2]}{2I_m^2(\omega^2 + \gamma^2)} \tag{4.10}$$

Experimentally, the PSD $S_r(\omega)$ can be directly calculated with the rotational frequency $\omega_r/2\pi$ collected with the spectrum analyzer. This is advantageous compared to the cases with the COM motion since an additional calibration factor to convert the voltage signal to position [167] is not necessary for the torque measurements. An example of the $S_r(\omega)$ when the modulation amplitude of the 1020 nm laser is 20 mW and 0 mW is presented in Fig. 4.8 (b). The red dashed line corresponds to the case of 20 mW modulation and the blue solid line shows the results of no modulation. The 200 mHz peak originates from the modulated torque.

Ignoring the thermal noise $M_{th}$ the Eq. 4.1 can be solved as

$$\omega_r(t) = \omega_{d.c.} + \frac{M_{a.c.}}{\sqrt{I_m^2(\omega_{mod}^2 + \gamma^2)}} sin(\omega_{mod}t + \phi) \tag{4.11}$$
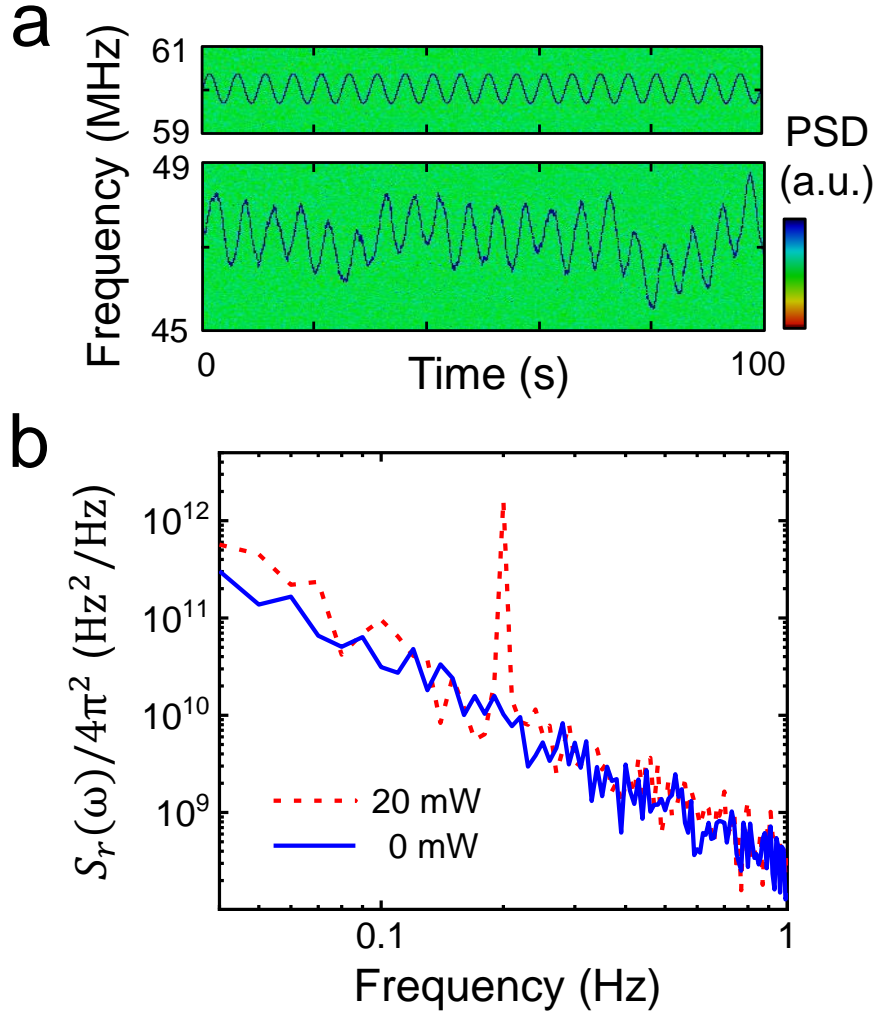
Fig. 4.8. (a) The measured spectrogram of the rotational frequency of a levitated nanoparticle under a sinusoidally modulated 1020 nm laser that delivers the external torque is shown in the bottom subfigure. The data is obtained at a pressure of $1.5 \times 10^{-5}$ torr and the laser modulation is at 200 mHz and with 39 mW amplitude. The top subfigure shows the RF signal generated from the VCO with the sinusoidally modulated voltage that controls the power of the 1020 nm laser. (b) PSD of the rotational motion spectrogram. The red dashed line shows result from 20 mW modulation and the blue solid line shows the case with no modulation. The 200 mHz peak appears due to the effect from the sinusoidally modulated external torque.

where $\phi = tan^{-1}(-\omega_{mod}/\gamma)$. This change in the rotational frequency of the nanorotor following the modulation of the external torque can be found in the lower subplot of Fig. 4.8 (a). Data were obtained at $1.5 \times 10^{-5}$ torr with 39 mW modulation amplitude and a 200 mHz modulation frequency. To compare the difference in the phase between the modulation of the laser and the change in the rotation frequency, the signal generated from the VCO with the identical modulation signal is presented on the top subplot of Fig. 4.8 (a). For the later torque measurements, this experiment was repeated with different modulation amplitudes.

The alternating torque can be measured using Eq. 4.11, but to do so the rotational damping rate $\gamma$ needs to be acquired first. This $\gamma$ can be measured by abruptly turning on the 1020 nm laser that provides the external torque and measuring the time dependent rotational frequency. The acquired data is fitted to an exponential curve $\omega = \omega_1 + (\omega_2 - \omega_1)(1 - e^{\frac{t-t_1}{\tau_r}})$ where $\omega_1$ represents the rotation frequency at the beginning, $\omega_2$ is the final rotation frequency, $t_1$ indicates when the external torque is switched on, and $\tau_r = 1/\gamma$ corresponds to the rotational damping time. The damping time, and therefore the damping rate, can be found from the fitting. Fig. 4.9 (a) shows an example of the measurement taken at $9.4 \times 10^{-6}$ torr. The external torque laser is switched on at 8 s, and the rotation frequency progresses following the exponential curve. The measurements are repeated multiple times at different pressures and the resulting damping time versus the air pressure is plotted in Fig. 4.9 (b). Results show a $1/p_{air}$ dependence on the air pressure, as expected.

With this experimentally measured rotational damping rate $\gamma$, the external torque $M_{a.c.}$ can be determined using the time dependent rotation frequency $\omega_r$. From Eq. 4.11,

$$(\omega_r - \omega_{d.c.})\sqrt{I_m^2(\omega_{mod}^2 + \gamma^2)} = M_{a.c.}sin(\omega_{mod}t + \phi) \tag{4.12}$$

If each side is multiplied with $sin(\omega_m t + \phi)$ and integrated over $\Delta t$,

$$\int_0^{\Delta t} (\omega_r - \omega_{d.c.})\sqrt{I_m^2(\omega_{mod}^2 + \gamma^2)}sin(\omega_{mod}t + \phi)dt = M_{a.c.}\frac{\Delta t}{2} \tag{4.13}$$
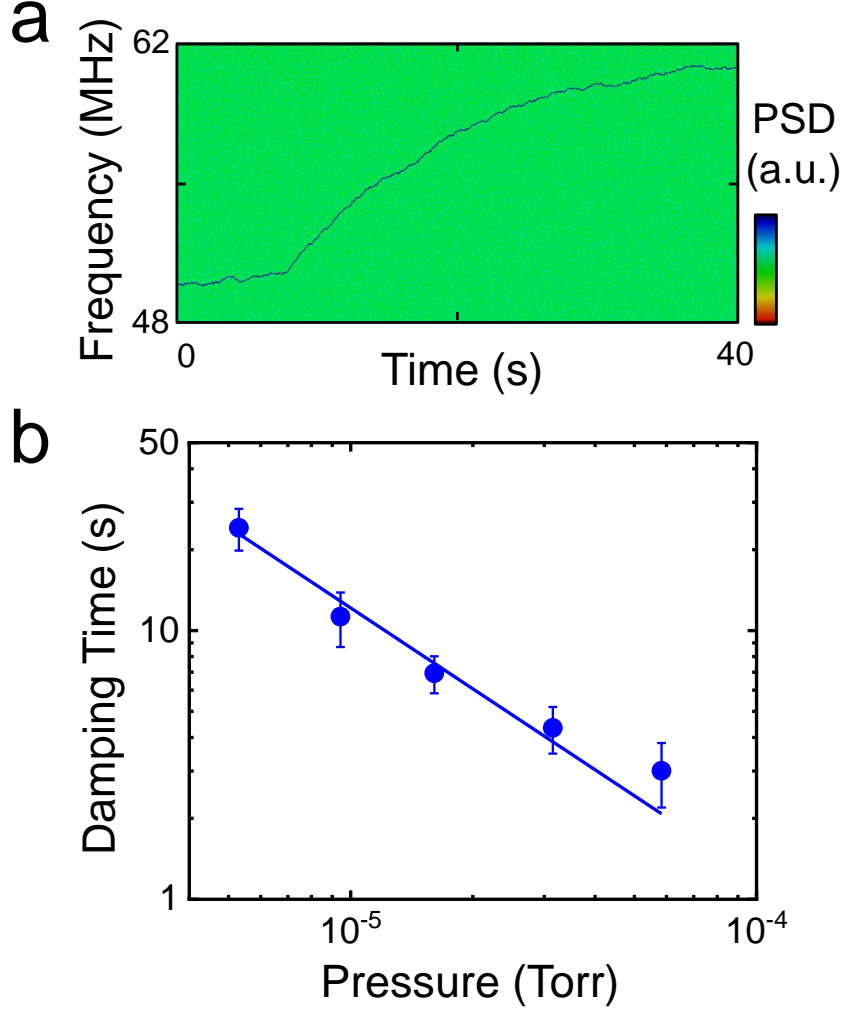
Fig. 4.9. (a) A spectrogram of the rotating silica nanosphere showing the measurements of the rotational damping at a pressure of $9.4 \times 10^{-6}$ torr. At 8 s, the laser for external torque is switched on, and the rotation accelerates following an exponential curve until the maximum frequency is reached. The rotational damping time is acquired from a fitting to an exponential curve. (b) The measured rotation damping time versus air pressure. The solid line depicts the rotation frequency inversely dependent to the air pressure.

Finally, the torque $M_{a.c.}$ is measured by

$$M_{a.c.} = \frac{2}{\Delta t} \int_0^{\Delta t} (\omega_r - \omega_{d.c.}) \sqrt{I_m^2(\omega_{mod}^2 + \gamma^2)} sin(\omega_{mod}t + \phi)dt \qquad (4.14)$$

This equation holds when the measurement time $\Delta t$ is an integer multiple of the modulation period $2\pi/\omega_m$. The data collected from the experiments similar to that of Fig.4.8 (c) is used to calculate the torque according to the modulation amplitude of the 1020 nm laser. Results from the torque measurements while changing the modulation amplitude of the 1020 nm laser power is shown in Fig. 4.10 (b).

The minimum torque that can be measured with this method is set by the limited torque sensitivity because of the thermal noise torque and the resulting Brownian motion. The lowest measurable torque for a period of $\Delta t$ is

$$M_{min} = \sqrt{\frac{4k_B T I_m \gamma}{\Delta t}} \qquad (4.15)$$

where the signal to noise ratio is one [77, 157]. This minimum detectable torque also depends on the torque sensitivity by $M_{min} = \sqrt{S_T}/\sqrt{\Delta t}$ where $\sqrt{S_T}$ is the torque sensitivity. The torque sensitivity is determined from the torque noise spectral density $S_T$ of the system which is measured from the PSD $S_r(\omega)$ when there is no external torque, $M_{a.c.} = 0$. The measured $S_r(\omega)$ when $M_{a.c.} = 0$ is defined as $S_{noise}(\omega)$. Therefore, the torque noise spectral density can be related to the $S_{noise}$ as

$$S_T = \frac{S_{noise}(\omega)}{|\chi(\omega)|^2} = I_m^2(\omega^2 + \gamma^2)S_{noise}(\omega) \qquad (4.16)$$

If the measurement is limited due to the thermal noise, $S_T = 4k_B T I_m \gamma$. Fig. 4.10 (a) shows the sensitivity acquired from the measured $S_r(\omega)$ at $M_{a.c.} = 0$. The dashed line in yellow depicted in the figure is the average value over the frequency range shown in the plot, and corresponds to $4.3 \times 10^{-27} \mathrm{Nm}/\sqrt{\mathrm{Hz}}$.

The minimum resolvable torque and the corresponding torque sensitivity can also be derived from the torque measurements in Fig. 4.10 (b). The plot includes a measured external torque of $(1.3\pm0.5)\times10^{-27}\mathrm{Nm}$ at a modulation of 3.2 mW and as small as $(4.7\pm3.6)\times10^{-28}\mathrm{Nm}$ at 1.1 mW modulation. The minimum resolvable torque can be determined from standard deviation of the measurements caused by the noise and for the measurements on the smaller torque $(< 3\times10^{-27}\mathrm{Nm})$, the average value of the standard deviation is $(4.2 \pm 1.2) \times 10^{-28}\mathrm{Nm}$. The data were taken over 100 seconds
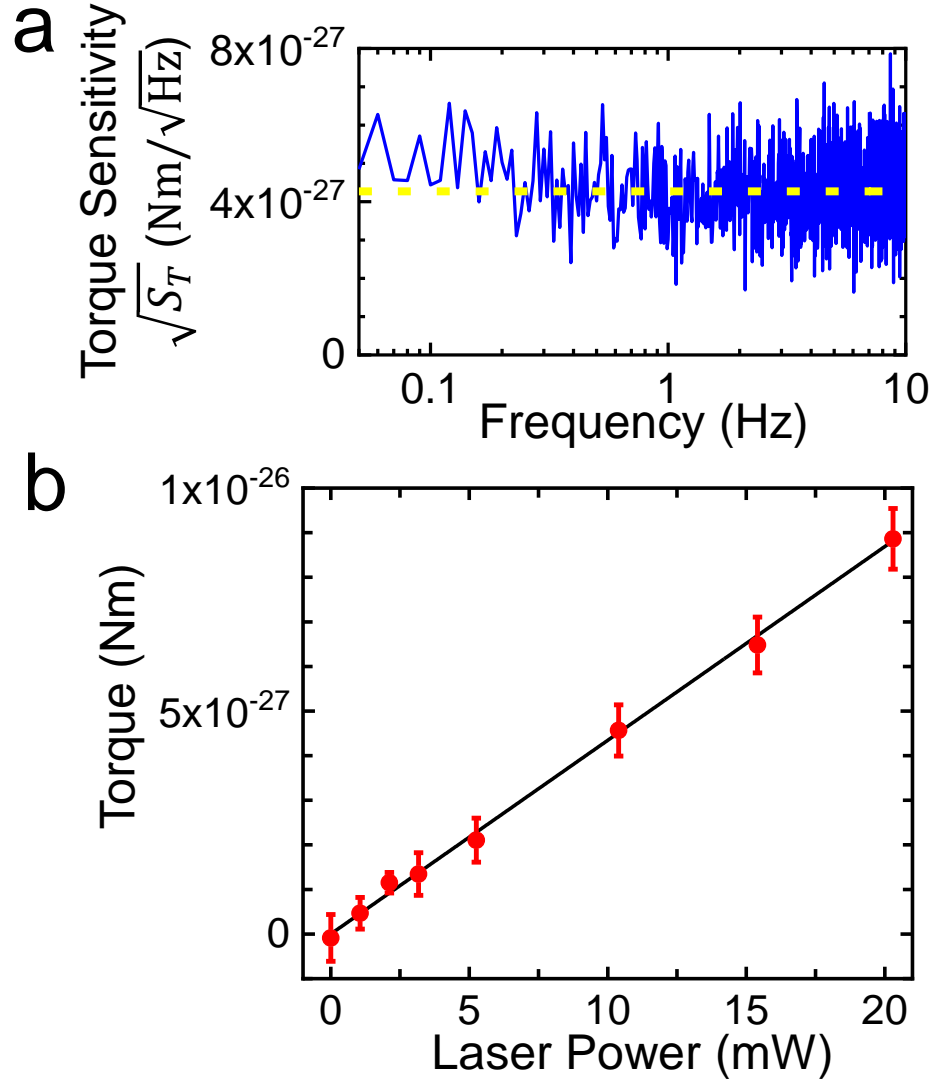
Fig. 4.10. (a) Torque sensitivity $\sqrt{S_T}$ is acquired from the PSD $S_r(\omega)$ when there is no external modulation torque ($M_{a.c.} = 0$). The solid line in blue shows the torque sensitivity and the dashed line in yellow indicates the average over the frequency range plotted in the figure. The corresponding torque sensitivity is $4.3 \times 10^{-27}$Nm/$\sqrt{\text{Hz}}$. (b) The measured torque versus the amplitude of 1020 nm laser power modulation. At a modulation of 1.1 mW, the measured torque is $(4.7 \pm 3.6) \times 10^{-28}$Nm. The standard deviation of the measurements are shown with the error bar.

and at $1.3 \times 10^{-5}$ torr. Therefore the corresponding measured sensitivity would be $(4.2 \pm 1.2) \times 10^{-27} \mathrm{Nm}/\sqrt{\mathrm{Hz}}$. The measured value is comparable to the value from Fig. 4.10 (a). It is also close to the thermal noise limited sensitivity that is calculated to be $3.3 \times 10^{-27} \mathrm{Nm}/\sqrt{\mathrm{Hz}}$ at 300K and at the same pressure. The experimentally measured torque sensitivity achieves a record and exceeds the sensitivity of the most advanced nanofabricated torque sensors at low temperatures [140] by several orders.

## 4.5   Vacuum Friction

An important application the ultrasensitive torque sensor would have is the detection of the vacuum friction [84, 86, 164, 165]. If a neutral nanoparticle rotates at a fast speed the mechanical rotation can transform the quantum and thermal vacuum fluctuations into a radiation emission. In this case, the electromagnetic vacuum will act as if it is a complex fluid that exerts a friction on the rotating particle [84, 86]. This friction is called the vacuum friction. Previous work have proposed the existence of vacuum friction, but the conditions suggested in the theoretical work is yet to be obtained in real experiments. Furthermore, with the larger local density of electromagnetic states, the minute vacuum friction in free space [165] is amplified with a substrate positioned nearby. Under these conditions [84, 86], the optically levitated nanorotor from this work may be suitable for the first measurements on the vacuum friction. According to our calculations, a silica nanosphere rotating at a rate of 1 GHz close to a silica substrate can experience a vacuum friction that is large enough to be measured under reasonable circumstances.

The vacuum frictional torque exerted on a nanosphere that rotates around an axis parallel to a substrate can be expressed as follows [84, 86]

$$M_{vac} = -\frac{2\hbar}{\pi} \int_{-\infty}^{\infty} [n_1(\omega - \Omega) - n_0(\omega)] \times \mathrm{Im}[\alpha(\omega - \Omega)]\mathrm{Im}[\bar{G}(\omega)]d\omega \qquad (4.17)$$

where $n_j(\omega) = [exp(\hbar\omega/k_B T_j) - 1]^{-1}$ is the function of Bose-Einstein distribution at temperature $T_j$, $\Omega$ is the angular velocity of the sphere in rotation, $\alpha$ is the electrical polarizability of the sphere, and $\bar{G}(\omega)$ is the green function which connects the dipole
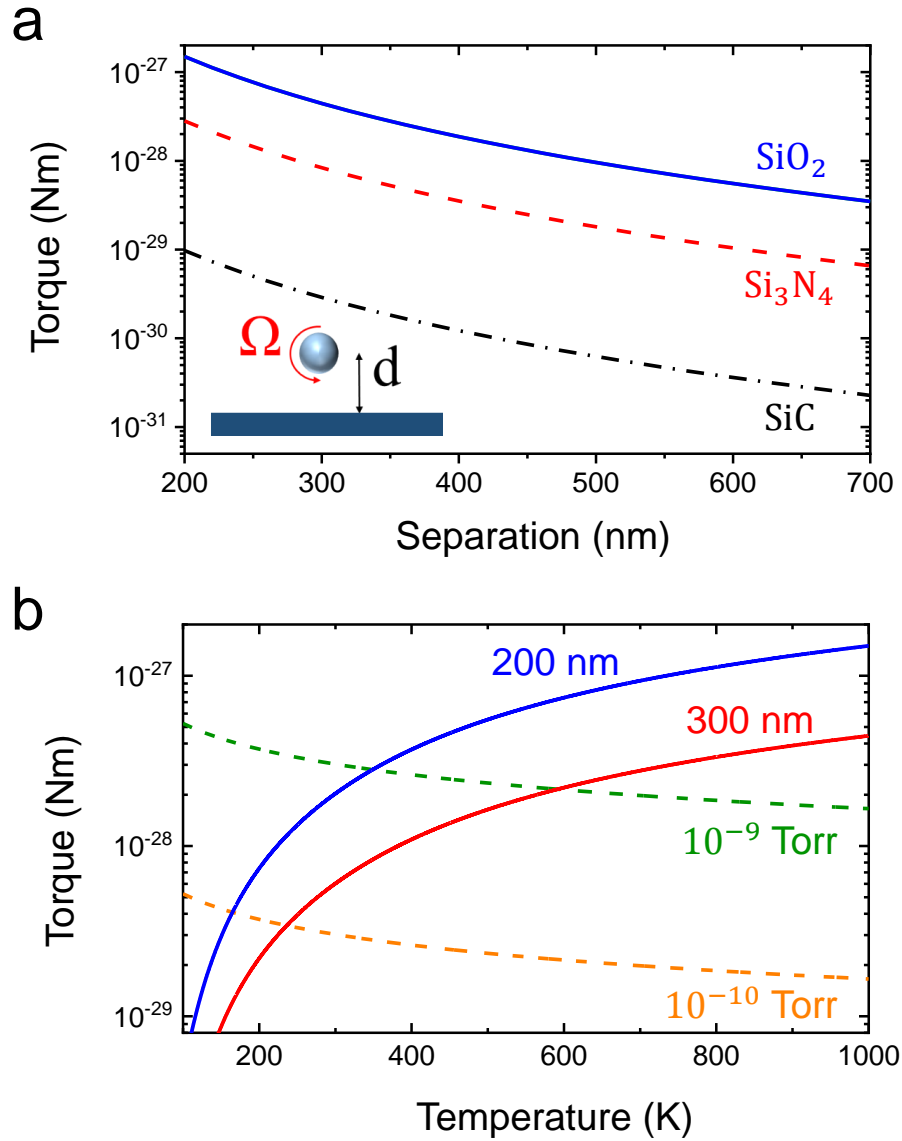
Fig. 4.11. Calculated vacuum frictional torque exerted on a nanosphere rotating close to a substrate. (a) The estimated vacuum friction exerted on a silica nanosphere with a diameter of 150 nm, at 1000 K, and rotating at a rate of 1 GHz versus the separation between the nanosphere and substrates of $SiO_2$, $Si_3N_4$ and SiC. The inset is a figure of a rotating sphere close to a surface. (b) In the case of a silica sphere rotating near a silica substrate, the torque from vacuum friction are depicted in the solid lines and the torque from air damping are depicted in the dashed lines. Both are plotted as a function of temperature. Other parameters are the identical to plot (a).

moment fluctuation of the sphere and the induced electromagnetic field on the substrate surface. Assuming the particle rotates about the z, $\bar{G}(\omega) = [G_{xx}(\omega) + G_{yy}(\omega)]/2$ where $G_{xx}$ and $G_{yy}$ are the Green tensor components [84]. The temperature of the nanosphere $(T_1)$ and the substrate $(T_0)$ are assumed to be the same. The distance $d$ from the sphere to the substrate affects the Green tensor components in

$$G_{xx}(\omega) = G_{zz}(\omega) = G_{yy}(\omega)/2 = \frac{1}{4\pi\epsilon_0(2d)^3}(\frac{\epsilon_{sub}(\omega) - 1}{\epsilon_{sub}(\omega) + 1}) \qquad (4.18)$$

With the equations, the torque from vacuum friction exerted on a 150 nm diameter silica nanopshere rotating at a rate of 1 GHz close to a substrate of three different material of $SiO_2$, $Si_3N_4$ and $SiC$ is calculated for different separations and temperature values. The calculated vacuum friction are plotted in Fig. 4.11.

In Fig. 4.11 (a), one can find that the largest vacuum friction is exerted on the silica nanosphere when the silica surface is selected. This is due to the matching photon polarition modes. At about 200 nm separations, the torque can be approximately $10^{-27} Nm$ which already comparable to the torque values that have been measured in this work. Even smaller torque can be measured with longer measurement time or at lower pressures.

Fig. 4.11 (b) compares the rotational air damping torque on the nanosphere to the vacuum frictional torque. The air damping torque on a sphere is given as [151]

$$M_{air} = \frac{\pi p D^4 \omega}{11.976} \sqrt{\frac{2m_{gas}}{\pi k_B T}} \qquad (4.19)$$

where $D$ is the sphere diameter, and $m_{gas} = 4.6 \times 10^{-26}$ kg is the air molecule's mass. Therefore, the torque from air damping reduces with the increased temperature. Contrarily, the vacuum frictional torque increases with temperature. In Fig. 4.11 (b), the air damping torque at $10^{-9}$ torr (dashed line in green) is smaller than the vacuum frictional torque at 200 nm separation (solid line in blue) when the temperature is larger than 350 K. It is smaller than the vacuum frictional torque at 300 nm separation (red solid line) when the temperature is larger than 590 K. Previous work in levitated optomechanics has demonstrated trapping at similar pressures and at distances closer

than 400 nm from surfaces [32, 168, 169]. Thus, the measurements on vacuum friction will be feasible with the torque measurements with optically levitated nanoparticles.

# 5. OPTICALLY LEVITATED NANODIAMONDS AND NV SPIN CONTROL IN VACUUM

## 5.1 Introduction

A substituted nitrogen atom and a neighboring vacancy in a diamond crystal form a nitrogen vacancy (NV) center. This NV center displays room-temperature quantum coherence and its electron spin can be controlled and read out with microwave and optical fields [102,170,171]. With these unusual features, the NV center has become an important platform for applications ranging from quantum computing and quantum information [94,172] to nanoscale sensing of magnetic and electric fields, temperature, and strain [89–92,173].

The combination of these NV spins with mechanical motions can form a hybrid spin-optomechanical system that may mediate interactions between distinct qubits or allow tests on various fundamental physics [87, 88, 174–176]. Imposing upon the unique platform, recent proposals have proposed to levitate nanodiamonds in vacuum and create large quantum superposition states or test collapse models and quantum gravity [50, 51, 53, 177]. While previous work have demonstrated optical trapping of nanodiamonds in both liquid and air [109–111], the ability to optically trap a nanodiamond in a vacuum environment would be crucial in realizing the above-mentioned proposals. Moreover, the control of the electron spin of the embedded nitrogen vacancies in levitated nanodiamonds in vacuum would allow a mechanical isolation of the nanodiamond from the thermal environment, and realize a strong coupling between the mechanical oscillations and the electron spin.

In the following experimental study, the electron spin resonance from a levitated nanodiamond is observed in low vacuum and the effects of the trap power and background gas are investigated. By varying the surrounding gas with oxygen and helium,

the effects from the gas types are studied with the photoluminescence and the contrast in ESR measurements. The results lead to a future application of NVs as an oxygen gas sensor. The ability to implement electron spin control from a levitated nanodiamond will open up future studies that may develop a spin-optomechanical scheme as a platform for testing various theories of fundamental physics.

## 5.2  Experimental Apparatus
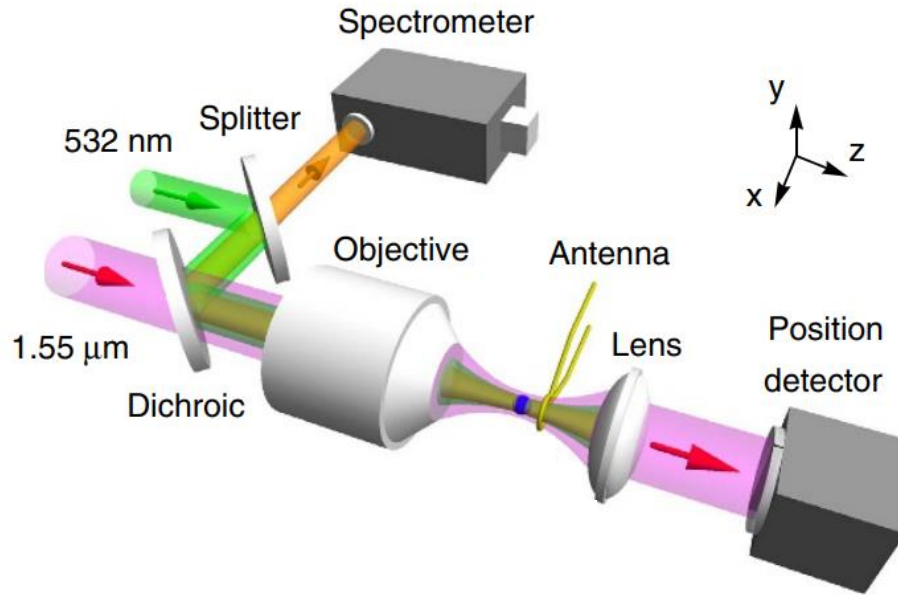


Fig. 5.1. Schematic of experiment. The fluorescent signal of the NV centers is depicted with the orange beam and is detected with the spectrometer and the EMCCD camera. The microwave antenna is used to control the electron spins.

The experimental apparatus used for the current experiment are again similar to that of the system used for the experiments in the former two chapters. It has the same optical levitation system based on a tightly focused 1550 nm trapping laser in a vacuum chamber and uses the same particle loading process with a nebulizer. However, there are some differences in the sample and the experimental setup. First,

instead of silica nanospheres or dumbbell-shaped nanoparticles, nanodiamond samples are used. For the experimental apparatus, in order to take the photoluminescence spectra from the NV centers and to deliver microwave signals for the electron spin control, additional parts were added to the system and will be covered in the following sections.

### 5.2.1 Nanodiamond Sample and Spectrometer
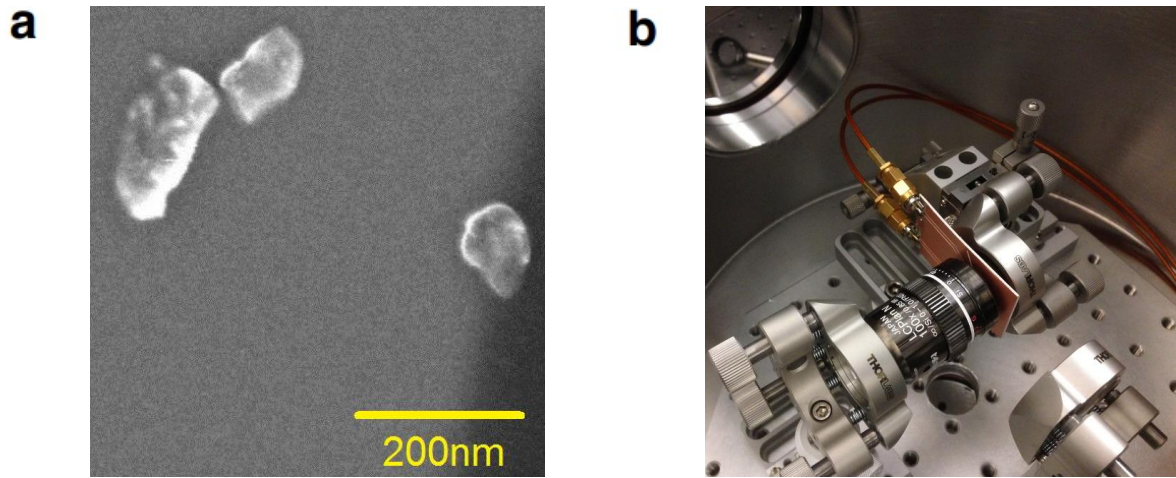


Fig. 5.2. (a) SEM image of nanodiamond sample. (b) Photograph of optical trapping system and microwave antenna inside the vacuum chamber.

A commercially available nanodiamond sample with an size average of 100 nm and with 500 NVs embedded inside (Adamas ND-NV-100nm-COOH) is used throughout the experiment. The sample is diluted in water at a density of approximately 30 $\mu$g/mL, sonicated for about 10 minutes, and is loaded to the optical trap with a nebulizer. The SEM image of the nanodiamond sample is depicted in Fig. 5.2(a). The optical trap is formed with a 1550 nm laser that is guided through an objective lens positioned inside the vacuum chamber. The nanodiamond motion is monitored with the photodetectors after a collimating lens. The trapping procedure is observed

with the 532 nm laser scattered off the trapped nanodiamonds using a CCD camera on the side.
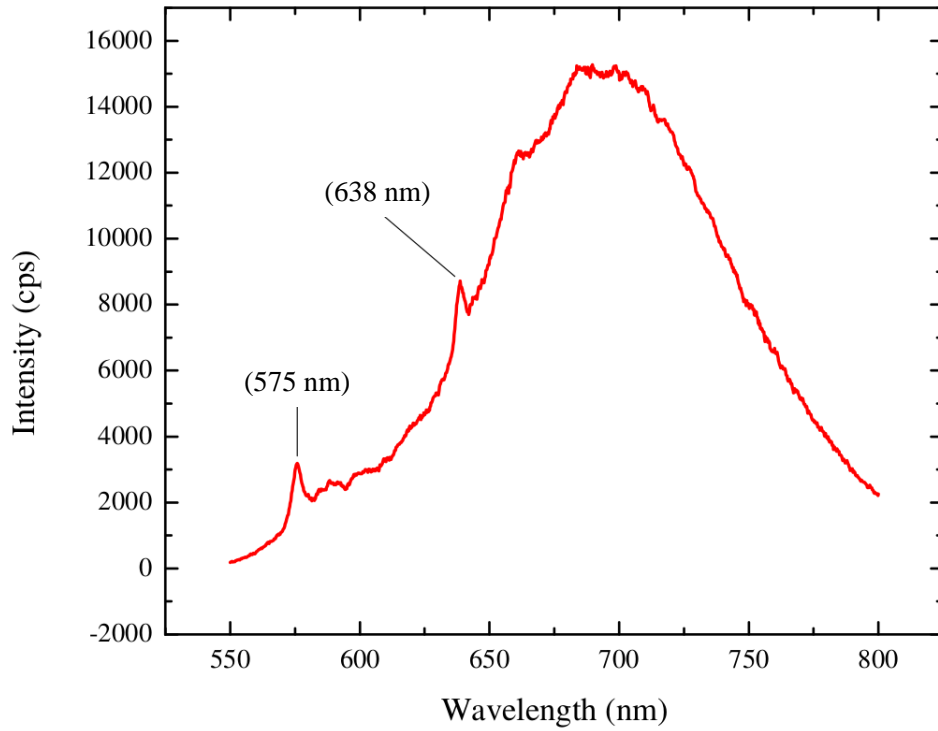


Fig. 5.3. Fluorescence spectra collected from nanodiamond sample prepared on glass slide. The NV$^0$ and NV$^-$ ZPL are identified and the NV$^-$ vibrational sideband can be observed.

For the collection of fluorescence signal from the nanodiamond, a 532 nm excitation laser is directed to the optically trapped nanodiamond following the beam path of the trap laser. With a 950 nm long pass dichroic mirror before the objective lens and additional filters (Thorlabs FES800, FEL550), the signal is guided to the spectrometer (Andor Shamrock SR500i) and an EMCCD camera (Andor Newton DU970P-BV). From the fluorescence, we can observe a unique characteristic of NV$^-$

centers, the zero phonon line (ZPL). For comparison with the fluorescence spectra taken with an optically levitated nanodiamond, the spectra is taken from the same sample on a glass slide. The resulting fluorescence spectra is plotted in Fig. 5.3. The two peaks at ~575 nm and ~638 nm in the figure represents the ZPL of the $NV^0$ and $NV^-$ centers, respectively [91, 178, 179]. The $NV^-$ vibrational side band is also shown from 630 to 800 nm. The signatures in the fluorescence spectra are exploitd to confirm that the particle in the trap is a nanodiamond but not a different particle.

### 5.2.2 Microwave System

For the ESR measurements of the NVs in the levitated nanodiamond, a microwave signal is delivered through a home-made coplanar microwave antenna positioned at about 0.5 mm from the trapping position as in Fig. 5.2(b) [109]. The RF signal generator (Stanford Research Systems SG386) is connected to microwave switches (ZYSWA-2-50DR) which are controlled with pulses generated from an FPGA card (NI USB-7855R). Subsequently the RF signal passes a power amplifier (ZHL-16W-43-S+) and is sent to the coplanar waveguide. Finally, the signal is terminated with a 30 dB fixed attenuator (Pasternack PE7337-30). The setup is shown in the diagram in Fig. 5.4.

The coplanar waveguide is prepared as shown in Fig. 5.5. A CNC machine is used to fabricate the microwave antenna, and based on our tests the power at the microwave antenna is expected to be approximately 30 dB or 1 W.

### 5.3 Optical Levitation of Nanodiamonds in Low Vacuum

As in the previous chapters, the diluted sample is loaded to an ultrasonic nebulizer and is launched into the trap created with a strongly focused 1550 nm laser. The microdroplets evaporate and eventually a nanodiamond is trapped within the vacuum chamber. Finally, the air in the chamber is evacuated with the turbomolecular pump and the nanodiamond is trapped in vacuum.
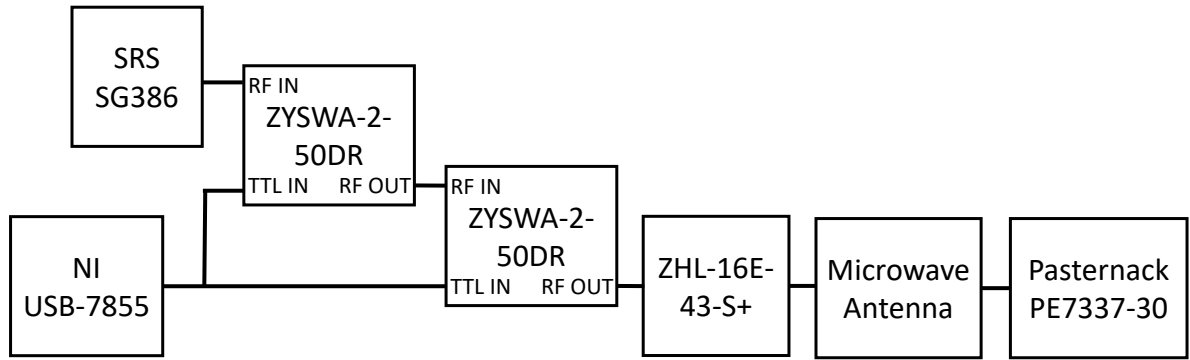
Fig. 5.4. Electronics for microwave control. The RF signal is connected to microwave switches which are controlled with an NI card. The output signal is amplified and connected to the antenna. Finally, the circuit is terminated with an attenuator.
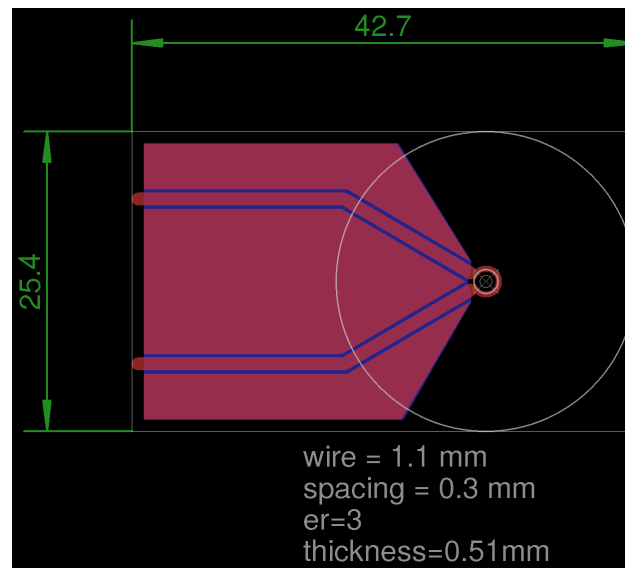


Fig. 5.5. Design of the home-made coplanar microwave antenna.

To check if the trapped particle is a nanodiamond with built-in NVs, the fluorescence signal is analyzed with the spectrometer. As mentioned in the above, the ZPL of a $NV^-$ center is at approximately 637 nm corresponding to the 1.94 eV transition between the $^3A_2$ ground state and the $^3E$ excited state as illustrated in Fig. 5.6 (b).
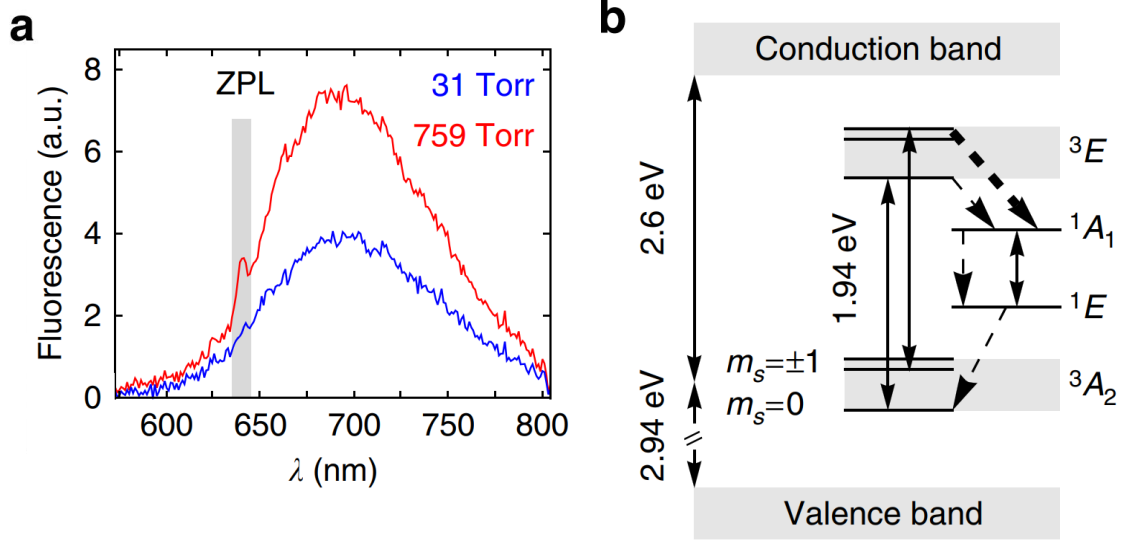
Fig. 5.6. (a) Fluorscence spectra collected in atmospheric pressure and low vacuum. The ZPL of the $NV^-$ center can be identified near 640 nm. (b) $NV^-$ center energy level. The solid arrows indicate the radiative transitions and the dashed arrows show the nonradiative transitions. $^3A_2$, $^1E$, $^1A_1$, $^3E$ indicate the electronic states and $m_s = 0, \pm1$ are the spin states for $^3A_2$.

Fig. 5.6 (a) shows the spectra at 759 torr and 31 torr and the ZPL can be identified near 640 nm. The small deviation from 637 nm is caused by the effects of temperature [92, 102, 180]. Both the fluorescence spectrum signals range from 600 to 800 nm as a result of thermal phonon broadening. The visible fluorescence can be observed to have decreased at lower pressures. At the reduced air pressures less air molecules provide cooling while the heating from laser absorption is unchanged, and therefore the internal temperature of the nanodiamond rises.

Along with the optical spectra from the $NV^-$ centers, the COM motion of the nanodiamond is also investigated. The data on the x direction motion is shown in Fig. 5.7 (a), and at atmospheric pressure the Brownian motion caused by the surrounding air molecules dominates the motion. Therefore, the trapping frequency cannot be observed in the PSD taken at 759 torr. At low vacuum of 31 torr, the

harmonic motion from the optical trap starts to dominate and the resonant peak appears at about 100 kHz. The resulting peak can be fit to a Lorentz curve [152]

$$S_x(\omega) = S_0 \frac{\Gamma_0}{(\Omega_x^2 - \omega^2)^2 - \omega^2\Gamma_0^2} \tag{5.1}$$

Here $S_0 = 2k_BT/m$, $T$ represents the temperature of air, $m$ is the nanodiamond's mass, and the trapping frequency $\Omega_0$ and the damping coefficient $\Gamma_0$ is determined with a fitting. The trapping frequency is subject to the trapping laser power but not the air pressure, and therefore is mostly constant in the range from 300 to 10 torr. The viscous damping coefficient $\Gamma_0/2\pi$ changes with pressure and ranges from around 40 kHz at 31 torr to approximately 500 kHz at atmospheric pressures. The hydrodynamic size of the nanodiamond can be estimated from this viscous damping factor as follows [148, 181].

$$\Gamma_0 = \frac{6\pi\eta r}{\sigma(4/3\pi r^3)} \frac{0.619}{0.619 + K_n}(1 + c_K) \tag{5.2}$$

where $\eta$ stands for the air's dynamic viscosity coefficient, r is the nanodiamond's hydrodynamic radius, $K_n = s/r$ is the Knudesen number, s is the air molecule's mean free path and $c_K = 0.31K_n/(0.785 + 1.152K_n + K_n^2)$. The air molecule's mean free path is [181]

$$s = \frac{\eta}{P}\sqrt{\frac{\pi k_BT}{2m_{air}}} \tag{5.3}$$

where $P$ represents the pressure and $m_{air}$ is the air molecule's mass.

The nanodiamond is considered to be in thermal equilibrium with air molecules at ambient temperature and atmospheric pressure. From the viscosity calculated with Sutherland's formula [182], $\eta \approx 18.52 \times 10^{-6}$ (Pa s) and $s \approx 67$ nm in ambient temperature. With these conditions, the viscous damping factor $\Gamma_0/2\pi = 500$ kHz obtained from the fitting in Fig. 5.7 (a) is used to solve for the $r$ in Eq. 5.2. The obtained diameter size of the nanodiamond is $2r = 94 \pm 7$ nm which is comparable to the manufacturer specification size (100 nm), and is consistent over 30 minutes as shown in Fig. 5.7 (b). The above is not applied for the nanodiamonds trapped in low vacuum since the diamond would have high internal temperature that is not

in thermal equilibrium with the air molecules, and therefore not suitable for the size calculations. Once the pressure is lowered below a certain value, the nanodiamonds escapes from the optical trap as in the case in Fig. 5.7 (d) at 9 torr. Occasionally the diamonds can be trapped at slightly lower pressures but has not been trapped below 1 torr in our experiments.

### 5.3.1  Particle Loss Mechanism

As described in Fig. 5.7 (c), the fluorescence count and the viscous damping factor is collected from an optically levitated nanodiamond at 31 torr for 17 minutes before the diamond is lost. The gradual reduction in the total fluorescence count before loss may seem to indicate that the diamond is burning in residual air at low vacuum [137]. Nonetheless, the viscous damping factor $\Gamma_0/2\pi$ directly related to the size of the diamond is nearly unchanged during the observation implying that the size of the diamond does not have a significant change before loss.

The internal temperature of diamonds can be measured using the ESR signals collected from the NVs. The diamond shown in Fig. 5.7 (c) is found to have an internal temperature of approximately 450 K. Former studies have shown nanodiamond size reduction from air oxidation at atmospheric pressure occurs at approximately 1 nm/h at a temperature of 770 K. Therefore, the nanodiamond trapped at 31 torr with an internal temperature of 450 K should have a negligible size reduction. Therefore the loss is unlikely to be due to the oxidation of the nanodiamond.

The mechanism behind the loss of the nanodiamonds may be related to the Brownian motion of the nanodiamond with an increased temperature. Once the internal temperature of the nanodiamond escalates, the effective temperature of the air molecules also rises [145]. The Brownian motion's mean squared displacement $\langle x^2 \rangle$ is proportional to the effective temperature of gas, and therefore a diamond with increased temperature would experience a larger vibration amplitude before escaping the optical trap. Still, further studies are needed to clarify the loss mechanism
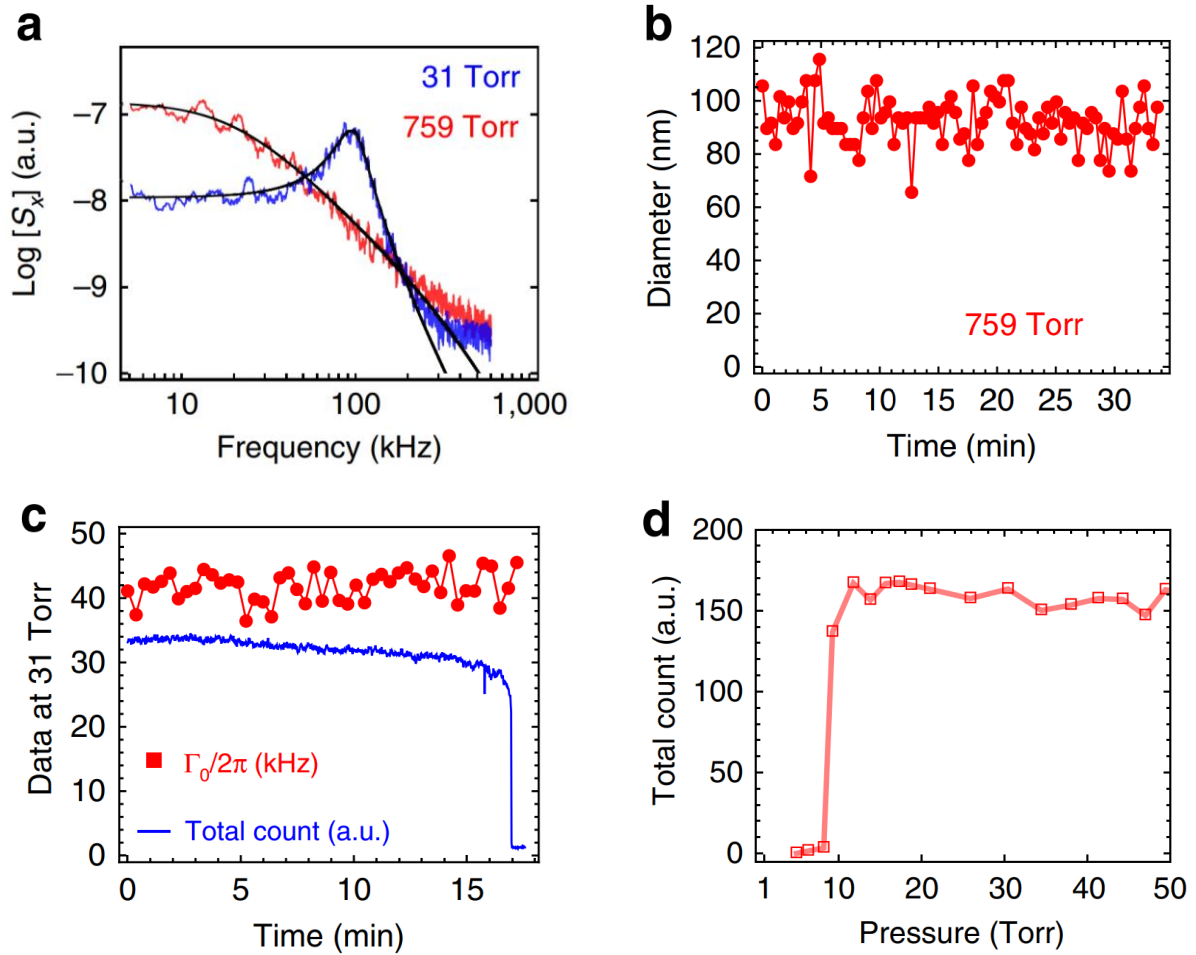
Fig. 5.7. (a) Measured PSD of the COM motion of the trapped nanodiamond in direction perpendicular to the beam propagation. The red line is the PSD at 759 torr and the blue line is the PSD at 31 torr. At low pressures, a resonant peak appears. The black curve is the fitting to the Lorentz curve. (b) The hydrodynamic diameter of the diamond nanoparticle is calculated from the viscous damping $\Gamma_0$ at atmospheric pressure. The size remains the same for over 30 minutes. (c) The viscous damping $\Gamma_0$ and total fluorescence count at 31 torr. The viscous damping remains fairly constant before being lost. (d) Fluorescence count versus air pressure. The nanodiamond is lost at 9 torr. All measurements are implemented with same nanodiamond particle. a.u., arbitrary unit.

of the nanodiamond. Since the nanodiamond is lost at a few torr, the experiments throughout this work are limited to pressures at low vacuum.

### 5.3.2   Electron Spin Resonance Technique

The ESR from the nanodiamonds are collected using the Optically Detected Magnetic Resonance (ODMR) technique which is based on the spin-dependent luminescence [102, 171]. The fluorescence from the excited $NV^-$ center comes from the radiative transisiton from the $^3E$ excited state to the $^3A_2$ ground state. An additional process with a nonradiative decay is available where the $^3E$ excited state relaxes to the $^3A_2$ ground state through metastable states $^1E$ and $^1A_1$. The electron spin state at $m_s = \pm 1$ has a higher probability to decay via the nonradiative decay than the $m_s = 0$ state owing to the different crossover rates, and the nonradiative decay requires more time. Therefore, the fluorescence count rate is weaker at the $m_s = \pm 1$ state compared to that at the $m_s = 0$ state.

In experiments, the microwave lock-in technique is used to excite the electron spin states with microwave pulses and observe the ESR signal [109]. Microwave pulses with on/off sequences that are 500 ms long are delivered with a microwave antenna for a range of frequencies while the nanodiamond is continuously irradiated with the 532 nm laser. Once a resonant microwave frequency causes an electron spin state conversion from the initialized $m_s = 0$ state to the $m_s = \pm 1$ state, a reduction in fluorescence can be observed in the normalized fluorescence signal, $I_{PL}$. The normalized $I_{PL}$ is defined as the count ratio when the microwave excitation is switched on and off and the $1 - I_{PL}$ is defined as the ESR contrast. The minimum position of the $I_{PL}$ is where the ESR peak occurs.

### 5.3.3 Nanodiamond Temperature

The temperature of the nanodiamond can be directly measured from a fitting of the ESR to a double Gaussian function [91, 102, 109]. The Hamiltonian of an NV center in zero-field is [89],

$$H = DS_z^2 + E(S_x^2 - S_y^2) \qquad (5.4)$$

where $D$ is the zero-field splitting between the ground state $m_s = \pm 1$ state and the $m_s = 0$ state and E is the splitting between the $m_s = \pm 1$ from the NV's broken axial symmetry [183]. $D$ corresponds to the center of the double peaks of the ESR spectrum, and $E$ corresponds to the spacing between the peaks. The ambient magnetic field in our experiment is very small and therefore the spacing between the resonance peaks is primarily determined by the zero field parameter $E$. The zero-field splitting parameter $D$ component depends on temperature. $D$ can be written as [184],

$$D(T) = a_0 + a_1 T + a_2 T^2 + a_3 T^3 + \Delta_\text{pressure} + \Delta_\text{strain} \qquad (5.5)$$

where $a_0 = 2.8697$ GHz, $a_1 = 9.7 \times 10^{-5}$ GHz K$^{-1}$, $a_2 = -3.7 \times 10^{-7}$ GHz K$^{-2}$, $a_3 = 1.7 \times 10^{-10}$ GHz K$^{-3}$, $\Delta_\text{pressure} = 1.5$ kHz bar$^{-1}$ [185] and $\Delta_\text{strain}$ is the effect from the internal strain of the nanodiamonds. The shift from the pressure difference is negligible in comparison to the shift from the thermal effects in this experiment. However, each nanodiamond has different $\Delta_\text{strain}$ of around a few MHz, and may cause an inaccuracy of tens of kelvins if neglected. The linear dependence relation between the diamond temperature and the laser power is used to assess the internal strain of individual nanodiamond sample. With Eq. 5.5, the temperatures can be derived from the $D(T)$ which is obtained from the fitting of the ESR to a double Gaussian curve [91, 109]. The internal temperature of diamonds would be 296 K with zero trapping laser power, and with this known temperature at the intersect with the vertical axis of Fig. 5.8 (c) the internal strain $\Delta_\text{strain}$ for each diamond is determined [186].

## 5.4   Effect of Trapping Laser Power on Electron Spin Resonance

First, the effect of the laser that optically traps the nanodiamond is investigated at atmospheric pressure. The power of the trapping laser is changed while trapping the nanodiamond in air, and the change in fluorescence and the ESR spectra are recorded. Additionally, using the ESR spectra, the temperature of the nanodiamond is calculated for the different laser powers.

In Fig. 5.8 (a), the fluorescence is collected with a spectrometer and an EMCCD camera while the levitated diamond is illuminated with a 260 $\mu$W, 532 nm laser. As the trap laser power is decreased from 500 to 60 mW, the fluorescence from the nanodiamond increases by approximately 2.5 times over the whole spectrum.

For the ESR collection in Fig. 5.8 (b), the green laser is reduced to 30 $\mu$W and the laser power for trapping is varied from 500 to 249 mW. The sequence for the collection of individual ESR scan was around 30 minutes which was needed to obtain an ESR curve with a sufficient signal to noise ratio. From collected data, the signal of ESR could be found to increase as the trapping laser was reduced. Later, this signal could be fitted to a double Gaussian function to calculate the internal temperature of the nanodiamonds.

The increase in fluorescence and ESR signal as the trapping laser is reduced can be explained with the effect of heating from the laser and the photoionization [178, 187]. First, the trapping laser absorption can increase the temperature of the trapped nanodiamond and since an escalated temperature increases the nonradiative decay, the lower fluorescence with higher trapping laser power can be explained [184]. Likewise, as the trapping laser is reduced, an increase in the fluorescence signal can be observed.

As well as the heating, the photo-induced ionization from the trapping laser may generate a reduction in the fluorescence. The use of the trapping laser with a wavelength of 1550 nm along with the excitation laserw with a wavelength of 532 nm may lead to an excitation of the electrons in $NV^-$ excited state into the conduction band, and consequently cause an ionization to $NV^0$. More $NV^-$ centers ionized to $NV^0$
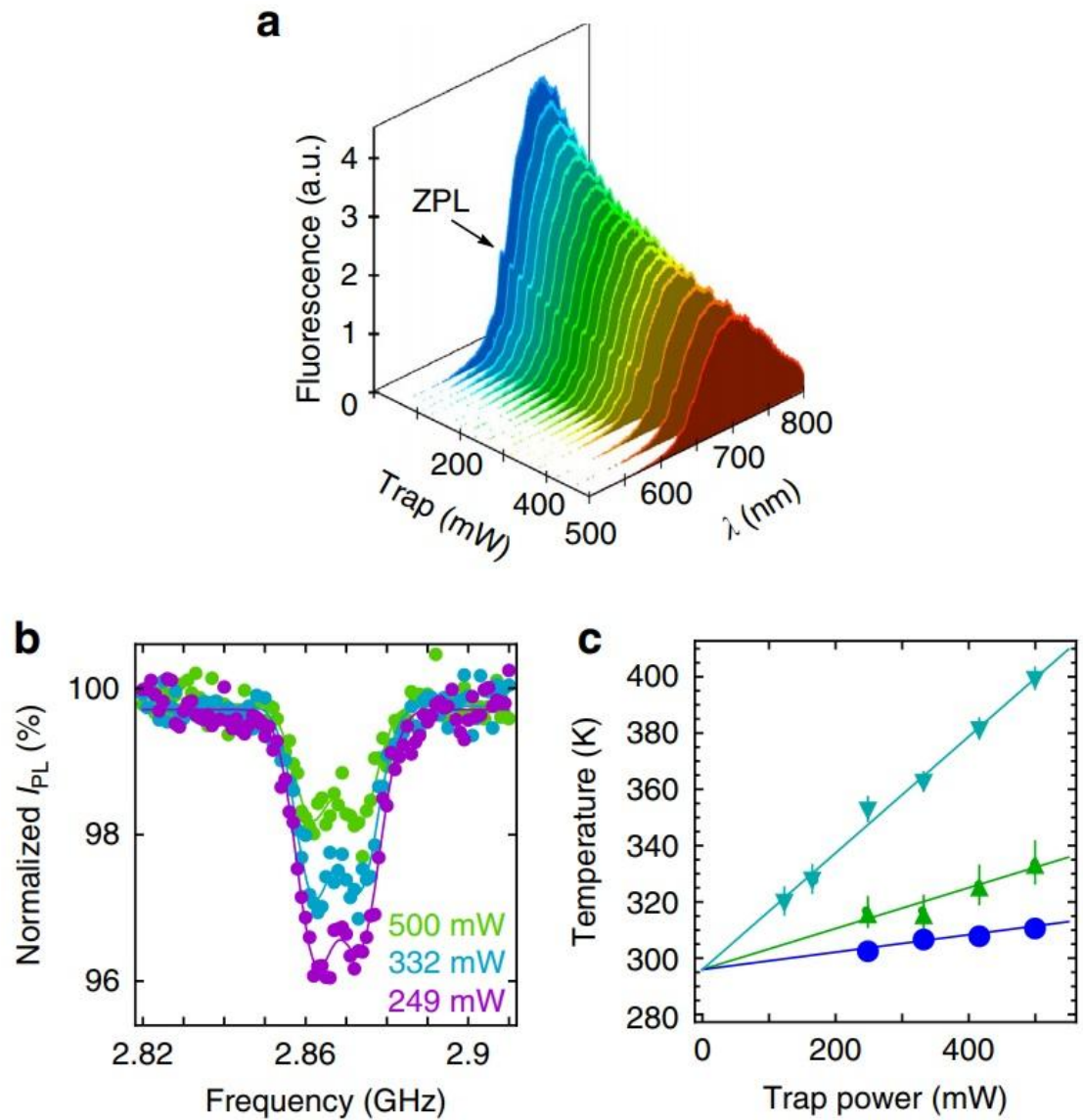
Fig. 5.8. (a) Fluorescence strength versus power of trapping laser. (b) Normalized ESR spectra. The curves of different color are measured at different trapping laser power. (c) Measured internal temperature versus power of trap laser. The error bars correspond to the standard error of the parameters fitted to the ESR spectra. Each marker corresponds to a different diamond particle.

would cause a reduction in the fluorescence signal. Furthermore, the ionization also reduces the ESR contrast. After the recombination from $NV^0$ to $NV^-$ occurs, only about 1/3 of the spin state ends up in $m_s = 0$ state [178] and therefore the reduction in the total population in the $m_s = 0$ state causes a reduced ESR contrast [188].

Finally, the linear temperature dependence to the trap power could be observed as in Fig. 5.8(c). The temperature is calculated from the ESR spectra. Considering the temperature of the diamond would be at room temperature with no trapping laser, the temperature starts from 296 K at 0 mW trap laser. Depending on the sample, the temperature reaches up to 400 K at a trap laser of 500 mW and results show that the temperature increases linearly with the trap power despite the slope is different for each nanodiamond.

## 5.5   Vacuum and ESR

In the second part of the experiment, the effect of the vacuum environment on the optically trapped nanodiamond is studied. Different from the previous measurements at atmospheric pressure [112], as the pressure is lowered the number of air molecules surrounding the levitated nanodiamond reduces, and therefore there is less cooling effect from the collisions with the air molecules. Fig. 5.9(a) shows a shift to the left in the ESR signal as the pressure is lowered, indicating a temperature rise as the pressure is lowered.

The temperature of the levitated nanodiamond is also directly measured from the ESR spectra. The temperature of the diamond rises from 300 to 450 K as the pressure is lowered to 31 torr. As the particle is in the free molecular regime, where the mean free path of the surrounding gas molecules is greater than the levitated diamond sample size, the cooling provided by the gas is proportional to the pressure. Therefore, the increase in temperature is inversely proportional to pressure leading to the relation $T = T_0 + \alpha/p_{\text{gas}}$, where $T_0$ is the room temperature and $\alpha$ is a coefficient depending on the trapped particle, surrounding gas, and the trap laser power. The experimental
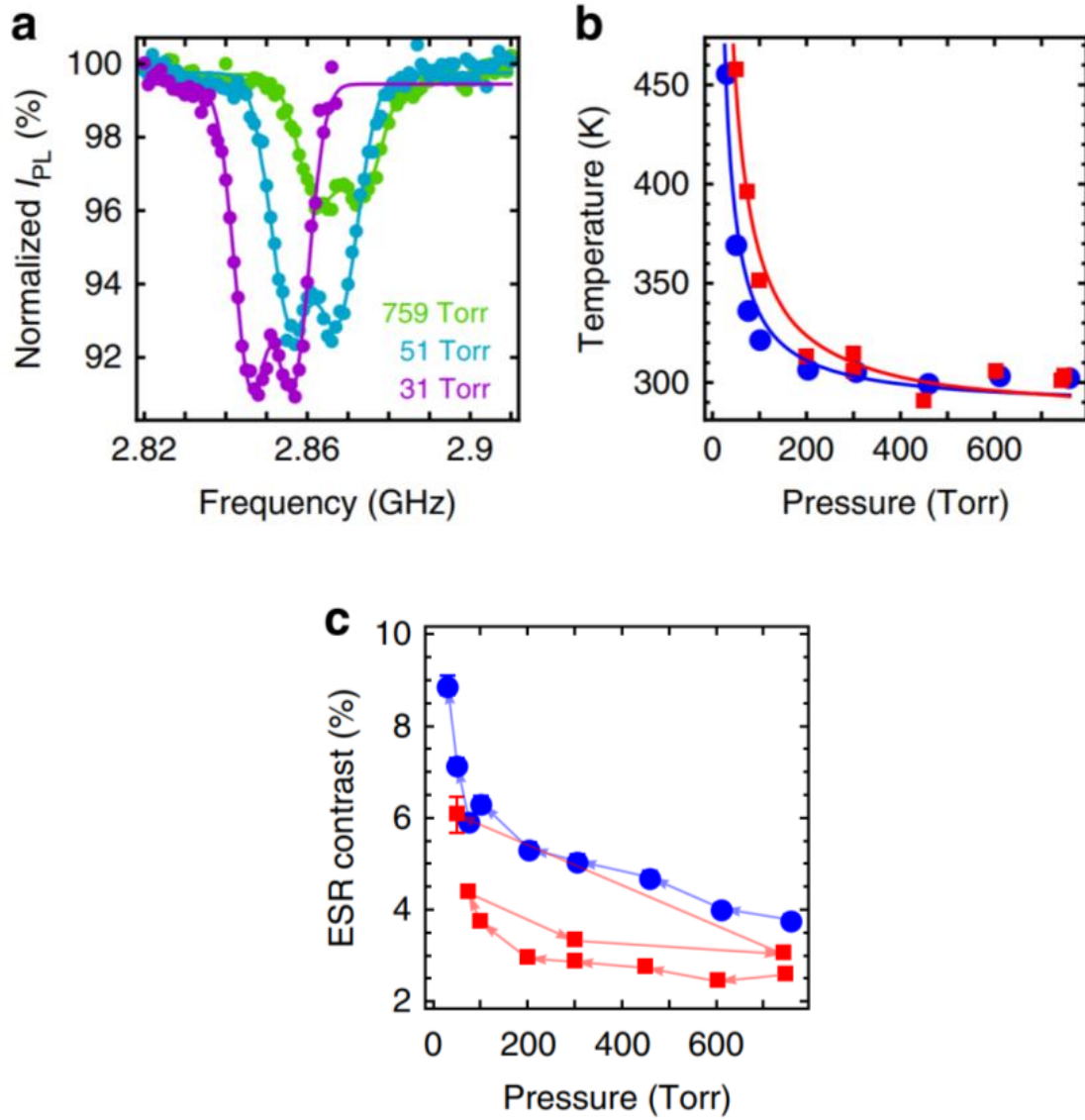
Fig. 5.9. (a) Measured ESR spectra of diamond nanoparticles that are optically levitated at various air pressures. (b) Diamond nanoparticle internal temperature versus air pressure. Each marker corresponds to a different diamond nanoparticle. (c) Sequence of measured ESR contrast as the air pressure is changed. Each marker corresponds to a different diamond nanoparticle.

results are plotted in Fig. 5.9 (b) for two separate nanodiamonds. Both trapped

diamonds show a good agreement to the temperature increase inversely proportional to the pressure.

The ESR contrast was initially expected to decrease as the pressure is lowered due to the increase in temperature [184]. Counter-intuitively, the observations showed a more than two-fold increase in ESR contrast as the pressure was lowered to 31 torr. To test whether the ESR contrast enhancement is an irreversible effect, the ESR is measured while lowering to 74 torr and raising the pressure to atmospheric pressure. From Fig. 5.9 (c), it could found that as the pressure is raised after lowering to low pressure once, the ESR contrast increases minutely compared to the initial contrast. This may be an effect from purification of the nanodiamond as it was exposed to low pressure [189, 190]. However, the ESR contrast becomes significantly smaller when brought back to atmospheric pressures compared to the ESR measured at a low pressure. This implies that the increased ESR contrast is not a permanent effect but a process that is reversible. Therefore, there should be no substantial alteration on the trapped diamond nanoparticle after the exposure to low vacuum and the ESR enhancement at lower pressures should originate from the reduction in the number of air molecules surrounding the levitated nanodiamond.

## 5.6   ESR in Different Gases

In the final part of the experiment, the gas in the vacuum chamber is changed between oxygen and helium during the measurements on a single nanodiamond in order to further study the effects from the surrounding gas. As shown in Fig. 5.10 (a), data were collected in order of oxygen, helium, and the oxygen again. A purity of above 99 % of each gas is managed by repeatedly evacuating and filling the vacuum chamber with the anticipated gas. Additionally, the measurements made for the two cases with oxygen show similar results in both ESR contrast and fluorescence counts, indicating that the effects can be reversed and does not arise from the temporal drift in the system.
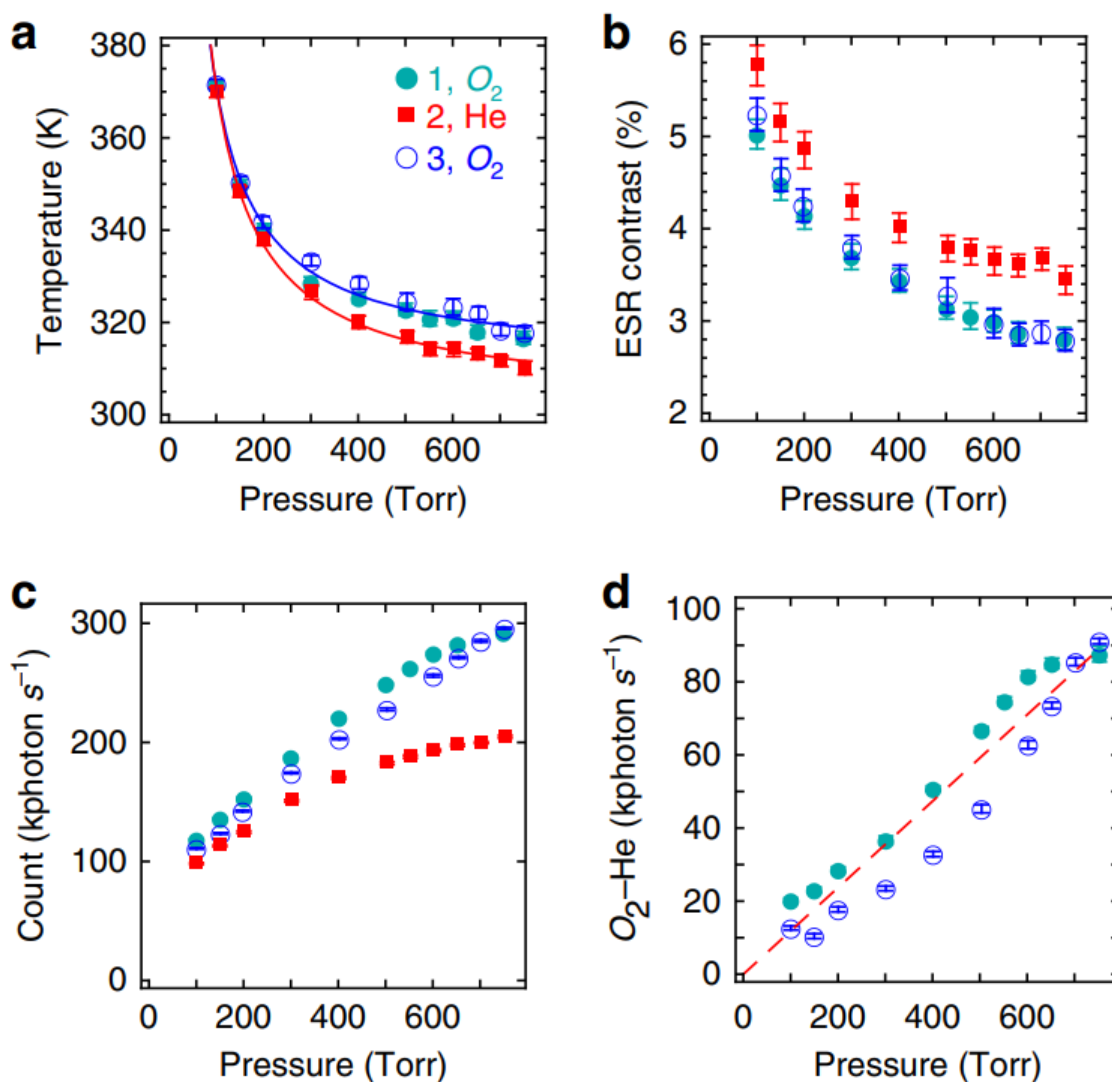
Fig. 5.10. (a) The internal temperature of a single diamond nanoparticle versus the pressure of oxygen and helium gas. (b) The contrast of ESR versus gas pressure compared in an oxygen and helium environment. (c) The measured fluorescence count versus the pressure of oxygen and helium. (d) The fluorescent count difference of a nanodiamond in oxygen and helium versus pressure. The dashed line in red corresponds to the linear fitting to the collected data.

The experiments show that the change in the gas type surrounding the optically levitated nanodiamond have effect on ESR contrast and fluorescence intensity. Fig. 5.10 (b) shows the ESR contrast in a helium environment is approximately 25% larger than in oxygen. Fig. 5.10 (c) shows that the fluorescence strength is about 30% weaker in the helium close to atmospheric pressures. However, in both gases, the ESR contrast increases and the fluorescence count decreases when the pressure is reduced. The effects from the different gases cannot be explained with the change in temperature since the fluorescence count is weaker in helium even though the temperature is lower in helium due to helium's higher thermal conductivity. Normally, the fluorescence strength would increase at lower temperatures.

The effect from the surrounding gas can originate from the lessened oxygen termination and the resulting decrease in the number of low quality $NV^-$s close to the surface [191, 192], and a small temperature rise that can quench the low quality $NV^-$ centers while not causing a significant effect on the $NV^-$ centers closer to the innermost part of the diamond nanoparticle [193]. The $NV^-$ centers at the surface have been shown to have stronger nonradiative decay which may lead to a reduced ESR contrast and a greater temperature dependence. It has also been demonstrated that the fluorescence from NV centers in diamond nanoparticles with a size of 20 to 30 nm decrease by 10 to 40% at 400 K [193] while NV centers in larger diamond samples is only reduced by a few percent at 450 K [184]. The nanodiamond samples used in the experiments have about 100 nm diameter and approximately 500 NV centers. As plotted in Fig. 5.10 (c), as air pressure is reduced, the temperature rises and causes the fluorescence from the low quality $NV^-$ centers to be suppressed. Since the NVs closer to the center of the diamond nanoparticle are less affected by the escalated temperature while the shallow NVs quench, the overall ESR contrast grows as the pressure is reduced (Fig. 5.10 (b)).

Furthermore, a large portion of NVs are in the charge state of $NV^0$ which has a weaker fluorescence strength and absence of ESR at 2.8 GHz [179, 194]. The oxygen termination permits a larger number of NV centers to be in the $NV^-$ state and causes

an increase of fluorescence in an oxygen environment as depicted in Fig. 5.10 (c). The NV$^-$s near the surface which are enabled from the oxygen gas has low ESR contrast and therefore the ESR contrast decreases in oxygen gas depicted in Fig 5.10 (b).

### 5.6.1  NV center Oxygen Gas Sensor

While oxygen can be used for a permanent surface termination [179, 191, 192], the experiments above have shown that oxygen termination can occur in an air environment, at temperatures close to room temperature, and can be reversed. Therefore, the NVs in the diamond nanoparticle can be exploited as a repeatably usable oxygen gas sensor. If the fluorescence counts collected from diamond in helium serves as a reference for the thermal effects, the variation in fluorescence for oxygen and helium turn out to show a close to linear dependence on air pressure in the range of data shown in Fig. 5.10 (d). The measured count differences are compared to a linear fit shown with the dashed line and follows the linear dependence fairly well except at the high pressures. The deviation from the linear fit at high pressures may be due to the limited maximum counts coming from the limited number of NVs in the diamond sample. However, the imaging system that is not yet optimized can already measure around 100 photon torr$^{-1}$s$^{-1}$. For future applications as an oxygen gas sensor, the nanodiamonds may be deposited on a surface instead of being optically levitated.

The zirconia sensor is the most universally used oxygen gas sensor [195, 196]. The zirconia sensor is based on an electrochemical fuel cell that is capable of expending some of the oxygen to produce an output voltage that depends on the concentration of oxygen in the environment. It also requires a heat up process for an effective measurement. Our nanodiamond oxygen gas sensor would not expend the oxygen and would eliminate the heat up process. Furthermore, the nanodiamond oxygen gas sensor could be made to be smaller and the sensitivity can be improved by employing multiple nanodiamonds.

# 6. CONCLUSION AND OUTLOOK

## 6.1 Precision Torque Measurements with Levitated Nanoparticles

Systems of levitated optomechanics have the advantage of having a great thermal isolation from the surrounding environment and therefore is often used for purposes of precision measurements. In the present thesis, an ultrasensitive torque detection has been demonstrated with optically levitated nanoparticles. The system does not require nanofabrication or a cryogenic environment and therefore will be applicable for studies of precision torque measurements. Furthermore, while a torque as small as $(4.7 \pm 3.6) \times 10^{-28} Nm$ has been measured, the value can be enhanced by either measuring the torque for an extended period or trapping the nanorotor at higher vacuum where the rotational damping rate is smaller. With the ability to detect the unprecedented levels of torque, the optically levitated torque sensor can be used for various precision measurement applications that could not have been possible with other systems. In the following section, the opportunities for the experimental observation of radiation shot noise and vacuum friction will be discussed.

### 6.1.1 Radiation Shot Noise

At high pressures, the damping forces exerted on the optically levitated nanoparticle is dominated by the gas damping. The damping from the surrounding gas reduces as the pressure is lowered and can improve the sensitivity when the system is used for precision measurements. At high vacuum, the effect from gas damping becomes minute and the damping is mainly influenced by the photon shot noise.

The photon shot noise originates from the particulate characteristics of light. The momentum from individual photons are transmitted to the levitated particle through

light scattering and photon recoil determines the damping rate of the particle in high vacuum. Previously, the radiation pressure shot noise on a levitated nanosphere has been observed with an optically trapped nanosphere at pressures below $10^{-6}$ torr [59]. In this former study, the photon recoil heating was directly observed along the direction perpendicular to both the polarization and propagation directions. According to a recent work, the heating rate in a linearly polarized laser were found to be distributed by 1/10 in direction of polarization, 7/10 in direction of propagation, and 2/10 in direction that is perpendicular to the other two directions [197, 198]. As a result, when the laser polarization is in parallel to X and the laser propagates towards the Z, the shot noise heating rate for each DOF is expected to be as follows:

$$\Gamma_x = \frac{1}{10} \frac{\omega_0 P_{scatt}}{mc^2 \omega_x} = \frac{1}{10} \frac{\hbar k^2}{m \omega_x} J_p \left( \frac{8\pi}{3} \right) \left( \frac{\alpha k^2}{4\pi\varepsilon_0} \right)^2 \tag{6.1}$$

$$\Gamma_y = \frac{2}{10} \frac{\omega_0 P_{scatt}}{mc^2 \omega_y} = \frac{2}{10} \frac{\hbar k^2}{m \omega_y} J_p \left( \frac{8\pi}{3} \right) \left( \frac{\alpha k^2}{4\pi\varepsilon_0} \right)^2 \tag{6.2}$$

$$\Gamma_z = \frac{7}{10} \frac{\omega_0 P_{scatt}}{mc^2 \omega_z} = \frac{7}{10} \frac{\hbar k^2}{m \omega_z} J_p \left( \frac{8\pi}{3} \right) \left( \frac{\alpha k^2}{4\pi\varepsilon_0} \right)^2 \tag{6.3}$$

where $J_p = I/(\hbar \omega_0)$ and $P_{scatt} = \sigma_{scatt} I$ where the scattering cross-section is $\sigma_{scatt} = \left( \frac{8\pi}{3} \right) \left( \frac{\alpha k^2}{4\pi\varepsilon_0} \right)^2 = \alpha^2 k^4/(6\pi\varepsilon_0^2)$. With a sufficient level of vacuum, our system will be able to experimentally verify the calculations on the translational shot noise heating rate in all three directions.

Furthermore, since photons carry both linear and angular momentum, a radiation torque shot noise can also be predicted. As in the experiments presented above, the polarization of the trapping laser can be altered between linear, elliptical, and circular polarization. The heating rate from rotational shot noise has also been studied for the different polarizations. In a linearly polarized laser where a symmetric particle aligns its symmetry axis to the polarization direction and oscillates within a small angle, the amount of shot noise in each Euler angle is as follows [197]:

$$\left( \dot{E}_\alpha, \dot{E}_\beta, \dot{E}_\gamma \right) = J_p \left( \frac{8\pi}{3} \right) \left( \frac{k^2}{4\pi\varepsilon_0} \right)^2 (\alpha_z - \alpha_x)^2 \left( \frac{\hbar^2}{2I_x} \right) (1, 1, 0) \tag{6.4}$$

where $I_x$ corresponds to the moment of inertia perpendicular to the symmetry axis and $\alpha_x, \alpha_z$ are the polarizability along the axis parallel and perpendicular to the axis of symmetry. For an elliptically polarized laser defined as $\mathbf{E} = E_0\langle\cos\psi, i\sin\psi, 0\rangle$, the distribution of the energy is as the following [197]:

$$\left(\dot{E}_\alpha, \dot{E}_\beta, \dot{E}_\gamma\right) = J_p\left(\frac{8\pi}{3}\right)\left(\frac{k^2}{4\pi\varepsilon_0}\right)^2 (\alpha_z - \alpha_x)^2 \left(\frac{\hbar^2}{2I_x}\right)(1, \cos^2\psi, 0) \qquad (6.5)$$

Depending on the particle geometry, particle size, the dielectric constant of the particle, and the beam parameters, the shot noise in the rotational DOF can be comparable to or even larger than the translational shot noise. Therefore, with a nonspherical particle optically levitated in high vacuum will enable the examination of both the translational and rotational shot noise. An observation on the radiation torque shot noise on a levitated nanoparticle will serve as an experiment revealing the quantum nature of the angular momentum of light.

## 6.1.2  Vacuum Friction

Another important potential experiment with the optically levitated nanorotor is the detection of the vacuum friction [84, 86, 164, 165]. Vacuum friction occurs from an interplay among a moving surface and a vacuum electromagnetic field that induces a drag. For a neutral nanoparticle rotating at a high rotation rate, the quantum and thermal vacuum fluctuations can be converted to a radiation. As a consequence, the electromagnetic vacuum applies a frictional torque, the vacuum friction, on the particle [84, 86].

The vacuum friction in free space may be too small to be measured [165], but the friction can be magnified with a nearby surface which can provide a large local density of electromagnetic states [84, 86]. Therefore, if the optically levitated nanorotor could be trapped in high vacuum and at a position with a surface nearby, our system may enable the first measurements on the vacuum friction. Previous studies have demonstrated optical levitation at pressures below $10^{-8}$ torr [61] and at a position less than 400 nm away from a surface [168, 169]. As a result, the experimental measurement on

vacuum friction will be attainable with the rotating levitated nanoparticle in realistic conditions.

To realize the experiments, the pressure attained in the vacuum chamber needs to be in the order of $10^{-8}$ torr or below. Furthermore, to verify the observations on the vacuum friction, the distance between the substrate and the trapped particle needs to be calibrated. Therefore, furture experiments will involve lowering the pressure inside the vacuum chamber and adding a nearby substrate and to resolve the separation between the trapped particle and the substrate.

## 6.2  Towards Spin-Optomechanics of Levitated Nanoparticles

In the experiment with levitated nanodiamonds with built-in NV centers, an additional spin DOF has been added to the motional DOF of the mechanical oscillator. This hybrid spin-optomechanical system will allow studies of the quantum interactions between electron spin and both rotational and COM motion. A levitated nanodiamond in vacuum will have the advantage of having a large mechanical quality factor with its great isolation from the thermal environment. The electron spin of NV centers have a long coherence time at room temperature which is advantageous for quantum information science applications. With a magnetic field gradient, the electron spin will be coupled to the motion of the particle and allow sensing and manipulation of the motion of the nanodiamond using the NV electron spin. Such a scheme could provide a unique apparatus for fundamental experiments including macroscopic quantum superposition states and creation of mass wave interference.

### 6.2.1  Levitation of Nanodiamonds in High Vacuum

In order to realize the ambitious proposals stated above, the nanodiamond needs to be trapped in high vacuum. However, our experiments are currently limited to pressures above 1 torr and the nanodiamonds are lost before reaching a lower pressure. This is presumably due to the laser absorption increasing the temperature of the

diamond [41, 112, 137, 199]. Commercially available nanodiamond samples that were used throughout the experiments contain graphitic carbon. Thus, it would have a high trap laser absorption and both the internal temperature and COM temperature would increase due to less cooling from the surrounding gas in the lower pressures. Using a more pure nanodiamond sample with less absorption would be one solution for trapping nanodiamonds in high vacuum [200, 201]. From our results, the temperature of the diamond is expected to be about 450 K when the particle is lost. Since former studies have shown the oxidation reduces the size of diamond particles at a rate of 1 nm per hour at 770 K [190, 202], it can be concluded that the loss of the particle is not from the oxidation or burning of the trapped nanodiamond but from the increase in temperature leading to a larger vibration that eventually causes the particle to be lost. If a nanodiamond sample with less graphitic carbon included could allow the temperature of the diamond to increase less compared to our current sample, optical levitation of nanodiamonds in high vacuum may be achieved as in the experiments with silica nanospheres and dumbbell-shaped nanoparticles.

Another approach that can be used in order to avoid the heating of the nanodiamonds from the trapping laser is to use Paul traps or magneto-gravitational traps instead of an optical trap [31, 203–205]. By removing the source of the optical absorption, the trapping laser, the increase in temperature due to the inefficient heat dissipation in vacuum can be avoided. The levitated nanodiamond particles in Paul traps and magneto-gravitational traps could survive at pressures below $10^{-2}$ torr [31, 203]. Even without the trapping laser, additional lasers are needed for the levitated diamonds for the excitation or the spin control on the NV centers and this may prevent the nanodiamonds to be trapped in lower pressures. Future experiments may use shorter laser pulses for such purposes to conduct experiments at lower pressures which may enable a strong coupling between the mechanical DOF and the spin [30, 55]. An additional challenge that may need to resolved is that the trapping frequencies in Paul traps and magneto-gravitational traps are lower compared to that of optical traps, which may limit the coupling of the spin to the particle motion.

### 6.2.2 Quantum Interaction between Motion of a Levitated Nanodiamond and Electron Spin

Once a diamond nanoparticle with NV centers is levitated at high vacuum and a strong coupling of the electron spin and the diamond motion is formed, studies of quantum interaction between the two mechanical degrees of freedom will become possible. The motions that is capable of being coupled to the electron spin includes both the ROT motion and the COM motion of the diamonds. The quantum interactions among the NV electron spin with the motions of a levitated diamond will enable the ambitious investigations of fundamental quantum science and realize applications of quantum based technologies.

Recent work have begun to experimentally study the effects on the NV center electron spins within a diamond in a rotating frame [113, 114]. A diamond sample has been attached on top of an electric motor that could rotate the embedded NV centers at speeds of up to about 3 kHz. Since the spin in the rotating sample would show a precession rate that depends on the frame's rotational angular frequency, an effective magnetic field would appear, similar to that in the Barnett effect. The work used the NV centers to discern the pseudo magnetic fields in the rotating frame which shows the possibility of quantum control with mechanical rotation. Furthermore, experiments have demonstrated quantum measurements from the rotating NV centers providing prospects for probing rotations with a single qubit sensor and potential enhancement in magnetic field detection.

Theoretical proposals based on levitated nanodiamonds have also been introduced for the coupling of the NV spin and the torsional mode [55, 206]. Theory have shown that from the fact that the orientation of a nonspherical particle changes with the torsional vibration or rotational motion, a moderate homogeneous magnetic field becomes sufficient for the strong coupling with spin. Most recently, an experimental work has utilized the coupling between the NV spin and the torsional vibration to reveal a spin-depended torque and also cool the motion of a levitated diamond par-

ticle. The researchers were able to couple the large ensemble of NV spins with the orientation of the trapped microdiamond and reported the observations on the mechanically detected NV spin resonance and the bistability and phonon lasing of the diamond motion.

In future studies, on the basis of recent progress, we will be able to levitate diamonds with single NV centers and induce a faster rotation in vacuum. The small rotational damping from the surrounding gas in the vacuum environment will enable an ultrafast rotation on the levitated nanodiamond similar to the experiments with dumbbell-shaped silica nanoparticles. Provided with the strong coupling between a single spin to the rotational or torsional motion of the trapped diamond in high vacuum, dramatic advances in fields of quantum information science and quantum metrology will be realized. For example, a fast rotating diamond NV center will accumulate a large quantum geometric phase [115] which is imperative for its relations to many nontrivial quantum phenomena. The potential of the platform will not be limited only to fundamental studies but will also bring potential quantum sensing applications such as rotating sensors and NV diamond gyroscopes [116].

Besides the spin coupling to the rotational DOF, the coupling to the COM motion of the levitated diamonds also have appealing research opportunities. Within a magnetic field gradient, a spin state dependent force will be exerted on the electron spin and couple it with the COM motion of the levitated diamond. This scheme will be similar to that of experiments with atoms in that the COM motion can be manipulated and sensed with the internal states. The larger mass of the levitated nanodiamonds will further enable experiments generating large quantum spatial superposition states with the spin-optomechanical coupling [50, 176]. Assuming the oscillations of the levitated nanodiamonds are cooled near to the ground state, the electron spin can be arranged to a quantum superposition state of spin up and spin down. Thus, a magnetic field gradient will exert opposite forces on the two different states and create a superposition of the levitated nanodiamond in two different positions. Since the nanodiamond will be levitated in high vacuum, the mechanical

quality factor will be extremely large which is also beneficial for a strong coupling of the electron spin and the COM motion of the levitated diamond nanoparticle. The generated quantum superposition state can be detected with the time-of-flight measurements which creates a spatial interference pattern. Creating a large quantum superposition state with levitated diamonds will pave way for tests on objective collapse models of quantum wavefunctions and the building of nanoparticle matter-wave interferometry [48, 51–53].

In conclusion, a hybrid quantum electron spin-optomechanical system with a levitated nanodiamond will achievable with the coupling of the internal NV spin and the diamond's rotation or COM motion. In order to accomplish the strong coupling in high vacuum, additional efforts such as the production of pure nanodiamond samples or levitation and quantum control with modified schemes of Paul traps and magneto-gravitational traps are required. The spin-optomechanical configuration will provide a platform for realizing the elaborate experiments for precision measurements, quantum metrology, quantum information, and versatile tests on fundamental physics.

REFERENCES

# REFERENCES

[1] J. C. Maxwell, *A treatise on electricity and magnetism*. Clarendon press, 1881.

[2] P. Lebedev, "Investigations on the pressure forces of light," *Ann. Phys*, vol. 6, pp. 433–458, 1901.

[3] E. F. Nichols and G. F. Hull, "The pressure due to radiation," *Proceedings of the American Academy of Arts and Sciences*, vol. 38, no. 20, pp. 559–599, 1903.

[4] A. Ashkin, "History of optical trapping and manipulation of small-neutral particle, atoms, and molecules," *IEEE Journal of Selected Topics in Quantum Electronics*, vol. 6, no. 6, pp. 841–856, 2000.

[5] P. H. Jones, O. M. Maragò, and G. Volpe, *Optical tweezers: Principles and applications*. Cambridge University Press, 2015.

[6] S. E. S. Spesyvtseva and K. Dholakia, "Trapping in a material world," *ACS Photonics*, vol. 3, no. 5, pp. 719–736, 2016.

[7] R. A. Beth, "Mechanical detection and measurement of the angular momentum of light," *Physical Review*, vol. 50, no. 2, p. 115, 1936.

[8] A. Ashkin, "Acceleration and trapping of particles by radiation pressure," *Physical Review Letters*, vol. 24, no. 4, p. 156, 1970.

[9] A. Ashkin and J. M. Dziedzic, "Optical levitation by radiation pressure," *Applied Physics Letters*, vol. 19, no. 8, pp. 283–285, 1971.

[10] A. Ashkin and J. Dziedzic, "Stability of optical levitation by radiation pressure," *Applied Physics Letters*, vol. 24, no. 12, pp. 586–588, 1974.

[11] A. Ashkin and J. M. Dziedzic, "Optical levitation in high vacuum," *Applied Physics Letters*, vol. 28, no. 6, pp. 333–335, 1976.

[12] A. Ashkin and J. Dziedzic, "Feedback stabilization of optically levitated particles," *Applied Physics Letters*, vol. 30, no. 4, pp. 202–204, 1977.

[13] A. Ashkin, J. M. Dziedzic, J. Bjorkholm, and S. Chu, "Observation of a single-beam gradient force optical trap for dielectric particles," *Optics Letters*, vol. 11, no. 5, pp. 288–290, 1986.

[14] M. Friese, J. Enger, H. Rubinsztein-Dunlop, and N. R. Heckenberg, "Optical angular-momentum transfer to trapped absorbing particles," *Physical Review A*, vol. 54, no. 2, p. 1593, 1996.

[15] N. Simpson, K. Dholakia, L. Allen, and M. Padgett, "Mechanical equivalence of spin and orbital angular momentum of light: an optical spanner," *Optics Letters*, vol. 22, no. 1, pp. 52–54, 1997.

[16] A. I. Bishop, T. A. Nieminen, N. R. Heckenberg, and H. Rubinsztein-Dunlop, "Optical microrheology using rotating laser-trapped particles," *Physical Review Letters*, vol. 92, no. 19, p. 198104, 2004.

[17] M. Friese, T. Nieminen, N. Heckenberg, and H. Rubinsztein-Dunlop, "Optical alignment and spinning of laser-trapped microscopic particles," *Nature*, vol. 394, no. 6691, p. 348, 1998.

[18] A. La Porta and M. D. Wang, "Optical torque wrench: angular trapping, rotation, and torque detection of quartz microparticles," *Physical Review Letters*, vol. 92, no. 19, p. 190801, 2004.

[19] T. A. Nieminen, N. R. Heckenberg, and H. Rubinsztein-Dunlop, "Optical measurement of microscopic torques," *Journal of Modern Optics*, vol. 48, no. 3, pp. 405–413, 2001.

[20] S. Parkin, G. Knöner, W. Singer, T. A. Nieminen, N. R. Heckenberg, and H. Rubinsztein-Dunlop, "Optical torque on microscopic objects," *Methods in Cell Biology*, vol. 82, pp. 525–561, 2007.

[21] L. Paterson, M. P. MacDonald, J. Arlt, W. Sibbett, P. Bryant, and K. Dholakia, "Controlled rotation of optically trapped microscopic particles," *Science*, vol. 292, no. 5518, pp. 912–914, 2001.

[22] R. Omori, T. Kobayashi, and A. Suzuki, "Observation of a single-beam gradient-force optical trap for dielectric particles in air," *Optics Letters*, vol. 22, no. 11, pp. 816–818, 1997.

[23] T. Li, S. Kheifets, D. Medellin, and M. G. Raizen, "Measurement of the instantaneous velocity of a Brownian particle," *Science*, vol. 328, no. 5986, pp. 1673–1675, 2010.

[24] T. Li, S. Kheifets, and M. G. Raizen, "Millikelvin cooling of an optically trapped microsphere in vacuum," *Nature Physics*, vol. 7, no. 7, p. 527, 2011.

[25] J. Gieseler, B. Deutsch, R. Quidant, and L. Novotny, "Subkelvin parametric feedback cooling of a laser-trapped nanoparticle," *Physical Review Letters*, vol. 109, no. 10, p. 103603, 2012.

[26] B. Kane, "Levitated spinning graphene flakes in an electric quadrupole ion trap," *Physical Review B*, vol. 82, no. 11, p. 115441, 2010.

[27] J. Millen, P. Fonseca, T. Mavrogordatos, T. Monteiro, and P. Barker, "Cavity cooling a single charged levitated nanosphere," *Physical Review Letters*, vol. 114, no. 12, p. 123602, 2015.

[28] A. Kuhlicke, A. W. Schell, J. Zoll, and O. Benson, "Nitrogen vacancy center fluorescence from a submicron diamond cluster levitated in a linear quadrupole ion trap," *Applied Physics Letters*, vol. 105, no. 7, p. 073101, 2014.

[29] I. Alda, J. Berthelot, R. A. Rica, and R. Quidant, "Trapping and manipulation of individual nanoparticles in a planar paul trap," *Applied Physics Letters*, vol. 109, no. 16, p. 163105, 2016.

[30] T. Delord, L. Nicolas, L. Schwab, and G. Hétet, "Electron spin resonance from NV centers in diamonds levitating in an ion trap," *New Journal of Physics*, vol. 19, no. 3, p. 033031, 2017.

[31] J.-F. Hsu, P. Ji, C. W. Lewandowski, and B. D'Urso, "Cooling the motion of diamond nanocrystals in a magneto-gravitational trap in high vacuum," *Scientific Reports*, vol. 6, p. 30125, 2016.

[32] B. R. Slezak, C. W. Lewandowski, J.-F. Hsu, and B. D'Urso, "Cooling the motion of a silica microsphere in a magneto-gravitational trap in ultra-high vacuum," *New Journal of Physics*, 2018.

[33] J. Gieseler and J. Millen, "Levitated nanoparticles for microscopic thermodynamics—a review," *Entropy*, vol. 20, no. 5, p. 326, 2018.

[34] J. Gieseler, J. R. Gomez-Solano, A. Magazzù, I. P. Castillo, L. P. García, M. Gironella-Torrent, X. Viader-Godoy, F. Ritort, G. Pesce, A. V. Arzola *et al.*, "Optical tweezers: A comprehensive tutorial from calibration to applications," *arXiv preprint arXiv:2004.05246*, 2020.

[35] L. Rondin, J. Gieseler, F. Ricci, R. Quidant, C. Dellago, and L. Novotny, "Direct measurement of Kramers turnover with a levitated nanoparticle," *Nature Nanotechnology*, vol. 12, no. 12, pp. 1130–1133, 2017.

[36] T. M. Hoang, R. Pan, J. Ahn, J. Bang, H. Quan, and T. Li, "Experimental test of the differential fluctuation theorem and a generalized Jarzynski equality for arbitrary initial states," *Physical Review Letters*, vol. 120, no. 8, p. 080602, 2018.

[37] J. Gieseler, R. Quidant, C. Dellago, and L. Novotny, "Dynamic relaxation of a levitated nanoparticle from a non-equilibrium steady state," *Nature Nanotechnology*, vol. 9, no. 5, p. 358, 2014.

[38] G. Ranjit, M. Cunningham, K. Casey, and A. A. Geraci, "Zeptonewton force sensing with nanospheres in an optical lattice," *Physical Review A*, vol. 93, no. 5, p. 053801, 2016.

[39] D. Hempston, J. Vovrosh, M. Toroš, G. Winstone, M. Rashid, and H. Ulbricht, "Force sensing with an optically levitated charged nanoparticle," *Applied Physics Letters*, vol. 111, no. 13, p. 133111, 2017.

[40] F. Monteiro, S. Ghosh, A. G. Fine, and D. C. Moore, "Optical levitation of 10-ng spheres with nano-g acceleration sensitivity," *Physical Review A*, vol. 96, no. 6, p. 063841, 2017.

[41] T. M. Hoang, Y. Ma, J. Ahn, J. Bang, F. Robicheaux, Z.-Q. Yin, and T. Li, "Torsional optomechanics of a levitated nonspherical nanoparticle," *Physical Review Letters*, vol. 117, no. 12, p. 123604, 2016.

[42] O. Romero-Isart, M. L. Juan, R. Quidant, and J. I. Cirac, "Toward quantum superposition of living organisms," *New Journal of Physics*, vol. 12, no. 3, p. 033015, 2010.

[43] D. E. Chang, C. Regal, S. Papp, D. Wilson, J. Ye, O. Painter, H. J. Kimble, and P. Zoller, "Cavity opto-mechanics using an optically levitated nanosphere," *Proceedings of the National Academy of Sciences*, vol. 107, no. 3, pp. 1005–1010, 2010.

[44] A. D. Rider, D. C. Moore, C. P. Blakemore, M. Louis, M. Lu, and G. Gratta, "Search for screened interactions associated with dark energy below the 100 $\mu$ m length scale," *Physical Review Letters*, vol. 117, no. 10, p. 101101, 2016.

[45] A. A. Geraci, S. B. Papp, and J. Kitching, "Short-range force detection using optically cooled levitated microspheres," *Physical Review Letters*, vol. 105, no. 10, p. 101101, 2010.

[46] W. Nie, Y. Lan, Y. Li, and S. Zhu, "Effect of the Casimir force on the entanglement between a levitated nanosphere and cavity modes," *Physical Review A*, vol. 86, no. 6, p. 063809, 2012.

[47] A. Arvanitaki and A. A. Geraci, "Detecting high-frequency gravitational waves with optically levitated sensors," *Physical Review Letters*, vol. 110, no. 7, p. 071105, 2013.

[48] O. Romero-Isart, "Quantum superposition of massive objects and collapse models," *Physical Review A*, vol. 84, no. 5, p. 052121, 2011.

[49] Z.-q. Yin, A. A. Geraci, and T. Li, "Optomechanics of levitated dielectric particles," *International Journal of Modern Physics B*, vol. 27, no. 26, p. 1330018, 2013.

[50] Z.-q. Yin, T. Li, X. Zhang, and L. Duan, "Large quantum superpositions of a levitated nanodiamond through spin-optomechanical coupling," *Physical Review A*, vol. 88, no. 3, p. 033614, 2013.

[51] O. Romero-Isart, A. C. Pflanzer, F. Blaser, R. Kaltenbaek, N. Kiesel, M. Aspelmeyer, and J. I. Cirac, "Large quantum superpositions and interference of massive nanometer-sized objects," *Physical Review Letters*, vol. 107, no. 2, p. 020405, 2011.

[52] A. Bassi, K. Lochan, S. Satin, T. P. Singh, and H. Ulbricht, "Models of wavefunction collapse, underlying theories, and experimental tests," *Reviews of Modern Physics*, vol. 85, no. 2, p. 471, 2013.

[53] M. Scala, M. Kim, G. Morley, P. Barker, and S. Bose, "Matter-wave interferometry of a levitated thermal nano-oscillator induced and probed by a spin," *Physical Review Letters*, vol. 111, no. 18, p. 180403, 2013.

[54] J. Bateman, S. Nimmrichter, K. Hornberger, and H. Ulbricht, "Near-field interferometry of a free-falling nanoparticle from a point-like source," *Nature Communications*, vol. 5, p. 4788, 2014.

[55] Y. Ma, T. M. Hoang, M. Gong, T. Li, and Z.-q. Yin, "Proposal for quantum many-body simulation and torsional matter-wave interferometry with a levitated nanodiamond," *Physical Review A*, vol. 96, no. 2, p. 023827, 2017.

[56] G. Ranjit, D. P. Atherton, J. H. Stutz, M. Cunningham, and A. A. Geraci, "Attonewton force detection using microspheres in a dual-beam optical trap in high vacuum," *Physical Review A*, vol. 91, no. 5, p. 051805, 2015.

[57] F. Tebbenjohanns, M. Frimmer, A. Militaru, V. Jain, and L. Novotny, "Cold damping of an optically levitated nanoparticle to microkelvin temperatures," *Physical Review Letters*, vol. 122, no. 22, p. 223601, 2019.

[58] G. P. Conangla, F. Ricci, M. T. Cuairan, A. W. Schell, N. Meyer, and R. Quidant, "Optimal feedback cooling of a charged levitated nanoparticle with adaptive control," *Physical Review Letters*, vol. 122, no. 22, p. 223602, 2019.

[59] V. Jain, J. Gieseler, C. Moritz, C. Dellago, R. Quidant, and L. Novotny, "Direct measurement of photon recoil from a levitated nanoparticle," *Physical Review Letters*, vol. 116, no. 24, p. 243601, 2016.

[60] J. Vovrosh, M. Rashid, D. Hempston, J. Bateman, M. Paternostro, and H. Ulbricht, "Parametric feedback cooling of levitated optomechanics in a parabolic mirror trap," *JOSA B*, vol. 34, no. 7, pp. 1421–1428, 2017.

[61] F. Tebbenjohanns, M. Frimmer, V. Jain, D. Windey, and L. Novotny, "Motional sideband asymmetry of a nanoparticle optically levitated in free space," *Physical Review Letters*, vol. 124, no. 1, p. 013603, 2020.

[62] N. Kiesel, F. Blaser, U. Delić, D. Grass, R. Kaltenbaek, and M. Aspelmeyer, "Cavity cooling of an optically levitated submicron particle," *Proceedings of the National Academy of Sciences*, vol. 110, no. 35, pp. 14 180–14 185, 2013.

[63] D. Windey, C. Gonzalez-Ballestero, P. Maurer, L. Novotny, O. Romero-Isart, and R. Reimann, "Cavity-based 3D cooling of a levitated nanoparticle via coherent scattering," *Physical Review Letters*, vol. 122, no. 12, p. 123601, 2019.

[64] N. Meyer, A. De los Rios Sommer, P. Mestres, J. Gieseler, V. Jain, L. Novotny, and R. Quidant, "Resolved-sideband cooling of a levitated nanoparticle in the presence of laser phase noise," *Physical Review Letters*, vol. 123, no. 15, p. 153601, 2019.

[65] U. Delić, M. Reisenbauer, K. Dare, D. Grass, V. Vuletić, N. Kiesel, and M. Aspelmeyer, "Cooling of a levitated nanoparticle to the motional quantum ground state," *Science*, vol. 367, no. 6480, pp. 892–895, 2020.

[66] H. Shi and M. Bhattacharya, "Coupling a small torsional oscillator to large optical angular momentum," *Journal of Modern Optics*, vol. 60, no. 5, pp. 382–386, 2013.

[67] Y. Arita, A. W. McKinley, M. Mazilu, H. Rubinsztein-Dunlop, and K. Dholakia, "Picoliter rheology of gaseous media using a rotating optically trapped birefringent microparticle," *Analytical Chemistry*, vol. 83, no. 23, pp. 8855–8858, 2011.

[68] Y. Arita, M. Mazilu, and K. Dholakia, "Laser-induced rotation and cooling of a trapped microgyroscope in vacuum," *Nature Communications*, vol. 4, p. 2374, 2013.

[69] Y. Arita, E. M. Wright, and K. Dholakia, "Optical binding of two cooled microgyroscopes levitated in vacuum," *Optica*, vol. 5, no. 8, pp. 910–917, 2018.

[70] F. Monteiro, S. Ghosh, E. C. van Assendelft, and D. C. Moore, "Optical rotation of levitated spheres in high vacuum," *Physical Review A*, vol. 97, no. 5, p. 051802, 2018.

[71] S. Kuhn, A. Kosloff, B. A. Stickler, F. Patolsky, K. Hornberger, M. Arndt, and J. Millen, "Full rotational control of levitated silicon nanorods," *Optica*, vol. 4, no. 3, pp. 356–360, 2017.

[72] S. Kuhn, B. A. Stickler, A. Kosloff, F. Patolsky, K. Hornberger, M. Arndt, and J. Millen, "Optically driven ultra-stable nanomechanical rotor," *Nature Communications*, vol. 8, no. 1, p. 1670, 2017.

[73] P. Nagornykh, J. E. Coppock, J. P. Murphy, and B. Kane, "Optical and magnetic measurements of gyroscopically stabilized graphene nanoplatelets levitated in an ion trap," *Physical Review B*, vol. 96, no. 3, p. 035402, 2017.

[74] A. D. Rider, C. P. Blakemore, A. Kawasaki, N. Priel, S. Roy, and G. Gratta, "Electrically driven, optically levitated microscopic rotors," *Physical Review A*, vol. 99, no. 4, p. 041802, 2019.

[75] J. Ahn, Z. Xu, J. Bang, Y.-H. Deng, T. M. Hoang, Q. Han, R.-M. Ma, and T. Li, "Optically levitated nanodumbbell torsion balance and GHz nanomechanical rotor," *Physical Review Letters*, vol. 121, p. 033603, 2018.

[76] M. Rashid, M. Toroš, A. Setter, and H. Ulbricht, "Precession motion in levitated optomechanics," *Physical Review Letters*, vol. 121, no. 25, p. 253601, 2018.

[77] Z. Xu and T. Li, "Detecting Casimir torque with an optically levitated nanorod," *Physical Review A*, vol. 96, no. 3, p. 033843, 2017.

[78] B. A. Stickler, B. Papendell, S. Kuhn, B. Schrinski, J. Millen, M. Arndt, and K. Hornberger, "Probing macroscopic quantum superpositions with nanorotors," *New Journal of Physics*, vol. 20, no. 12, p. 122001, 2018.

[79] M. Carlesso, M. Paternostro, H. Ulbricht, and A. Bassi, "When Cavendish meets Feynman: A quantum torsion balance for testing the quantumness of gravity," *arXiv preprint arXiv:1710.08695*, 2017.

[80] R. Reimann, M. Doderer, E. Hebestreit, R. Diehl, M. Frimmer, D. Windey, F. Tebbenjohanns, and L. Novotny, "GHz rotation of an optically trapped nanoparticle in vacuum," *Physical Review Letters*, vol. 121, p. 033602, 2018.

[81] E. Le Bourhis, *Glass: mechanics and technology.* John Wiley & Sons, 2014.

[82] M. Schuck, D. Steinert, T. Nussbaumer, and J. W. Kolar, "Ultrafast rotation of magnetically levitated macroscopic steel spheres," *Science Advances*, vol. 4, no. 1, p. e1701519, 2018.

[83] J. Ahn, Z. Xu, J. Bang, P. Ju, X. Gao, and T. Li, "Ultrasensitive torque detection with an optically levitated nanorotor," *Nature Nanotechnology*, vol. 15, no. 2, pp. 89–93, 2020.

[84] R. Zhao, A. Manjavacas, F. J. G. de Abajo, and J. Pendry, "Rotational quantum friction," *Physical Review Letters*, vol. 109, no. 12, p. 123604, 2012.

[85] Y. Guo and Z. Jacob, "Giant non-equilibrium vacuum friction: role of singular evanescent wave resonances in moving media," *Journal of Optics*, vol. 16, no. 11, p. 114023, 2014.

[86] A. Manjavacas, F. J. Rodríguez-Fortuño, F. J. G. de Abajo, and A. V. Zayats, "Lateral Casimir force on a rotating particle near a planar surface," *Physical Review Letters*, vol. 118, no. 13, p. 133605, 2017.

[87] O. Arcizet, V. Jacques, A. Siria, P. Poncharal, P. Vincent, and S. Seidelin, "A single nitrogen-vacancy defect coupled to a nanomechanical oscillator," *Nature Physics*, vol. 7, no. 11, p. 879, 2011.

[88] S. Kolkowitz, A. C. B. Jayich, Q. Unterreithmeier, S. D. Bennett, P. Rabl, J. Harris, and M. D. Lukin, "Coherent sensing of a mechanical resonator with a single-spin qubit," *Science*, p. 1216821, 2012.

[89] G. Balasubramanian, I. Chan, R. Kolesov, M. Al-Hmoud, J. Tisler, C. Shin, C. Kim, A. Wojcik, P. R. Hemmer, A. Krueger *et al.*, "Nanoscale imaging magnetometry with diamond spins under ambient conditions," *Nature*, vol. 455, no. 7213, p. 648, 2008.

[90] J. Taylor, P. Cappellaro, L. Childress, L. Jiang, D. Budker, P. Hemmer, A. Yacoby, R. Walsworth, and M. Lukin, "High-sensitivity diamond magnetometer with nanoscale resolution," *Nature Physics*, vol. 4, no. 10, p. 810, 2008.

[91] V. Acosta, E. Bauch, M. Ledbetter, A. Waxman, L.-S. Bouchard, and D. Budker, "Temperature dependence of the nitrogen-vacancy magnetic resonance in diamond," *Physical Review Letters*, vol. 104, no. 7, p. 070801, 2010.

[92] X.-D. Chen, C.-H. Dong, F.-W. Sun, C.-L. Zou, J.-M. Cui, Z.-F. Han, and G.-C. Guo, "Temperature dependent energy level shifts of nitrogen-vacancy centers in diamond," *Applied Physics Letters*, vol. 99, no. 16, p. 161903, 2011.

[93] J. Wrachtrup and F. Jelezko, "Processing quantum information in diamond," *Journal of Physics: Condensed Matter*, vol. 18, no. 21, p. S807, 2006.

[94] E. Togan, Y. Chu, A. Trifonov, L. Jiang, J. Maze, L. Childress, M. G. Dutt, A. S. Sørensen, P. Hemmer, A. S. Zibrov *et al.*, "Quantum entanglement between an optical photon and a solid-state spin qubit," *Nature*, vol. 466, no. 7307, p. 730, 2010.

[95] L. Childress and R. Hanson, "Diamond NV centers for quantum computing and quantum networks," *MRS Bulletin*, vol. 38, no. 2, pp. 134–138, 2013.

[96] J. Cramer, N. Kalb, M. A. Rol, B. Hensen, M. S. Blok, M. Markham, D. J. Twitchen, R. Hanson, and T. H. Taminiau, "Repeated quantum error correction on a continuously encoded qubit by real-time feedback," *Nature Communications*, vol. 7, p. 11526, 2016.

[97] R. Brouri, A. Beveratos, J.-P. Poizat, and P. Grangier, "Photon antibunching in the fluorescence of individual color centers in diamond," *Optics Letters*, vol. 25, no. 17, pp. 1294–1296, 2000.

[98] C. Kurtsiefer, S. Mayer, P. Zarda, and H. Weinfurter, "Stable solid-state source of single photons," *Physical Review Letters*, vol. 85, no. 2, p. 290, 2000.

[99] N. Bar-Gill, L. M. Pham, A. Jarmola, D. Budker, and R. L. Walsworth, "Solid-state electronic spin coherence time approaching one second," *Nature Communications*, vol. 4, p. 1743, 2013.

[100] P. C. Maurer, G. Kucsko, C. Latta, L. Jiang, N. Y. Yao, S. D. Bennett, F. Pastawski, D. Hunger, N. Chisholm, M. Markham *et al.*, "Room-temperature quantum bit memory exceeding one second," *Science*, vol. 336, no. 6086, pp. 1283–1286, 2012.

[101] E. van Oort, P. Stroomer, and M. Glasbeek, "Low-field optically detected magnetic resonance of a coupled triplet-doublet defect pair in diamond," *Physical Review B*, vol. 42, no. 13, p. 8605, 1990.

[102] A. Gruber, A. Dräbenstedt, C. Tietz, L. Fleury, J. Wrachtrup, and C. Von Borczyskowski, "Scanning confocal optical microscopy and magnetic resonance on single defect centers," *Science*, vol. 276, no. 5321, pp. 2012–2014, 1997.

[103] W. Gao, A. Imamoglu, H. Bernien, and R. Hanson, "Coherent manipulation, measurement and entanglement of individual solid-state spins using optical fields," *Nature Photonics*, vol. 9, no. 6, p. 363, 2015.

[104] M. W. Doherty, N. B. Manson, P. Delaney, F. Jelezko, J. Wrachtrup, and L. C. Hollenberg, "The nitrogen-vacancy colour centre in diamond," *Physics Reports*, vol. 528, no. 1, pp. 1–45, 2013.

[105] Y. Dumeige, M. Chipaux, V. Jacques, F. Treussart, J.-F. Roch, T. Debuisschert, V. M. Acosta, A. Jarmola, K. Jensen, P. Kehayias *et al.*, "Magnetometry with nitrogen-vacancy ensembles in diamond based on infrared absorption in a doubly resonant optical cavity," *Physical Review B*, vol. 87, no. 15, p. 155202, 2013.

[106] A. Nizovtsev, S. Y. Kilin, C. Tietz, F. Jelezko, and J. Wrachtrup, "Modeling fluorescence of single nitrogen–vacancy defect centers in diamond," *Physica B: Condensed Matter*, vol. 308, pp. 608–611, 2001.

[107] E. van Oort and M. Glasbeek, "Fluorescence detected level-anticrossing and spin coherence of a localized triplet state in diamond," *Chemical Physics*, vol. 152, no. 3, pp. 365–373, 1991.

[108] J. Harrison, M. Sellars, and N. Manson, "Optical spin polarisation of the NV centre in diamond," *Journal of Luminescence*, vol. 107, no. 1-4, pp. 245–248, 2004.

[109] V. R. Horowitz, B. J. Alemán, D. J. Christle, A. N. Cleland, and D. D. Awschalom, "Electron spin resonance of nitrogen-vacancy centers in optically trapped nanodiamonds," *Proceedings of the National Academy of Sciences*, vol. 109, no. 34, pp. 13 493–13 497, 2012.

[110] M. Geiselmann, M. L. Juan, J. Renger, J. M. Say, L. J. Brown, F. J. G. De Abajo, F. Koppens, and R. Quidant, "Three-dimensional optical manipulation of a single electron spin," *Nature Nanotechnology*, vol. 8, no. 3, p. 175, 2013.

[111] L. P. Neukirch, J. Gieseler, R. Quidant, L. Novotny, and A. N. Vamivakas, "Observation of nitrogen vacancy photoluminescence from an optically levitated nanodiamond," *Optics Letters*, vol. 38, no. 16, pp. 2976–2979, 2013.

[112] L. P. Neukirch, E. Von Haartman, J. M. Rosenholm, and A. N. Vamivakas, "Multi-dimensional single-spin nano-optomechanics with a levitated nanodiamond," *Nature Photonics*, vol. 9, no. 10, p. 653, 2015.

[113] A. Wood, E. Lilette, Y. Fein, V. Perunicic, L. Hollenberg, R. Scholten, and A. Martin, "Magnetic pseudo-fields in a rotating electron–nuclear spin system," *Nature Physics*, vol. 13, no. 11, p. 1070, 2017.

[114] A. A. Wood, E. Lilette, Y. Y. Fein, N. Tomek, L. P. McGuinness, L. C. Hollenberg, R. E. Scholten, and A. M. Martin, "Quantum measurement of a rapidly rotating spin qubit in diamond," *Science Advances*, vol. 4, no. 5, p. eaar7691, 2018.

[115] D. Maclaurin, M. Doherty, L. Hollenberg, and A. Martin, "Measurable quantum geometric phase from a rotating single spin," *Physical Review Letters*, vol. 108, no. 24, p. 240403, 2012.

[116] M. Ledbetter, K. Jensen, R. Fischer, A. Jarmola, and D. Budker, "Gyroscopes based on nitrogen-vacancy centers in diamond," *Physical Review A*, vol. 86, no. 5, p. 052116, 2012.

[117] T. M. Hoang, J. Ahn, J. Bang, and T. Li, "Electron spin control of optically levitated nanodiamonds in vacuum," *Nature Communications*, vol. 7, no. 1, p. 12250, 2016.

[118] A. Ashkin, J. M. Dziedzic, and T. Yamane, "Optical trapping and manipulation of single cells using infrared laser beams," *Nature*, vol. 330, no. 6150, p. 769, 1987.

[119] K. Svoboda and S. M. Block, "Biological applications of optical forces," *Annual Review of Biophysics and Biomolecular Structure*, vol. 23, no. 1, pp. 247–285, 1994.

[120] T. T. Perkins, "Optical traps for single molecule biophysics: a primer," *Laser & Photonics Reviews*, vol. 3, no. 1-2, pp. 203–220, 2009.

[121] P. C. Ashok and K. Dholakia, "Optical trapping for analytical biotechnology," *Current Opinion in Biotechnology*, vol. 23, no. 1, pp. 16–21, 2012.

[122] A. Ashkin, "Atomic-beam deflection by resonance-radiation pressure," *Physical Review Letters*, vol. 25, no. 19, p. 1321, 1970.

[123] D. J. Wineland, R. E. Drullinger, and F. L. Walls, "Radiation-pressure cooling of bound resonant absorbers," *Physical Review Letters*, vol. 40, no. 25, p. 1639, 1978.

[124] E. Raab, M. Prentiss, A. Cable, S. Chu, and D. E. Pritchard, "Trapping of neutral sodium atoms with radiation pressure," *Physical Review Letters*, vol. 59, no. 23, p. 2631, 1987.

[125] D. C. Moore, A. D. Rider, and G. Gratta, "Search for millicharged particles using optically levitated microspheres," *Physical Review Letters*, vol. 113, no. 25, p. 251801, 2014.

[126] A. Ashkin, "Forces of a single-beam gradient laser trap on a dielectric sphere in the ray optics regime," *Biophysical Journal*, vol. 61, no. 2, pp. 569–582, 1992.

[127] L. P. Neukirch and A. N. Vamivakas, "Nano-optomechanics with optically levitated nanoparticles," *Contemporary Physics*, vol. 56, no. 1, pp. 48–62, 2015.

[128] V. Coffey, "The tiniest traps: optical manipulation gets smaller," *Optics and Photonics News*, vol. 24, no. 4, pp. 24–31, 2013.

[129] Y. Harada and T. Asakura, "Radiation forces on a dielectric sphere in the rayleigh scattering regime," *Optics Communications*, vol. 124, no. 5-6, pp. 529–541, 1996.

[130] C. F. Bohren and D. R. Huffman, *Absorption and scattering of light by small particles.* John Wiley & Sons, 2008.

[131] J. Trojek, L. Chvátal, and P. Zemánek, "Optical alignment and confinement of an ellipsoidal nanorod in optical tweezers: a theoretical study," *JOSA A*, vol. 29, no. 7, pp. 1224–1236, 2012.

[132] L. Novotny and B. Hecht, *Principles of nano-optics.* Cambridge university press, 2012.

[133] J. Gieseler, L. Novotny, and R. Quidant, "Thermal nonlinearities in a nanomechanical oscillator," *Nature Physics*, vol. 9, no. 12, pp. 806–810, 2013.

[134] J. Bang, T. Seberson, P. Ju, J. Ahn, Z. Xu, X. Gao, F. Robicheaux, and T. Li, "5D cooling and nonlinear dynamics of an optically levitated nanodumbbell," *arXiv preprint arXiv:2004.02384*, 2020.

[135] A. A. Rahman and P. Barker, "Laser refrigeration, alignment and rotation of levitated Yb 3+: YLF nanocrystals," *Nature Photonics*, vol. 11, no. 10, p. 634, 2017.

[136] J. E. Coppock, P. Nagornykh, J. P. Murphy, I. McAdams, S. Katragadda, and B. Kane, "Dual-trap system to study charged graphene nanoplatelets in high vacuum," *JOSA B*, vol. 34, no. 6, pp. C36–C43, 2017.

[137] A. Rahman, A. Frangeskou, M. Kim, S. Bose, G. Morley, and P. Barker, "Burning and graphitization of optically levitated nanodiamonds in vacuum," *Scientific Reports*, vol. 6, p. 21633, 2016.

[138] H. Cavendish *et al.*, "XXI. Experiments to determine the density of the earth," *Philosophical Transactions of the Royal Society of London*, vol. 88, pp. 469–526, 1798.

[139] P. H. Kim, C. Doolin, B. D. Hauer, A. J. MacDonald, M. R. Freeman, P. E. Barclay, and J. P. Davis, "Nanoscale torsional optomechanics," *Applied Physics Letters*, vol. 102, no. 5, p. 053102, 2013.

[140] P. Kim, B. Hauer, C. Doolin, F. Souris, and J. Davis, "Approaching the standard quantum limit of mechanical torque sensing," *Nature Communications*, vol. 7, p. 13165, 2016.

[141] V. Parsegian and G. H. Weiss, "Dielectric anisotropy and the van der Waals interaction between bulk media," *The Journal of Adhesion*, vol. 3, no. 4, pp. 259–267, 1972.

[142] S. Van Enk, "Casimir torque between dielectrics," *Physical Review A*, vol. 52, no. 4, p. 2569, 1995.

[143] C. Marletto and V. Vedral, "Gravitationally induced entanglement between two massive particles is sufficient evidence of quantum effects in gravity," *Physical Review Letters*, vol. 119, no. 24, p. 240402, 2017.

[144] S. Bose, A. Mazumdar, G. W. Morley, H. Ulbricht, M. Toroš, M. Paternostro, A. A. Geraci, P. F. Barker, M. Kim, and G. Milburn, "Spin entanglement witness for quantum gravity," *Physical Review Letters*, vol. 119, no. 24, p. 240401, 2017.

[145] J. Millen, T. Deesuwan, P. Barker, and J. Anders, "Nanoscale temperature measurements using non-equilibrium Brownian dynamics of a levitated nanosphere," *Nature Nanotechnology*, vol. 9, no. 6, p. 425, 2014.

[146] P. M. Johnson, C. M. van Kats, and A. van Blaaderen, "Synthesis of colloidal silica dumbbells," *Langmuir*, vol. 21, no. 24, pp. 11 510–11 517, 2005.

[147] T. Li, S. Kheifets, D. Medellin, and M. G. Raizen, "Measurement of the instantaneous velocity of a Brownian particle," *Science*, vol. 328, no. 5986, pp. 1673–1675, 2010.

[148] T. Li, *Fundamental tests of physics with optically trapped microspheres.* Springer Science & Business Media, 2012.

[149] D. W. Mackowski, "Monte Carlo simulation of hydrodynamic drag and thermophoresis of fractal aggregates of spheres in the free-molecule flow regime," *Journal of Aerosol Science*, vol. 37, no. 3, pp. 242–259, 2006.

[150] P. Chan and B. Dahneke, "Free-molecule drag on straight chains of uniform spheres," *Journal of Applied Physics*, vol. 52, no. 5, pp. 3106–3110, 1981.

[151] J. Corson, G. W. Mulholland, and M. R. Zachariah, "Calculating the rotational friction coefficient of fractal aerosol particles in the transition regime using extended Kirkwood-Riseman theory," *Physical Review E*, vol. 96, no. 1, p. 013110, 2017.

[152] K. Berg-Sørensen and H. Flyvbjerg, "Power spectrum analysis for optical tweezers," *Review of Scientific Instruments*, vol. 75, no. 3, pp. 594–612, 2004.

[153] M. C. Wang and G. E. Uhlenbeck, "On the theory of the Brownian motion II," *Reviews of Modern Physics*, vol. 17, no. 2-3, p. 323, 1945.

[154] M. Pitkonen, "Polarizability of the dielectric double-sphere," *Journafl of Mathematical Physics*, vol. 47, no. 10, p. 102901, 2006.

[155] B. T. Draine, "The discrete-dipole approximation and its application to interstellar graphite grains," *The Astrophysical Journal*, vol. 333, pp. 848–872, 1988.

[156] K. Dholakia and P. Zemánek, "Colloquium: Gripped by light: Optical binding," *Reviews of Modern Physics*, vol. 82, no. 2, p. 1767, 2010.

[157] L. Haiberger, M. Weingran, and S. Schiller, "Highly sensitive silicon crystal torque sensor operating at the thermal noise limit," *Review of Scientific Instruments*, vol. 78, no. 2, p. 025101, 2007.

[158] G. Brambilla and D. N. Payne, "The ultimate strength of glass silica nanowires," *Nano Letters*, vol. 9, no. 2, pp. 831–835, 2009.

[159] E. G. Adelberger, J. Gundlach, B. Heckel, S. Hoedl, and S. Schlamminger, "Torsion balance experiments: A low-energy frontier of particle physics," *Progress in Particle and Nuclear Physics*, vol. 62, no. 1, pp. 102–134, 2009.

[160] M. Wu, N. L.-Y. Wu, T. Firdous, F. F. Sani, J. E. Losby, M. R. Freeman, and P. E. Barclay, "Nanocavity optomechanical torque magnetometry and radiofrequency susceptometry," *Nature Nanotechnology*, vol. 12, no. 2, pp. 127–131, 2017.

[161] H. Chan, V. Aksyuk, R. Kleiman, D. Bishop, and F. Capasso, "Quantum mechanical actuation of microelectromechanical systems by the Casimir force," *Science*, vol. 291, no. 5510, pp. 1941–1944, 2001.

[162] J. E. Losby, V. T. Sauer, and M. R. Freeman, "Recent advances in mechanical torque studies of small-scale magnetism," *Journal of Physics D: Applied Physics*, vol. 51, no. 48, p. 483001, 2018.

[163] L. He, H. Li, and M. Li, "Optomechanical measurement of photon spin angular momentum and optical torque in integrated photonic devices," *Science Advances*, vol. 2, no. 9, p. e1600485, 2016.

[164] M. Kardar and R. Golestanian, "The "friction" of vacuum, and other fluctuation-induced forces," *Reviews of Modern Physics*, vol. 71, no. 4, p. 1233, 1999.

[165] A. Manjavacas and F. G. De Abajo, "Vacuum friction in rotating particles," *Physical Review Letters*, vol. 105, no. 11, p. 113601, 2010.

[166] X.-Y. Chen, T. Li, and Z.-Q. Yin, "Nonadiabatic dynamics and geometric phase of an ultrafast rotating electron spin," *Science Bulletin*, vol. 64, no. 6, pp. 380–384, 2019.

[167] F. Ricci, M. T. Cuairan, G. P. Conangla, A. W. Schell, and R. Quidant, "Accurate mass measurement of a levitated nanomechanical resonator for precision force-sensing," *Nano Letters*, vol. 19, no. 10, pp. 6711–6715, 2019.

[168] R. Diehl, E. Hebestreit, R. Reimann, F. Tebbenjohanns, M. Frimmer, and L. Novotny, "Optical levitation and feedback cooling of a nanoparticle at sub-wavelength distances from a membrane," *Physical Review A*, vol. 98, no. 1, p. 013851, 2018.

[169] L. Magrini, R. A. Norte, R. Riedinger, I. Marinković, D. Grass, U. Delić, S. Gröblacher, S. Hong, and M. Aspelmeyer, "Near-field coupling of a levitated nanoparticle to a photonic crystal cavity," *Optica*, vol. 5, no. 12, pp. 1597–1602, 2018.

[170] J. Loubser and J. van Wyk, "Electron spin resonance in the study of diamond," *Reports on Progress in Physics*, vol. 41, no. 8, p. 1201, 1978.

[171] E. van Oort, N. Manson, and M. Glasbeek, "Optically detected spin coherence of the diamond NV centre in its triplet ground state," *Journal of Physics C: Solid State Physics*, vol. 21, no. 23, p. 4385, 1988.

[172] P. Neumann, R. Kolesov, B. Naydenov, J. Beck, F. Rempp, M. Steiner, V. Jacques, G. Balasubramanian, M. Markham, D. Twitchen *et al.*, "Quantum register based on coupled electron spins in a room-temperature solid," *Nature Physics*, vol. 6, no. 4, pp. 249–253, 2010.

[173] R. Schirhagl, K. Chang, M. Loretz, and C. L. Degen, "Nitrogen-vacancy centers in diamond: nanoscale sensors for physics and biology," *Annual Review of Physical Chemistry*, vol. 65, pp. 83–105, 2014.

[174] P. Rabl, P. Cappellaro, M. G. Dutt, L. Jiang, J. Maze, and M. D. Lukin, "Strong magnetic coupling between an electronic spin qubit and a mechanical resonator," *Physical Review B*, vol. 79, no. 4, p. 041302, 2009.

[175] D. Lee, K. W. Lee, J. V. Cady, P. Ovartchaiyapong, and A. C. B. Jayich, "Topical review: spins and mechanics in diamond," *Journal of Optics*, vol. 19, no. 3, p. 033001, 2017.

[176] Z. Yin, N. Zhao, and T. Li, "Hybrid opto-mechanical systems with nitrogen-vacancy centers," *Science China Physics, Mechanics & Astronomy*, vol. 58, no. 5, p. 050303, 2015.

[177] A. Albrecht, A. Retzker, and M. B. Plenio, "Testing quantum gravity by nanodiamond interferometry with nitrogen-vacancy centers," *Physical Review A*, vol. 90, no. 3, p. 033834, 2014.

[178] N. Aslam, G. Waldherr, P. Neumann, F. Jelezko, and J. Wrachtrup, "Photo-induced ionization dynamics of the nitrogen vacancy defect in diamond investigated by single-shot charge state detection," *New Journal of Physics*, vol. 15, no. 1, p. 013064, 2013.

[179] B. Grotz, M. V. Hauf, M. Dankerl, B. Naydenov, S. Pezzagna, J. Meijer, F. Jelezko, J. Wrachtrup, M. Stutzmann, F. Reinhard *et al.*, "Charge state manipulation of qubits in diamond," *Nature Communications*, vol. 3, no. 1, p. 729, 2012.

[180] G. Davies and M. Hamer, "Optical studies of the 1.945 ev vibronic band in diamond," *Proceedings of the Royal Society of London. A. Mathematical and Physical Sciences*, vol. 348, no. 1653, pp. 285–298, 1976.

[181] S. Beresnev, V. Chernyak, and G. Fomyagin, "Motion of a spherical particle in a rarefied gas. part 2. drag and thermal polarization," *Journal of Fluid Mechanics*, vol. 219, pp. 405–421, 1990.

[182] W. Sutherland, "LII. the viscosity of gases and molecular force," *The London, Edinburgh, and Dublin Philosophical Magazine and Journal of Science*, vol. 36, no. 223, pp. 507–531, 1893.

[183] N. D. Lai, D. Zheng, F. Jelezko, F. Treussart, and J.-F. Roch, "Influence of a static magnetic field on the photoluminescence of an ensemble of nitrogen-vacancy color centers in a diamond single-crystal," *Applied Physics Letters*, vol. 95, no. 13, p. 133101, 2009.

[184] D. Toyli, D. Christle, A. Alkauskas, B. Buckley, C. Van de Walle, and D. Awschalom, "Measurement and control of single nitrogen-vacancy center spins above 600 k," *Physical Review X*, vol. 2, no. 3, p. 031001, 2012.

[185] M. W. Doherty, V. V. Struzhkin, D. A. Simpson, L. P. McGuinness, Y. Meng, A. Stacey, T. J. Karle, R. J. Hemley, N. B. Manson, L. C. Hollenberg *et al.*, "Electronic properties and metrology applications of the diamond NV- center under pressure," *Physical Review Letters*, vol. 112, no. 4, p. 047601, 2014.

[186] M. Geiselmann, R. Marty, F. J. G. De Abajo, and R. Quidant, "Fast optical modulation of the fluorescence from a single nitrogen–vacancy centre," *Nature Physics*, vol. 9, no. 12, pp. 785–789, 2013.

[187] N. D. Lai, O. Faklaris, D. Zheng, V. Jacques, H. Chang, J. Roch, and F. Treussart, "Quenching nitrogen–vacancy center photoluminescence with an infrared pulsed laser," *New Journal of Physics*, vol. 15, no. 3, p. 033030, 2013.

[188] G. Fuchs, V. Dobrovitski, D. Toyli, F. Heremans, C. Weis, T. Schenkel, and D. Awschalom, "Excited-state spin coherence of a single nitrogen–vacancy centre in diamond," *Nature Physics*, vol. 6, no. 9, p. 668, 2010.

[189] N. Xu, J. Chen, and S. Deng, "Effect of heat treatment on the properties of nano-diamond under oxygen and argon ambient," *Diamond and Related Materials*, vol. 11, no. 2, pp. 249–256, 2002.

[190] A. Wolcott, T. Schiros, M. E. Trusheim, E. H. Chen, D. Nordlund, R. E. Diaz, O. Gaathon, D. Englund, and J. S. Owen, "Surface structure of aerobically oxidized diamond nanocrystals," *The Journal of Physical Chemistry C*, vol. 118, no. 46, pp. 26 695–26 702, 2014.

[191] K.-M. Fu, C. Santori, P. Barclay, and R. Beausoleil, "Conversion of neutral nitrogen-vacancy centers to negatively charged nitrogen-vacancy centers through selective oxidation," *Applied Physics Letters*, vol. 96, no. 12, p. 121907, 2010.

[192] M. Hauf, B. Grotz, B. Naydenov, M. Dankerl, S. Pezzagna, J. Meijer, F. Jelezko, J. Wrachtrup, M. Stutzmann, F. Reinhard *et al.*, "Chemical control of the charge state of nitrogen-vacancy centers in diamond," *Physical Review B*, vol. 83, no. 8, p. 081304, 2011.

[193] T. Plakhotnik and D. Gruber, "Luminescence of nitrogen-vacancy centers in nanodiamonds at temperatures between 300 and 700 K: perspectives on nanothermometry," *Physical Chemistry Chemical Physics*, vol. 12, no. 33, pp. 9751–9756, 2010.

[194] C. Santori, P. E. Barclay, K.-M. C. Fu, and R. G. Beausoleil, "Vertical distribution of nitrogen-vacancy centers in diamond formed by ion implantation and annealing," *Physical Review B*, vol. 79, no. 12, p. 125313, 2009.

[195] W. J. Fleming, "Physical principles governing nonideal behavior of the zirconia oxygen sensor," *Journal of the Electrochemical Society*, vol. 124, no. 1, pp. 21–28, 1977.

[196] A. Brailsford, M. Yussouff, and E. Logothetis, "A first-principles model of the zirconia oxygen sensor," *Sensors and Actuators B: Chemical*, vol. 44, no. 1-3, pp. 321–326, 1997.

[197] T. Seberson, J. Ahn, J. Bang, T. Li, and F. Robicheaux, "Optical levitation of a YIG nanoparticle and simulation of sympathetic cooling via coupling to a cold atomic gas," *arXiv preprint arXiv:1910.05371*, 2019.

[198] C. Zhong and F. Robicheaux, "Shot-noise-dominant regime for ellipsoidal nanoparticles in a linearly polarized beam," *Physical Review A*, vol. 95, no. 5, p. 053421, 2017.

[199] R. M. Pettit, L. P. Neukirch, Y. Zhang, and A. N. Vamivakas, "Coherent control of a single nitrogen-vacancy center spin in optically levitated nanodiamond," *JOSA B*, vol. 34, no. 6, pp. C31–C35, 2017.

[200] P. Andrich, B. J. Alemán, J. C. Lee, K. Ohno, C. F. de las Casas, F. J. Heremans, E. L. Hu, and D. D. Awschalom, "Engineered micro-and nanoscale diamonds as mobile probes for high-resolution sensing in fluid," *Nano Letters*, vol. 14, no. 9, pp. 4959–4964, 2014.

[201] H. S. Knowles, D. M. Kara, and M. Atatüre, "Observing bulk diamond spin coherence in high-purity nanodiamonds," *Nature Materials*, vol. 13, no. 1, p. 21, 2014.

[202] T. Gaebel, C. Bradac, J. Chen, J. Say, L. Brown, P. Hemmer, and J. Rabeau, "Size-reduction of nanodiamonds via air oxidation," *Diamond and Related Materials*, vol. 21, pp. 28–32, 2012.

[203] G. Planes Conangla, A. W. Schell, R. A. Rica, and R. Quidant, "Motion control and optical interrogation of a levitating single NV in vacuum," *Nano Letters*, 2018.

[204] T. Delord, P. Huillery, L. Schwab, L. Nicolas, L. Lecordier, and G. Hétet, "Ramsey interferences and spin echoes from electron spins inside a levitating macroscopic particle," *Physical Review Letters*, vol. 121, no. 5, p. 053602, 2018.

[205] T. Delord, P. Huillery, L. Nicolas, and G. Hétet, "Spin-cooling of the motion of a trapped diamond," *Nature*, vol. 580, no. 7801, pp. 56–59, 2020.

[206] T. Delord, L. Nicolas, Y. Chassagneux, and G. Hétet, "Strong coupling between a single nitrogen-vacancy spin and the rotational mode of diamonds levitating in an ion trap," *Physical Review A*, vol. 96, no. 6, p. 063810, 2017.